High-resolution and Large Field Microscopy of Expanded Mouse Brain Sections and Human Brain Organoids

Dissertation
zur
Erlangung des Doktorgrades (Dr. rer. nat.)
der
Mathematisch-Naturwissenschaftlichen Fakultät
der
Rheinischen Friedrich-Wilhelms-Universität Bonn

vorgelegt von

Juan Eduardo Rodríguez Gatica

aus
Talcahuano, Chile

Bonn 2023

Angefertigt mit Genehmigung der Mathematisch-Naturwissenschaftlichen Fakultät
der Rheinischen Friedrich-Wilhelms-Universität Bonn

1. Gutachter: Prof. Dr. Ulrich Kubitscheck
2. Gutachter: Prof. Dr. Rudolf Merkel

Tag der Promotion: 22.02.2024

Erscheinungsjahr: 2024

Abstract

Connectome analysis, the comprehensive mapping of neural connections within an organism nervous system has long been a formidable challenge in neuroscience. Traditional methods often fall short in providing a holistic view of neural circuits, especially when attempting to balance high-resolution imaging with the need to cover large tissue volumes. This study addresses this challenge by introducing a transformative imaging technique, Light Sheet Fluorescence Expansion Microscopy (LSFEM).

LSFEM synergizes two powerful imaging modalities: light sheet fluorescence microscopy (LSFM) and expansion microscopy (ExM). Conventionally, while confocal microscopy excels in capturing high-resolution images of tissue sections and small model organisms, it struggles with larger samples. On the other hand, tomographic techniques, suitable for centimeter-sized samples often compromise on resolution. LSFEM effectively bridges this divide enabling cellular resolution imaging of millimeter-sized samples, thus providing a solution that is both expansive in coverage and meticulous in detail.

Drawing inspiration from the design blueprint proposed by Baumgart & Kubitscheck, a custom-built light sheet microscope was developed. This microscope, characterized by its upright design, underwent iterative refinements with a focus on enhancing both axial and lateral resolution. A standout feature of the final design is its objective revolver that allows for swift magnification changes during a single acquisition session. This adaptability combined with the microscope's ability to accommodate diverse sample sizes aligns seamlessly with the "Smart imaging" concept, which optimizes imaging performance by selectively targeting specific portions of a vast volume.

The application of LSFEM was demonstrated in the mapping of neural circuits within the mouse hippocampus and cortex. This approach provided unprecedented insights into the organizational principles of these circuits, capturing intricate subcellular structures like dendritic spines and synaptic junctions. Historically, such detailed imaging necessitated the use of high-resolution microscopy techniques, such as electron microscopy or super-resolution optical microscopy. However, these methods often come with their own set of challenges, including intensive sample preparation, potential introduction of artifacts or limitations in sample volume coverage.

LSFEM's transformative approach offers a solution that is both efficient and versatile. By physically expanding the sample, the effective resolution is enhanced, allowing for the capture of intricate subcellular structures. This technique supports large analysis volumes, a stark contrast to the limited range of methods like STED. Furthermore, LSFEM is compatible with a plethora of staining and labeling techniques, enabling selective identification of specific cell types or structures.

Beyond its applications in neuroscience, the potential of LSFEM extends to fields like developmental biology and cancer research. The study also introduces a new iteration along with lattice light-sheet microscopy (LLSM) using innovative hardware for lattice light-sheet generation tailored for expanded samples, further enhancing the imaging capabilities.

With the burgeoning development of artificial intelligence (AI) tools in image analysis, the synergy of AI methods with LSFEM presents a potent combination to tackle the connectome problem.

In conclusion, LSFEM offers a groundbreaking approach to super-resolution imaging, promising efficient and detailed imaging studies in the future. By leveraging this technique, researchers can achieve a comprehensive understanding of tissue architecture and organization, propelling advancements in connectomics research and beyond.

Publications

Parts of this thesis have previously been published in peer-reviewed journals:

Articles

2022 **J. E. Rodriguez-Gatica**†, V. Iefremova†, L. Sokhranyaeva, C. Au Yeung, Y. Breitkreuz, O. Brüstle, M. K. Schwarz, and U. Kubitscheck*, "Imaging Three-Dimensional Brain Organoid Architecture from Meso- to Nanoscale across Development", Development (2022).
DOI: https://doi.org/10.1117/1.NPh.6.1.015005

2020 A. Stockhausen†, J. Bürgers†, **J.E. Rodriguez-Gatica**, J. Schweihoff, R. Merkel, J.M. Prigge, M.K. Schwarz, and U. Kubitscheck*, "Hard-wired lattice light-sheet microscopy for imaging of expanded samples", Opt. Express (2020).
DOI: https://doi.org/10.1364/OE.393728

2019 J. Bürgers†, I. Pavlova†, **J.E. Rodriguez-Gatica**†, C. Henneberger, M. Oeller, J. Ruland, J.P. Siebrasse, U. Kubitscheck*, and M.K. Schwarz*, "Light Sheet Fluorescence Expansion Microscopy: Fast Mapping of Neuronal Connectivity at Super Resolution", Neurophotonics (2019).
DOI: https://doi.org/10.1242/dev.200439

† These authors contributed equally.

* Corresponding authors.

Further publications

2023 A. Stockhausen, **J. E. Rodriguez-Gatica**, J. Schweihoff, M. K. Schwarz, and U. Kubitscheck, "Airy beam light sheet microscopy boosted by deep learning deconvolution", Opt. Express (2023). DOI: https://doi.org/10.1364/OE.485699 .

2023 **J. E. Rodriguez-Gatica**, V. Iefremova, O. Brüstle, M. K. Schwarz, and U. Kubitscheck, "Stufenlose In-toto-Analyse expandierter humaner Hirnorganoide vom Millimeter- bis zum Nanometerbereich", Biospektrum (2023) [not peer-reviewed]. DOI: https://doi.org/10.1007/s12268-023-2055-z

2023 J. Arcos, F. Grunenwald, D. Sepulveda, C. Jerez, V. Urbina, T. Huerta, P. Troncoso-Escudero, D. Tirado, A. Perez, R. Diaz-Espinoza E. Nova, U. Kubitscheck, **J. E. Rodriguez-Gatica**, C. Hetz, J. Toledo, P. Ahumada, D. Rojas-Rivera, E. Martín-Montañez, M. Garcia-Fernandez, and R.L. Vidal, "IGF2 prevents dopaminergic neuronal loss and decreases intracellular alpha-synuclein accumulation in Parkinson's disease models", Cell Death Discovery (2023)**.** DOI: https://doi.org/10.1038/s41420-023-01734-1

2023 K. Barmpa, C. Saraiva, G. Gomez-Giro, E. Gabassi, S. Spitz, **J. E. Rodriguez-Gatica**, P. Antony, G. Robertson, F. Papastefanaki., U. Kubitscheck, A. Salti, P. Ertl, R. Matsas, F. Edenhofer, and J.C. Schwamborn, "Age-induced midbrain-striatum assembloids model early phenotypes of Parkinson's disease", BioRxiv. DOI: https://doi.org/10.1101/2023.10.28.564305

2023 **J. E. Rodriguez-Gatica**, M. K. Schwarz, U. Kubitscheck, "Light sheet fluorescence microscopy of expanded neuronal tissue", ***submitted to Neuromethods (book chapter)*** [not peer reviewed].

2021 A. Möller-Kerutt, **J. E. Rodriguez-Gatica**, K. Wacker, R. Bhatia, J. Siebrasse, N. Boon, V. Van Marck, P. Boor, U. Kubitscheck, J. Wijnholds, H. Pavenstädt and T. Weide, "Crumbs2 Is an Essential Slit Diaphragm Protein of the Renal Filtration Barrier", JASN (2021). DOI:https://doi.org/10.1681/ASN.2020040501

Invited Talks

2023 **J.E. Rodriguez-Gatica**, “Light sheet fluorescence expansion microscopy: From single synapses to long distance neuronal connections”, in First National Congress of the Italian Core facilities Network, Milano, Italy.

2023 **J.E. Rodriguez-Gatica**, “Light sheet fluorescence expansion microscopy: From single synapses to long distance neuronal connections”, in Light-Sheet Microscopy and Spatial Proteomics with Miltenyi Biotec, CECAD – University of Cologne, Cologne, Germany.

2023 **J.E. Rodriguez-Gatica**, “Light sheet fluorescence expansion microscopy: From single synapses to long distance neuronal connections”, in Expansion and Light-Sheet Microscopy Workshop, Universidad Mayor, Santiago, Chile.

2022 **J.E. Rodriguez-Gatica**, “The transparent brain - Light sheet microscopy of expanded neuronal tissue and brain organoids”, in Webinar for LiSIUM (Light-Sheet Imaging at Universidad Mayor), Universidad Mayor, Santiago, Chile.

2022 **J.E. Rodriguez-Gatica**, “Imaging long-range neuronal connections in the mouse brain by light sheet fluorescence expansion microscopy”, in Webinar for LabRoots and Miltenyi Biotec, Germany.

2021 **J.E. Rodriguez-Gatica**, “Light sheet fluorescence expansion microscopy: From Meso to Nanoscale”, in Microscopy for the Study of Bacterial Biofilms, Binational course: Biomedical Neuroscience Institute (BNI), University of Chile, Santiago, Chile; Instituto de Investigaciones Biológicas Clemente Estable (IIBCE), Montevideo, Uruguay.

Conference platform presentations

2023 **J. E. Rodriguez-Gatica**, M. K. Schwarz and U. Kubitscheck, “Imaging long-range neuronal connections in the mouse brain by light sheet fluorescence expansion microscopy”, in European Light Microscopy Iniciative 2023, Noordwijk, the Netherlands.

2023 **J. E. Rodriguez-Gatica**, N. Brady, M. K. Schwarz, and U. Kubitscheck, “Super-resolution imaging achieved by specimen expansion and light sheet microscopy”, in Trends in Microscopy 2023, Münsingen, Germany.

2022 **J. E. Rodriguez-Gatica**, V. Iefremova, L. Sokhranyaeva, C. Au Yeung, Y. Breitkreuz, O. Brüstle, M. K. Schwarz, and U. Kubitscheck, “Imaging Three-Dimensional Brain Organoid Architecture from Meso- to Nanoscale across Development”, in Neuroscience 2022, Society for Neuroscience, San Diego, USA.

2022 **J. E. Rodriguez-Gatica**, V. Iefremova, L. Sokhranyaeva, C. Au Yeung, Y. Breitkreuz, O. Brüstle, M. K. Schwarz, and U. Kubitscheck, “Imaging Three-Dimensional Brain Organoid Architecture from Meso- to Nanoscale across Development”, in From Stem Cells to Human Development 2022, Surrey, UK.

2019 **J.E. Rodriguez-Gatica**, I. Pavlova, J. Schweihoff, J.P. Siebrasse, M.K. Schwarz, and U. Kubitscheck, “Light sheet fluorescence expansion microscopy and serial block face sectioning: Complete mapping of extended neuronal circuits at super resolution”, in Neuroscience 2019, Society for Neuroscience, Chicago, USA.

Poster presentations

2022 **J. E. Rodriguez-Gatica**, V. Iefremova, L. Sokhranyaeva, C. Au Yeung, Y. Breitkreuz, O. Brüstle, M. K. Schwarz, and U. Kubitscheck, “Imaging Three-Dimensional Brain Organoid Architecture from Meso- to Nanoscale across Development”, in Enabling imaging across scales, European Molecular Biology Laboratory Imaging Centre Symposium, Heidelberg, Germany.

2018 **J.E. Rodriguez-Gatica**, I. Pavlova, J. Bürgers, U. Kubitscheck, and M.K. Schwarz, “Expansion Light Sheet Microscopy: Fast Imaging of Neuronal Connectivity Maps at Super Resolution”, in Neuroscience 2018, Society of Neuroscience, San Diego, USA.

2018 **J.E. Rodriguez**, I. Pavlova, J. Bürgers, U. Kubitscheck, and M.K. Schwarz, “Expansion Light Sheet Microscopy: Fast Imaging of Neuronal Conectivyty Maps at Super Resolution”, in 10th Light-Sheet Conference 2018, Dresden, Germany.

2017 **J.E. Rodriguez**, J. Bürgers, M. Franke, S. Memarhosseini, M. Oeller, J.P. Siebrasse, M.K. Schwarz, and U. Kubitscheck, “Light Sheet Fluorescence Microscopy Of Expanded Samples”, in Focus on Microscopy 2017, Bordeaux, France.

Table of Contents

Abbreviations

2D	Two-dimensional
3D	Three-dimensional
4D	Four-dimensional
4-hydroxy-TEMPO	4-Hydroxy-2,2,6,6-tetramethylpiperidine 1-oxyl
AcX	Acryloyl-X
AI	Artificial intelligence
APS	Ammonium persulfate
CLEM	Correlative light and electron microscopy
CLSM	Confocal laser scanning microscopy
DG	Dentate gyrus
EM	Electron microscopy
ExM	Expansion microscopy
FM	Fluorescence microscopy
FOV	Field-of-view
FWHM	Full width at half maximum
GA	Glutaraldehyde
GC	Granule cells
GCL	Granule cell layer
HDB	Horizontal limb of the diagonal band of Broca
LLSFM	Lattice light-sheet microscopy
LSFEM	Light sheet fluorescence expansion microscopy
LSFM	Light sheet fluorescence microscopy
MA-NHS	Methacrylic acid N-hydroxysuccinimide ester
NA	Numerical aperture
OB	Olfactory bulb
ON	Overnight
OPFOS	Orthogonal-plane fluorescence optical sectioning
oRG	Outer radial glia
oSVZ	Outer subventricular zone

PALM	Photo-activated localization microscopy
PFA	Paraformaldehyde
PSF	Point spread function
ROI	Region of interest
RT	Room temperature
SBF-SEM	Serial block-face scanning electron microscopy
sCMOS	Scientific CMOS
SIM	Structured illumination microscopy
SMI	Spatially modulated illumination
SMLM	Single-molecule localization microscopy
SNR	Signal-to-noise ratio
SPIM	Selective plane illumination microscopy
SRM	Super-resolution microscopes
STED	Stimulated emission depletion microscopy
STORM	Stochastic optical reconstruction microscopy
SYN1	Synapsin1
TEMED	Tetramethylenediamine
VZ	Ventricular zone
WD	Working distance
WI	Water immersion
ZO1	Zonula occludens protein 1

1 Introduction

For all organ systems, except one, it is well established how the structure of an organ is related to its function. The exception is the brain, where our understanding of structure and function remains inadequate. Neuroscience is focused on the study of the neuronal circuits of the brain in which the main goal is developing the understanding of human functionality, where an important requirement for advancing our knowledge is to recognize its elements as well as their interactions. The generation of a complete topographic map of the brain, called connectome, has become a major goal (Jorgenson et al., 2015; Lichtman and Sanes, 2008).

In particular, understanding brain functionality is challenging because the activity of large populations of neurons across many brain areas is interdependent, which creates an exceedingly complex dynamical system. In some cases, where there is homogeneity among elements of a large system, physicists have been able to describe such joint dynamics in simplified terms, like models of gas molecules or magnetic interactions. Such simplifications are not possible in the neuronal system because of the great heterogeneity of its components (Keller and Ahrens, 2015). Therefore, to understand the whole system, it may be necessary to observe neural activity across large brain regions. Ideally then, one would aspire to obtain full spatiotemporal access to the whole brain at the sub-cellular level and millisecond resolution (Ahrens and Engert, 2015).

1.1 Challenges in optical microscopy

A major problem in connectome analysis is that the critical details of neuronal connectivity, the synapses occur on length scales of about 100-200 nm and are thus beyond the resolving power of traditional microscopy methods and can only be resolved using “super-resolution” light microscopy or electron microscopy.

Electron microscopy (EM) is considered the gold standard for high-resolution imaging due to its high-resolution power of ~1nm, and is typically used to resolve neuronal constituents, which are often as thin as 100-200 nm in diameter and thus beyond the diffraction limit of classical light microscopy as we will explain later. So-called “volumetric EM” has also the advantage of providing unbiased rendering of cellular and subcellular structures of the nervous system within neuronal ensembles. However, visualizing neuronal connectivity between extended neuronal structures by electron microscopy almost invariably requires cutting the preparation into a series of thin slices. Such slices must then be individually imaged and aligned in a tedious and error-prone procedure before any three-dimensional structure can be successfully reconstructed (Abbott et al., 2020; Titze and Genoud, 2016).

To date, modern light microscopy allows us to address phenomena at sub-cellular, cellular, and supra-cellular levels, generating data for testing novel hypotheses and new findings. In particular, fluorescence microscopy (FM) has emerged as a powerful technology in neuroscience since it allows the identification of specific features of biological specimens, e.g., groups of differentially stained neurons by immunochemistry. Thus, FM offers the ability to produce high-resolution multicolor images that are easier to analyse compared to EM images, enabling the delineation of spatially extended relationships of distinct neuronal structures.

The overall performance of FM is determined by three main factors: The first is the use of characteristic wavelengths of light to illuminate the sample (the excitation wavelength), from which a response wavelength is detected (the emission wavelength). Secondly, the imaging technique and the optics used, and finally the imaged sample itself. The first point presents the fundamental difference to EM, since in FM the resolution is limited by the diffraction barrier of the light (Abbe limit), with an achievable lateral resolution (d_{xy}) of ~250 nm for optical microscopy.

$$d_{xy} = \frac{0.61 \cdot \lambda_{em}}{NA}, \qquad NA = n \cdot sin\alpha$$

Where, λ_{em} is the emitted wavelength of the sample and NA is the numerical aperture with n being the refractive index and α is half the opening angle of the objective.

Many researchers have made numerous attempts to overcome the resolution limit by improving the power and quality of the microscopes. Successful novel techniques have been invented that circumvent the diffraction barrier and achieve a resolution down to a few nanometers. These include spatially modulated illumination (SMI) (Gustafsson, 2000; Neil et al., 1997), stimulated emission depletion microscopy (STED) (Hell and Wichmann, 1994), stochastic optical reconstruction microscopy (STORM) (Rust et al., 2006), or photo-activated localization microscopy (PALM) (Betzig et al., 2006).

The main idea of SMI is to combine multiple interfering (coherent) illumination fields to create artefacts in the image that are perfectly known. The generated spatial modulation is then used to recalculate an enhanced point spread function (PSF), thus obtaining additional information.

STORM and PALM rely on the stochastic activation of individual fluorophores with photoactivatable properties, which can be switched off and on with certain light frequencies in combination with and stochastic methods to compute the real structure. These two methods necessarily require post-processing and mathematical models to reconstruct the actual structure. Conversely, STED applies a fluorescence excitation and a simultaneous ring-shaped depletion illumination to reduce the detection point and therefore the point spread function, making it possible to generate super-resolution images without requiring any post-processing.

The third point influencing the overall performance of FM concerns the sample itself. In biology, the properties of the sample can severely limit the applicability of a certain technique, and these super-resolution methods are not exempt from this. When the sample to be observed presents inhomogeneities; mainly due to lipids and proteins in biological samples of animal origin, it creates changes in their refractive index causing the light to scatter which ultimately deteriorates the subsequent image. Thus, this deterioration causes a distortion of the expected resolution. These blurring effects increase upon deeper penetration into the sample (penetration depth). In general, to image large samples, both, resolution and penetration depth are not independent of each other and must be finely balanced.

It is important to note that super-resolution techniques that rely on sharpening the PSF are not feasible for the reconstruction of extended neuronal networks. All available optical super-resolution approaches are restricted to thin samples of maximally 20 µm in depth. In addition, such technologies typically require expensive equipment and/or have slow imaging speeds. Electron microscopy for instance requires special instrumentation and also the serial alignment of thousands of sections (Briggman and Bock, 2012; Titze and Genoud, 2016). Note that the largest dimensions of high-throughput EM datasets that are currently being produced are in the range of about (300 µm)^3 (Briggman and Bock, 2012; Peddie et al., 2022). Moreover, an additional bottleneck for obtaining neuro-connectomic data concerns the segmentation of the images (Collinson et al., 2023). In summary, all these factors limit the applicability of these techniques to questions of neuronal connectivity. The reason being that synaptically-connected neurons can be spatially separated from each other by dozens or even hundreds of micrometres.

What are the prerequisites to obtain a resolution resolving neuronal connections without degrading the resolution due to penetration depth? What if we physically enlarge the sample, instead of improving the resolution of our microscope. A recently introduced method expands the sample tissue to effectively increase the optical resolution by a factor of four (Chen et al., 2015). This works by synthesizing a swellable polymer network within a specimen that can be physically expanded. As a result of this expansion, macromolecules that are as close as 60 nm before the expansion can be resolved almost without distortion of the relative protein position. This increases the effective resolution and enables imaging of critical neuronal details using conventional light microscopes. Moreover, a beneficial side effect of expansion is that the gel absorbs the surrounding medium, thus acquiring its refractive index. The strong water absorption during the expansion process further enhances the sample's transparency allowing optimal imaging, thereby bypassing the depth-limit of super-resolution techniques.

1.2 Expansion microscopy

Boyden and co-workers were the first to introduce expansion microscopy (ExM), a radically new technique that allows effective super-resolution using light microscopy by increasing the size of the tissue sample rather than increasing the optical resolution equipment-wise (Chen et al., 2015). Using this approach optical resolution limitations are bypassed by modification of the tissue (Chen et al., 2015; Ku et al., 2016).

The first report of ExM (Chen et al., 2015) utilized an anchoring strategy for fluorescent tags through DNA-conjugated antibodies. This approach enabled the labelling of relevant structures through indirect immunostaining with a fluorescent DNA conjugate that can be incorporated into the hydrogel during free-radical gelation. This work was extended by Chozinski and Tillberg (Chozinski et al., 2016; Tillberg et al., 2016), allowing ExM with conventional labelling methods, allowing for an easier and less expensive protocol.

The fundamental principle behind ExM is the embedding of water-adsorbent polymers to physically expand enzymatically treated tissue samples. Although polymer embedding is not new in biology to improve optical properties (Chung et al., 2013; Germroth et al., 1995), ExM took advantage of an additional osmotic mechanism of polyelectrolyte gels that drives swelling by orders of magnitude in volume (Tanaka et al., 1980).

The idea is to use molecular handles to covalently anchor biomolecules and/or labels of a fixed biological sample to the polymer network. Afterwards, the sample itself is digested but the anchored labels remain unaltered. Since the labels are linked to the gel matrix, fluorescence microscopy can then reveal the topological structure of the tissue sample.

As with other super-resolution methods, ExM can only be applied to chemically fixed biological samples. During the fixation process, primary amino groups react with formaldehyde. The primary amino groups are present at the N-terminus of proteins, but also on various amino acids such as lysine. Amino groups have a free electron pair on the nitrogen, which can add nucleophilically to the carbonyl carbon of the formaldehyde. The resulting tetrahedral intermediate reacts via water splitting to form an imine. An amino group of a second protein can nucleophilically attack the imine carbon, so that ultimately two proteins are linked via a methylene bridge (Kiernan, 2000). In essence, paraformaldehyde (PFA) crosslinks amino groups without changing the tertiary structure of proteins so that most epitopes remain available for specific antibodies (Fujiwara and Pollard, 1980; Robinson and Snyder, 2004).

In ExM, before synthesizing the expandable polymer within the fixed tissue sample, proteins of interest need to be labelled. This can be achieved either by conventional antibody staining, where the primary antibody is targeted against the protein of interest and a secondary antibody containing a fluorophore is binding to the primary antibody or by direct visualization of overexpressed fluorescent proteins. Subsequently, the addition of linker molecule such as methacrylic acid N-hydroxysuccinimide ester (MA-NHS) then allow the formation of bridges between the fluorescent antibody complexes or the fluorescent proteins with the polymer matrix.

After these preparation steps the sample is embedded into the polymer gel containing sodium acrylate, a monomer that ensures superabsorbent properties of the resulting gel, and acrylamide, a co-monomer also providing good water-absorbing properties. Finally, N,N'-methylene bisacrylamide acts as a crosslinker and binds the polymers consisting of the monomers and co-monomers together. Note that changes in the crosslinker ratio allow to engineer the expansion factor of the polymer. Importantly, the expansion ratio is inversely proportional to the sodium acrylate / acrylamide proportions. Due to the small size of the monomers and crosslinkers (~100 Da), the resulting polymer network easily permeates the intracellular space.

During the gelation of the sample, a gel matrix is formed by free-radical polymerization, where ammonium persulfate (APS) serves as an initiator and tetramethylenediamine (TEMED) accelerates polymerization (Chen et al., 2015). Additionally, the use of an inhibitor like tetramethylpiperidin-1-oxyl (4-hydroxy-TEMPO) allows complete diffusion of the monomers throughout the tissue.

After the gel is formed by the free-radical polymerization, the sample is “mechanically homogenized” by enzymatically digesting proteins and removing lipids. Due to the structure of the sample, the gel cannot attain its homogeneous elastic properties, preventing uniform expansion. It is therefore essential that the tissue digestion process is complete. Only after the digestion or homogenization of the sample, isotropic tissue expansion can be achieved. Therefore, samples are incubated within a digestion buffer based on guanidine, that facilitates homogenization. Tris and EDTA act as a buffer to prevent DNA and protein degradation. Triton-X is needed to lyse cells to extract proteins or organelles and to permeabilize the cell membranes. Finally, a proteinase (e.g. proteinase-K) can enzymatically cleave the peptide bonds that link the amino acid groups within proteins.

The process of lipid removal in ExM is indirect. While most fixations employ aldehydes to create chemical cross-links with reactive lysine groups, the majority of lipids or their membrane probes do not react strongly with aldehydes. As a result, they remain mobile post-chemical fixation (Wen et al. 2020). Additionally, during the digestion process, components such as EDTA can help to break down lipid-protein interactions, indirectly facilitating lipid removal. Triton-X; which can solubilise lipid bilayers, also plays a role in effective lipid removal. Consequently, upon permeabilization, digestion, and expansion, most lipids will be solubilized and washed out of the expandable polymer (Wen et al., 2020).

After the sample has been completely digested, it consists only of the gel matrix to which fluorophores are bound. In this condition the sample can then be expanded.

In the last ExM step, the gel is expanded by immersion into distilled water. After changing the water several times, expansion passes into saturation reaching in total a 4-fold maximum expansion (Figure 1.1C). As a result, the fluorescent labels are linked to the grid of the gel with negligible distortion and inhomogeneity after expansion. The resulting sample can be optically imaged on conventional fluorescence microscopes, resulting in “effective super-resolution” images.

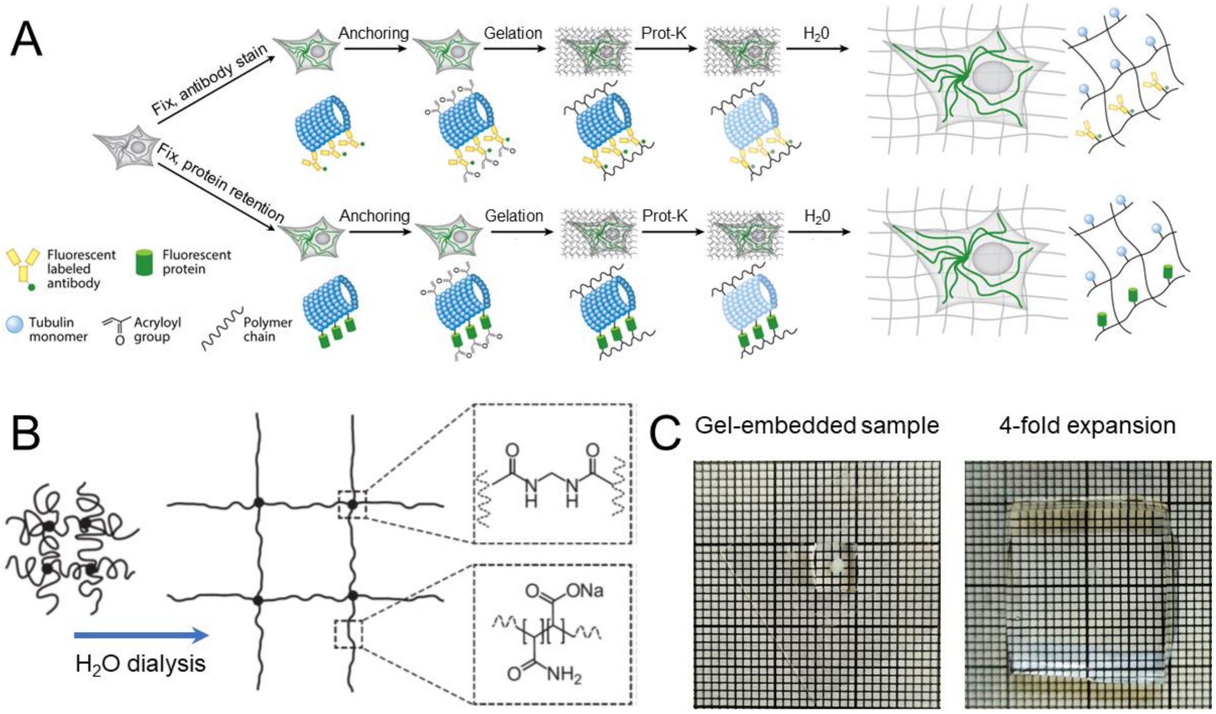

Figure 1.1. General overview of Expansion Microscopy. (A) (Top workflow) Samples are chemically fixed and stained with antibodies, using conventional immunostaining protocols, before anchoring treatment and subsequent ExM processing (gelation, Pro-K treatment, and expansion in water). (Middle workflow) Samples expressing FPs are chemically fixed and anchored before subsequent ExM processing. (B) Polyelectrolyte gel network expands after water dialysis. The dots represent the crosslinker and the lines the polymer chain, which extends during the dialysis. (C) A two months old brain organoid embedded in a polyacrylamide gel and the same organoid after expansion in bidistilled water, which yielded an approximately 4-fold expansion, as seen in the comparison on graph paper. (A) and (B) modified from (Tillberg and Chen, 2019), (C) from (Rodriguez-Gatica et al., 2022).

1.3 Light sheet microscopy

Advances in light microscopy have provided new insights to key questions of modern biomedical sciences, while fostering more and more systematic approaches to understand the essence of life (Abbott, 2003); generating data for testing hypotheses and new findings with applications that encompass developmental biology, membrane biophysics, disease progression/treatment and wound healing studies.

Typically, both light illumination and detection occur through a single objective in microscopy. Simple designs with dichromatic mirrors and filters, which are matched to pass or block desired wavelengths, enable powerful microscopy methods. Within the scientific realm, various microscope types have been innovated. For instance, Confocal Laser Scanning Microscopy (CLSM) (Minsky, 1988) which introduced spatial pinholes to separate out-of-focus light, Total Internal Reflection Fluorescence Microscopy (TIRFM) (Axelrod, 1981; Fish, 2009) which uses an evanescent light field for illumination, or Two-Photon Excitation Microscopy (2p-M) which employs non-linear optics for light illumination (Denk et al., 1990).

A new approach called Light Sheet Fluorescence Microscopy (LSFM) has been developed based on the principle of decoupling illumination and detection by sending a thin ‘‘sheet’’ of laser light into the sample from the side using a dedicated objective. This concept originated from the work of Siedentopf and Zsigmondy, who employed the principle of light sheet microscopy, called slit ultramicroscope at that time, for counting gold particles in solution in 1902 (Siedentopf and Zsigmondy, 1902). In 1912, Zsigmondy improved his optical setup used for the observation of fine nanoparticles suspended in a liquid solution. As a result, he introduced the immersion ultramicroscope (Mappes et al., 2012), an invention for which he was awarded the Nobel prize for chemistry in 1925. Light sheet fluorescence microscopy found its first application in biology after the development of genetically encoded fluorescent proteins in the 1990s (Tsien, 2009). In 1993, a technique called orthogonal-plane fluorescence optical sectioning (OPFOS) used light sheet illumination to image the internal architecture of fixed cochlea by Voie, Burns and Spelman (Voie et al., 1993). Finally, it was not until 2004 that the application of light sheet microscopy was demonstrated for fast four-dimensional (4D) (x, y, z, t) live imaging of millimeter-sized embryos by Huisken and Stelzer (Huisken et al., 2004). With the aid of Selective Plane Illumination Microscopy (SPIM) they observed entire in-vivo fish embryos over a long period of time and reconstructed the results via 3D-volume rendering with a spatial resolution of 6 µm. This was an enormous step in life science. Since then several biological development processes could be observed and analysed (Cella Zanacchi et al., 2011; Keller, 2013; Khairy and Keller, 2011; Mertz and Kim, 2010; Wan et al., 2019). The popularity of this technique reached the extent that LSFM was recognized by Nature Methods as the "Method of the Year" 2014 (Method of the Year 2014, 2015).

However, while this technique offers valuable advantages, it has certain limitations. In the context of LSFM, the challenge of sample opacity or non-transparency emerges as a noteworthy hurdle in the imaging process. The presence of opaque samples leads to the scattering and absorption of a portion of the incident illumination. This initial consequence results in diminished light penetration into the deeper layers, constraining the attainable imaging volume.

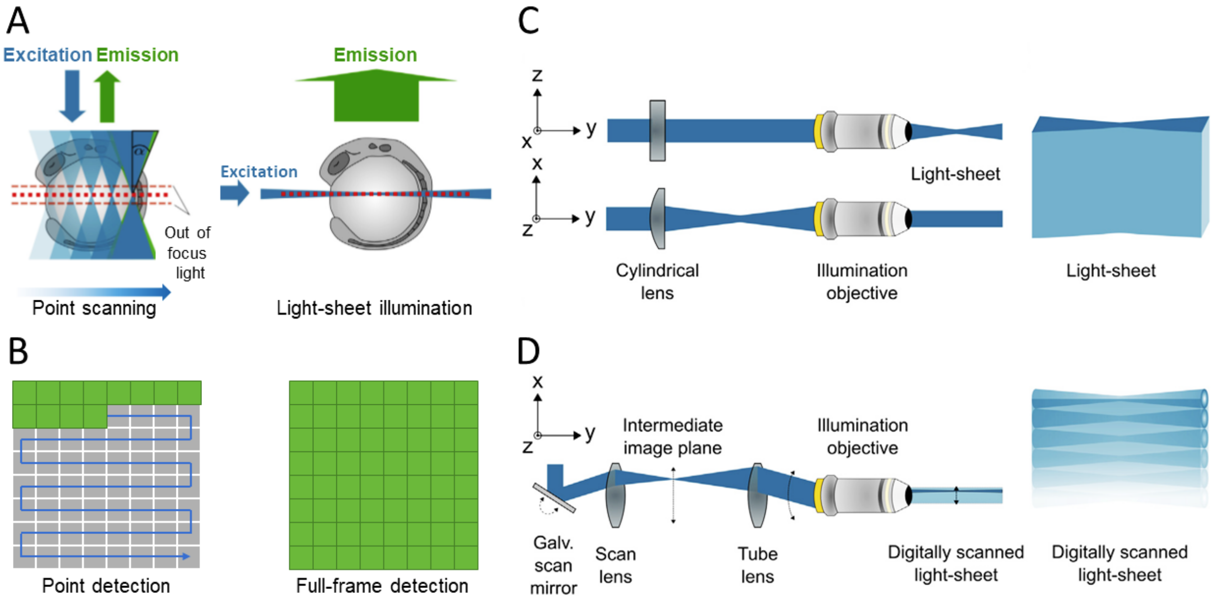

Figure 1.2. General overview of point scanning versus light sheet microscopy. (A) In point-scanning microscopy (confocal), sample illumination and detection occur through a laser beam that also illuminates areas above and below the intended focal plane. The sample is scanned point by point to generate an image of a single plane. (B) Conversely, light sheet microscopy illuminates an entire plane from the side, capturing the entire focal plane at once using an area detector instead of point-wise detection. (C) For generating a static light sheet, the Gaussian beam remains collimated in the yz-plane, while a cylindrical lens focuses it in the xy-plane before entering the illumination objective. This results in an extended beam in the xy-plane, focused along the z-axis. (D) In generating a digitally scanned light sheet, a combination of a galvanometric scan mirror and a scan lens creates a focused beam in the intermediate image plane. The galvanometric mirror's rotation induces a translation along the x-axis in the intermediate image plane, consequently moving the beam along the x-axis of the final image plane, resulting in a digitally scanned light sheet. (A),(C-D) modified from (Kromm et al., 2016).

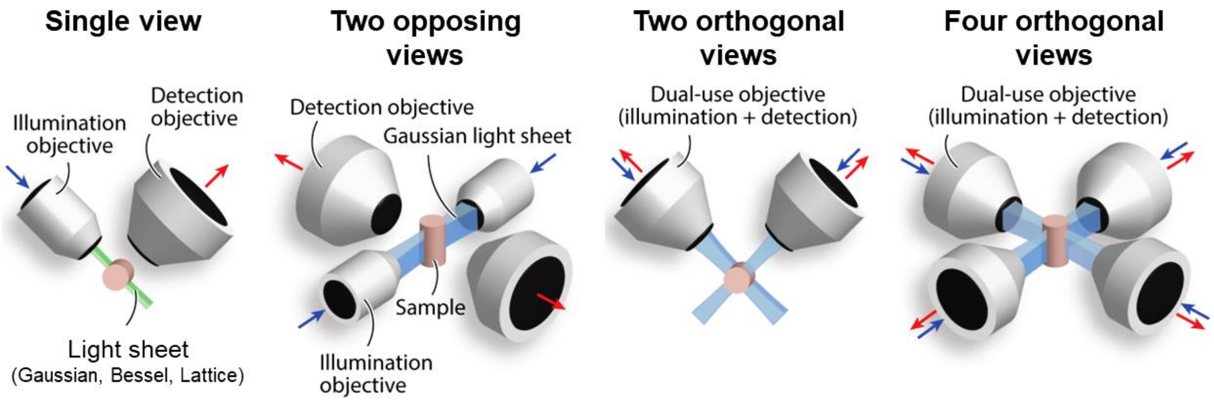

Figure 1.3. State-of-the-art light sheet microscopy techniques used for developmental imaging. Blue and red arrows indicate that an objective is used for laser illumination and fluorescence detection, respectively. All approaches of light sheet microscopes typically use Gaussian light sheets for fluorescence excitation (shown in blue), whereas Bessel and lattice light-sheet microscopes typically employ a dithered optical lattice (shown in green). Modified from (Wan et al., 2019).

Furthermore, the absorption and scattering of light within non-transparent samples give rise to uneven illumination across the specimen. This can engender artefacts, such as shadows and contribute to image blurring, consequently diminishing spatial resolution. While methods like the camera's rolling shutter can help mitigate out-of-focus light by reducing its impact to some degree, LSFM lacks the incorporation of a pinhole mechanism like in confocal microscopy, which effectively eliminates out-of-focus light and further enhances image clarity.

1.3.1 Working principle

Light Sheet Fluorescence Microscopy (LSFM) has two main distinguishing points compared to other fluorescence microscopy methods. The first point is the so-called optical slice, the other is the orthogonal layout of illumination and detection arm.

An optical slice can be generated by focusing in one plane a sheet of laser light. The light sheet is an elliptically focussed Gaussian beam (Saleh and Teich, 2013) which can be generated by focusing laser light with a cylindrical lens or by using a spherical focused beam which is fast scanned in one plane (Figure 1.2C-D). The latter method offers more flexibility as the height of the light sheet can be easily adapted by changing the scanning amplitude and its thickness by changing the diameter of the incoming laser beam (Kubitscheck, 2017). The advantages of this technique are the uniform illumination intensity over the complete field-of-view and the easy light sheet height adjustment through computer-controlled scanning mirrors.

Taking these into consideration, the illumination and detection light paths are completely separated from each other. Additionally, the focus is aligned to coincide with the focal plane of the detection optics. Thus, only signals in the overlapping region are detected and no out-of-focus fluorescence contributes to the image, which results in an optical sectioning effect (Figure 1.2A).

As the specimen is illuminated with a sheet of laser light, the entire focal plane of the detection arm is illuminated providing instant optical sectioning as opposed to the slow point scanning used in confocal microscopy (Figure 1.2B), making it the best choice for imaging large volumes. Reducing time is important to maintain ambient conditions and stability of the sample. By translating the sample along the detection axis through a static light sheet, a widely used approach has been established to acquire a z-stack as the camera continuously records images.

This increase of both acquisition speed and observation field in comparison to alternative non-invasive microscopy techniques becomes the primary tool when it comes to observing, tracking or quantifying dynamical phenomena in developmental biology and live imaging in general (Ahrens et al., 2013; Keller, 2013; Schmid et al., 2013).

A major challenge for fluorescence microscopy is the bleaching of the labelled samples. After each illumination, the sample loses a certain amount of its fluorescence property, i.e. the information of each image decreases with time. LSFM provides low bleaching by illuminating only the slice that is detected. It also yields a low photo-toxicity, given its fast and sensitive illumination/detection mechanism that allows observing very fast events in living organisms in the range of ~250 nm to millimeter-scale.

1.3.2 Illumination and detection arm

Usually, laser microscopes use one objective for illumination and detection. In LSFM the illumination and detection arm are orthogonal to each other, see Figure 1.3A due to the plane illumination. Positive side effects are a tremendous reduction of scattered illumination light due to the spatial separation of the arms. If the depth of focus of the detection objective matches the light sheet width, the axial resolution is enhanced because only the illuminated slice is detected.

By decoupling the illumination and detection arm, it is possible to tweak the illumination and the detection arms independently to adapt to the experimental needs (see review of (Wan et al., 2019)). Therefore, there are several technical implementations of light sheet microscopy developed for a wide range of applications (Figure 1.3).

The development of LSFM has enabled, for the first time, the imaging of an uncut whole brain in animal models such as Fly/Fish/Mouse, opening new windows for neuro connectomics. Given that imaging axonal connections throughout the structurally intact brain requires high resolution and sensitivity, LSFM becomes the obvious tool in which both are provided (Schwarz et al., 2015). Nevertheless, in order to achieve this, it has become necessary to have effective sample clearing protocols to minimize optical distortions. To this end, novel techniques that just started to emerge such as SCALE (Hama et al., 2011), CLARITY (Chung et al., 2013; Yang et al., 2014), CUBIC (Susaki et al., 2014) and FluoClearBABB (Schwarz et al., 2015) have been developed (for a review on different clearing procedures, see (Ueda et al., 2020)). The same principles are implemented in ExM, where due to the complete homogenization of the biological sample and the heavy adsorption of water, elements that can cause light distortion, such as lipids and proteins, are removed thereby making it almost perfectly transparent.

Thus, classical fluorescence microscopes are less well suited for ExM, as is LSFM. LSFM in contrast to confocal laser scanning microscopy, can handle both high volume data acquisition and low bleaching. While the combination of both techniques, ExM and LSFM seems natural, the correct optimization of both is not trivial, especially if the ultimate goal is to resolve intact neural circuits over large tissue extensions and still be able to obtain super-resolution images.

A solution to this issue came into reach with the development of light sheet fluorescence expansion microscopy (LSFEM), which has enabled the analysis of extended neural circuits in super-resolution (Bürgers et al., 2019; Gao et al., 2019; Schwarz and Kubitscheck, 2022).

1.4 Light sheet fluorescence expansion microscopy

As mentioned earlier, when designing a light sheet microscope, it is essential to determine the application for which it will be used. This is essential in order to choose the appropriate configuration of its illumination and detection arms, as well as the means to produce the light sheet, the achievable field-of-view (FOV) and the optical sectioning thickness. FOV and thickness need to be well-balanced for optimal imaging conditions because they are inversely proportional to each other. Conversely, sample preparation and mounting methods need to allow flexibility in order to perform a neuro connectomic analysis. By flexibility, we mean that the technique must be applicable to samples of different nature, while maintaining the ability to analyse neural circuits from the mesoscopic to the nanoscopic scale. The following section presents a description of the design and optimization process of these two techniques that we call light sheet fluorescence expansion microscopy (LSFEM).

1.4.1 Sample preparation

We started our microscopic approach focusing on the hippocampal dentate gyrus (DG). The DG is particularly interesting since it receives multiple sensory inputs, including olfactory, visual, auditory and somatosensory inputs via the lateral entorhinal cortex. Making it one of the very few brain areas that receives such a convergence of poly-sensory inputs, which makes it perfect for studying their neural networks and making comparisons between them. Figure 1.4 shows the process of the expansion over a sample of DG in a mouse brain sample.

In the first step of establishing ExM, the samples were stained with conventional antibodies: the primary antibody was targeted against the protein of interest, and the secondary antibody was carrying the fluorophore.

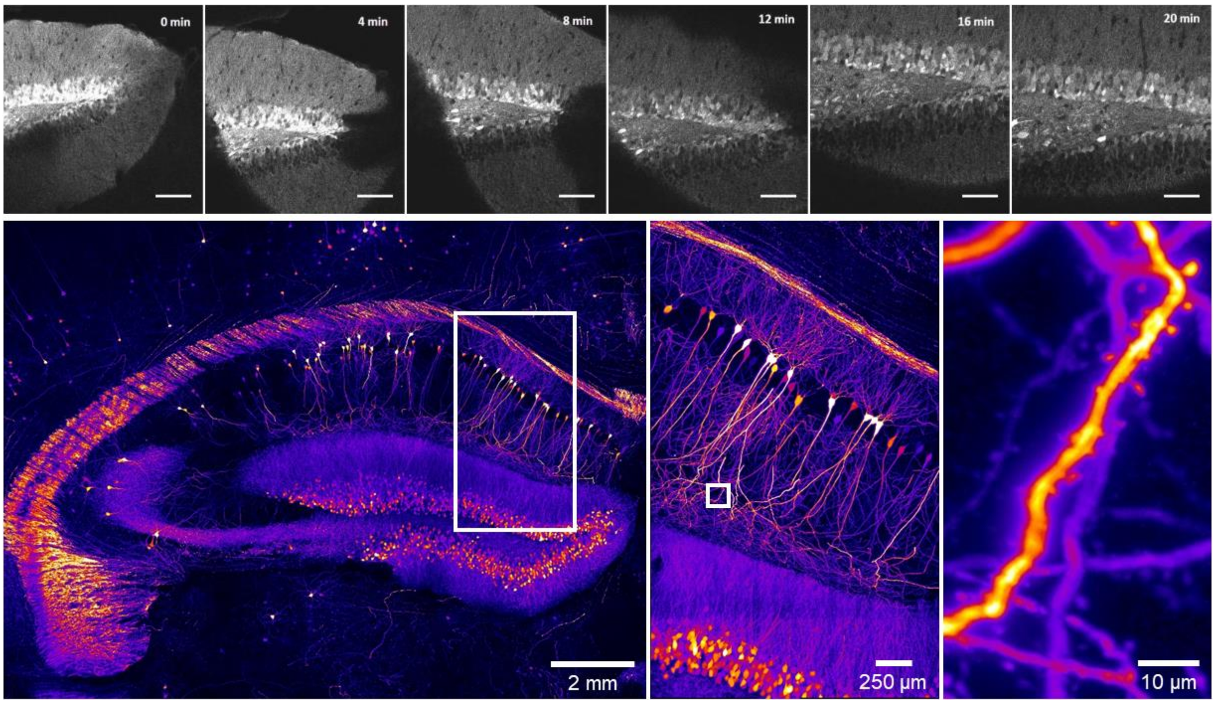

Figure 1.4. Process of expansion in a biological sample. (Top) Images of dentate gyrus (left to right) before expansion, 4, 8, 12, 16 and 20 minutes after. Scale bar 200 µm. Modified from (Oeller, 2016). (Bottom) Maximum intensity projection of an expanded mouse brain slice expressing EGFP. The endogenous EGFP fluorescence was enhanced by antibody staining against EGFP, the secondary antibody was conjugated to Alexa 488. The high virtual optical resolution after 4-fold expansion allowed identifying finest detail, e.g. the morphology of individual synaptic spines. (Rodriguez-Gatica et al. unpublished).

The initial ExM technique (Chen et al., 2015) encountered challenges related to biomolecule labelling, making it less accessible for many labs. Specifically, the original protocol did not have a comprehensive method to directly anchor biomolecules to the hydrogel matrix, a crucial step to maintain proteins in their native positions during expansion. Instead, the technique was demonstrated in cultured cells and brain tissue by staining the specimen with polymer-linkable probes, which required custom synthesis for preparation. These probes consisted of antibodies labelled with DNA oligonucleotides modified with both a fluorophore and a methacryloyl group, designed for covalent incorporation into the polymer. To anchor biomolecules to the gel, fixed samples are treated with acryloyl-X (AcX), methacrylic acid N-hydroxy succinimidyl ester (MA-NHS) or glutaraldehyde (GA). These compounds react with protein amines, anchoring them with functional groups that can participate in free-radical polymerization reactions during gelation, allowing native proteins and antibodies to be incorporated within the swellable hydrogel. In our quest for optimization, we opted against AcX due to its larger molecular size, which necessitates extended incubation periods. Additionally, GA was excluded because it produced excessive fluorescence background.

Initial studies, while successful in retaining fluorescent proteins, suffered from diminished and short-lived signals. This poses a challenge, especially for neuronal tissues, where prolonged imaging is essential to map entire connectomes. An improved protocol was thus developed, with an initial emphasis on conserving the inherent fluorescence of the samples. While the expansion process inevitably dilutes fluorescent labels, measures can be taken to counteract dye degradation from radical polymerization and proteolytic actions. The type and amount of linker play a pivotal role in the efficiency of molecule-to-gel bonding (Wen et al., 2020). Consequently, I increased the linker quantity to better preserve amine groups deep within the tissue. This is crucial as fluorescent dyes risk being lost during sample homogenization through digestion due to the random and sometimes inefficient anchoring process.

Expanding the sample by using Milli-Q water presents challenges due to its purity and low ion content. The water when exposed to air, absorbs carbon dioxide, leading to the formation of bicarbonate and a drop in pH. Over time, this pH decline can adversely affect the luminosity of fluorescent proteins, such as GFP (Haupts et al., 1998; Kneen et al., 1998). To address this, samples were rinsed in deionized water supplemented with 5mM Hepes buffer and with a pH adjusted to 7.4, achieving an expansion factor of approximately 4.0 times. This method reduces the expansion by roughly 11% but ensures the fluorescent proteins remain stable, especially during extended imaging sessions. This fluorescence-preserving enhancement, coupled with immunostaining, enabled us to discern various cell types in the hippocampal region (refer to Appendix A1).

Another significant hurdle to address was the constraint of working with samples with a maximum thickness of 100 µm. Considering that many neuronal connections in the brain extend over much greater distances, preserving the complete neuronal morphology becomes crucial.

The main challenge with thicker samples was to ensure effective penetration of the hydrogel matrix and subsequent uniform homogenization. To address the penetration issue, we modified the incubation times and introduced an initial gelation stage at 4°C. This low-temperature step slows down free radical reactions, ensuring thorough gel infiltration into the sample before polymerization commences.

For proper homogenization (Ebeling et al., 1974), we found that the starting enzyme concentration did not provide uniform tissue digestion, resulting in non-isotropic expansions. Depending on the tissue type and thickness, we recommend enzyme concentrations of 8, 16, or 32 units/ml. These adjustments allow for extended digestion phases, spanning multiple days, without compromising the brightness of even small clusters of fluorescent proteins. These methodological improvements have enabled us to prepare samples up to 500 µm thick, a significant leap from the original 100 µm limitation. Additionally, the gentle homogenization process preserves epitopes, facilitating post-process staining that reduces background and enhances signal quality (refer to Appendix A2).

This optimized technique is not limited to mouse brain samples; it can also be applied to more complex specimens like brain organoids (see Appendix A3). These organoids often exceed 500 µm in size and present unique challenges, such as the need for specialized antibodies to study intricate structures. To optimize the penetration of antibodies and linker in tissues larger than 500 µm, we added an extra permeabilization step using the detergent CHAPS. This step should be executed prior to the initial 'Anchoring' phase of the expansion procedure, as illustrated in Figure 1.1, and also before the staining process with antibodies. Unlike Triton X-100, CHAPS forms smaller micelles, enabling better sample penetration and more effective solubilisation of membrane proteins without denaturation.

Brain organoids, derived from human stem cells, offer a novel approach to model human brain development and diseases. They exhibit complex structures that mimic several facets of early neurogenesis, including polarized neuroepithelium, neurogenic ventricular and outer radial glia (oRG), and the formation of layered, cortex-like architectures. These features allow us to study various aspects of human brain development in a tissue-like context *in vitro* (Qian et al., 2019). Finally, these methodological advancements have allowed us to prepare samples up to 2 mm in thickness, representing a progression of 1900% from the initial constraint. This enables the preservation of a wide range of 3D extended structures that would otherwise be lost, complicating their subsequent analysis and reconstruction.

1.4.2 Hardware developments

1.4.2.1 Light sheet setup

Our initial analysis utilized a custom-built setup based on a Nikon Eclipse Ti-U inverted microscope, as shown in Figure 1.5A (Memarhosseini, 2016). This straightforward setup with a single illumination arm was chosen, anticipating near-complete sample transparency with minimal scattering.

In brief, the laser beam in the illumination arm is digitally navigated across the desired sample plane. This scanned point is relayed by optics into the back focal plane of the illumination objective, creating an effective light sheet at the sample. The fluorescence light is captured by the detection objective and directed to the Nikon microscope body, where a filter blocks any stray light and a tube lens projects the collected information onto the camera detector.

To adapt the setup to our needs, the sample chamber was the first to be modified due to its significant physical constraints during sample handling. The original chamber, custom-designed with a glass bottom for imaging and side glass walls for illumination, had limiting internal dimensions (4 mm x 20 mm x 2 mm), especially when considering a fourfold expansion factor. This width constraint effectively limited tissue expansion to just 1 mm, potentially curtailing the extent of the neural circuitry under study.

To better handle expanded samples, we designed a new custom sample chamber, depicted in Figure 1.5C. This chamber incorporated an illumination window from a standard coverslip and facilitated three-dimensional sample chamber movement. The expanded sample was anchored to a similar coverslip, which was horizontally inserted into the chamber forming its base.

While this design (Figure 1.5C) offered a 50-fold increase in volume, it had a drawback: the entire chamber, including its base, drifted during z-stack acquisition when the sample was moved to be scanned in depth. This introduced lens aberrations affecting the microscope's resolution. To address this, a new sample chamber was designed, as shown in Figure 1.5D.

Despite the resolution improvements with this chamber, we did not achieve the theoretical values (lateral: 242 nm and axial: 790 nm). The inverted acquisition path of the existing setup and optical aberrations from the bottom coverslip were the culprits. To counter this, we reconfigured the microscope with a vertical acquisition path, illustrated in Figure 1.5E-F. This setup allowed the objective to immerse in the same medium as the sample, enhancing resolution, while still accommodating a revolver for multi-scale imaging.

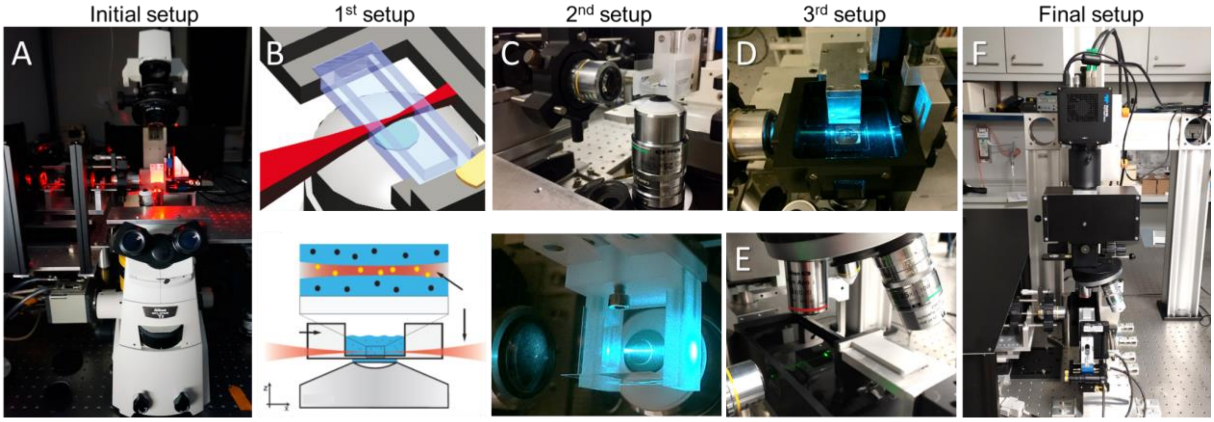

Figure 1.5. Light sheet setup. (A) Custom-built light sheet setup based on a Nikon Eclipse Ti-U inverted microscope. (B) (Top) Original chamber, custom-designed with a glass bottom for imaging and side glass walls for illumination. (Bottom) The excitation laser beam enters the chamber through the window from the left-hand side. (C) New custom sample chamber, closed by a third coverslip glued to the bottom side. (D) The expanded sample was fixed to a conventional coverslip (24 x 24 mm, 0.17 mm) by poly-L-lysine, and mounted so that the sample was inverted (sample hanging from the coverslip) on a motorized sample holder, in order to be moved in three spatial directions by motorized micro-translation stages. (E-F) Reconfiguration of the microscope with a vertical (upright) acquisition path. The sample size is now only limited by the travel range of the 3D stage, which corresponds to 24x24x24 mm^3. (B) modified from (Ritter et al., 2010).

Table 1.1: Experimental Optical Resolution.

		Theoretical resolution	**1st setup**	**2nd Setup**	**3rd setup**	**Final setup**
Lateral		242 nm	520 nm	380 nm	380 nm	380 nm
Axial		790 nm	2300 nm	1625 nm	1200 nm	1100 nm

* The theoretical FWHM values were determined using the procedures given above and emission wavelengths of 520 nm for green excitation.

** All values have errors of maximally 5%.

1.4.2.2 Optical resolution

Setup and sample chamber optimizations led to resolution improvements, quantified using fluorescent amine-modified beads in a similar hydrogel as used in ExM. Table 1 charts the resolution evolution from the initial to the latest configuration, showcasing significant improvements in both lateral and axial dimensions. These figures represent a 27% and 52% improvement in lateral and axial resolution, respectively, compared to the original setup. Assuming a fourfold average expansion factor, these values translate to virtual optical resolutions of 95 nm (lateral) and 275 nm (axial), enabling the resolution of synaptic neuronal connections.

1.4.2.3 Shifted Beam Waist

Our microscope's light sheet is virtual, generated by a scanning mirror that moves the laser beam. Due to the beam's divergence, the image is sharply focused at the beam waist position but blurred outside this focal region.

To enhance image quality, we limited image acquisition to a sub-image region centered around the beam waist (Dean et al., 2015). For a complete image, the beam waist shifted to five consecutive positions along the camera chip, and the final image was stitched together from these sub-images, as depicted in Figure 1.6C. This width can be adjusted to match any objective lens in the revolver, allowing the sub-image size to be tailored for optimal resolution when assembling the final image.

The light sheet's thickness and the field of view along the illumination axis are inter-dependent. Thus, both parameters must be judiciously selected based on the specimen under analysis. For instance, many applications in developmental biology and neuroscience require expansive FOV and long working distance objectives to allow image imaging of specimens ranging up to millimeters in size.

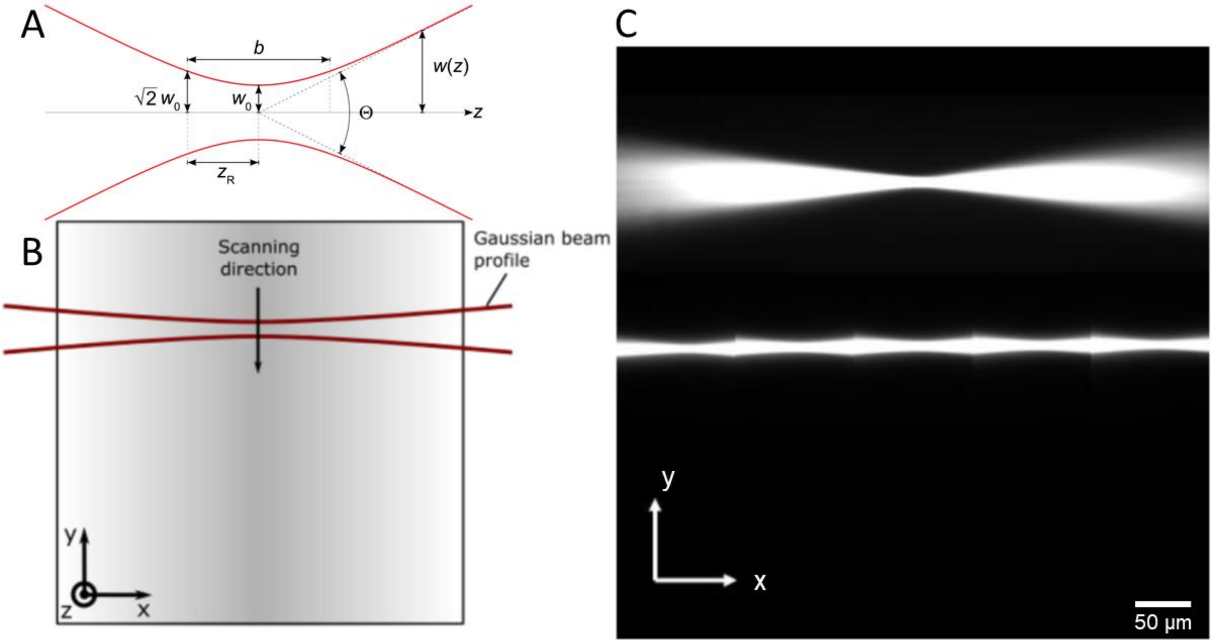

Figure 1.6. Gaussian beam profile. (A) Parameters of a Gaussian beam propagating in z are defined. The parameter w_0 indicates the beam waist, θ is the full angle of divergence. The Rayleigh length z_R is the distance from the beam waist to the point where the beam radius has expanded to $\sqrt{2}w_0$ due to divergence. (B) Direction of the digitally scanned light sheet. The darker the gray value within the image the higher is the intensity. (C) Gaussian intensity profile (top)and Gaussian beam tilling (bottom), To enhance image quality the beam waist could be shifted (e.g. 5 times). (A-B) modified from (Bürgers, 2016).

Thus, we find ourselves at an intersection of two powerful techniques. On one side, there is ExM, a method that physically expands a sample, enhancing the visualization of intricate structures at a higher resolution using conventional light microscopy. When fine-tuned for larger specimens, ExM holds the potential to preserve entire connectomes, embedded seamlessly within the hydrogel matrix. Yet, the expanded sample's potential remains untapped without an adept microscopy technique to scan this gel comprehensively.

Given this backdrop, light-sheet microscopy emerges as a natural counterpart. By illuminating the sample one thin slice at a time, it capitalizes on the transparency achieved when the sample absorbs the medium. This method not only scans the sample with speed and precision but also does so with minimal invasiveness. By reducing the light exposure, it ensures swift 3D scanning of expansive specimens while minimizing phototoxicity and photobleaching.

Thus, the synergy of tissue expansion and light-sheet microscopy, named as LSFEM in this thesis, forges a methodological platform. This platform empowers researchers with the capability to conduct high-speed, multicolor fluorescent microscopic imaging of vast nerve tissue samples at a level comparable to existing super-resolution microscopic techniques.

2 Results and Discussion

Conventionally, confocal microscopy has been the gold standard approach to image tissue sections and parts of small model organisms at high resolution. In contrast, at the larger scales, tomographic techniques have been established to reconstruct centimeter-sized samples, however, at lower resolution. Light-sheet microscopy represents a facile tool that bridges the gap between the above-mentioned technologies by providing cellular resolution on millimeter-sized samples.

A combination of LSFM with ExM promises to exceed this size spectrum considerably (Daetwyler and Fiolka, 2023). Thus, it is possible to resolve structures originally limited to super-resolution techniques (Igarashi et al., 2018; Werner et al., 2021), while maintaining the ability to cover millimeter-sized samples.

Migliori et al.'s publication was the first to suggest the innovative idea of merging these two methods (Migliori et al., 2018). However, their exploration of ExM was limited to a single example of a 250 µm thick coronal slice, captured with a low-magnification objective (10x/0.6NA). Their primary focus was on unveiling a new light sheet configuration, "light-sheet Theta", rather than exhaustively exploring the resolution advantages of this combination. Yet, early 2019 marked a significant milestone with concurrent publications from our team and another group (Bürgers et al., 2019; Düring et al., 2019). Both papers systematically showcased the ExM and LSFM combination, emphasizing the clearing capabilities of our expansion protocol. Our research demonstrated that this union enables imaging of extensive brain tissue volumes with subcellular detail.

In this work, we synergize tissue expansion and light sheet fluorescence microscopy to facilitate volumetric super-resolution imaging of expansive mouse brain and human organoid samples. We advocate for this pairing as the optimal solution for capturing super-resolved images of extended neuronal circuits, characterized by (i) high imaging rates up to 50 Hz, (ii) high contrast, and (iii) minimal photobleaching. This method, named "Light Sheet Fluorescence Expansion Microscopy" (LSFEM), is the cornerstone of our research.

2.1 Fast mapping of neural circuits at super-resolution

The results discussed in this chapter have been published in *Neurophotonics*. The publication is reproduced in Appendix A1.

Our first work (Bürgers et al., 2019) delves into the capabilities of Light Sheet Fluorescence Expansion Microscopy (LSFEM), with a focus on rapid volumetric super-resolution imaging of the mouse dentate gyrus. A standout feature of our approach is its ability to observe fluorescent proteins directly, eliminating the need for antibody staining, inherent in the original protocol (Chen et al., 2015). This innovation not only paves the way for using thicker samples, side-stepping the antibody penetration challenge but also enables comprehensive neural connection mapping within the context of large cell ensembles spanning several orders of magnitude. Importantly, this feature does not negate the use of antibodies. As demonstrated in the publication results, it facilitates the combination of fluorescent protein expression with antibody staining.

Our primary objective was to design a method that seamlessly integrates tissue expansion with light sheet fluorescence microscopy (LSFM). This integration empowers us with the capability for high-speed, large field-of-view volumetric imaging of neural circuits at a subcellular level. By employing LSFM on expanded mouse brain samples, specifically targeting the CA1 and dentate gyrus molecular, granule cell, and polymorphic layers, we achieved a lateral resolution of 100 nm and an axial resolution of 415 nm. This precision facilitated a detailed evaluation of granule cell and neurite morphology within extensive cell ensembles.

We also assessed the capabilities of confocal laser scanning microscopy for obtaining high-resolution volumetric images of extended neuronal networks. However, confocal microscopy proved to be slow and time-consuming, rendering it impractical for detailed reconstructions. For perspective, the total imaging duration required for a single confocal plane with a resolution of 2048×2048 pixels⁄image covering a field of 102.4×102.4 µm² required about 10.1 s, when no averaging was performed. Extrapolating this to a total volume of 1 mm³, total volume of the dentate gyrus, would amount to approximately 80 days (>1900 hours). Moreover, the resolution achieved by the confocal microscope was insufficient for unambiguously discerning the 3D structure of densely labelled granule cells, also imaging with confocal at deeper depths would be impossible due to sample bleaching owing to long acquisition times.

The LSFEM method we employed in this study capitalizes on tissue expansion, enhancing the samples' transparency and improving the effective resolution. Our custom-built microscope, tailored for ExM, produced images that vividly captured the intricate morphoanatomical contours of granule cells and dendrites. By using an objective lens with a high numerical aperture (NA) and long working distance, we acquired images in a mosaic-like fashion to cover an expansive field of view. The acquisition time for a complete stack of 400 images (covering a field of 355×355 µm²) was a mere 222.7 seconds, translating to a frame rate of 1.8 Hz. This high-speed imaging at low irradiances can generate large field-of-view images at subcellular resolution with minimal bleaching.

Remarkably, our imaging speed surpassed the current state-of-the-art high-resolution confocal laser scanning microscope by a factor of 17. We remain optimistic about further enhancement potential, aiming to optimize our setup and increase the imaging rate by a factor of 10 to 20, which would allow for nanoscale imaging of specimens in roughly 10 hours. The implications of this advancement are profound, as it could revolutionize the way researchers approach neural imaging, offering a more efficient and detailed view of complex neural networks.

We demonstrate our method's potential for studying neural circuit architecture and underscore its advantages over current imaging techniques. Combining structural and functional information with molecular phenotyping is crucial for understanding neural circuit connectivity and behaviour. Given the vast amount of data generated during imaging, our method offers new avenues for connectomics and graph analysis of large brain regions imaged in super resolution. We anticipate the need for novel mathematical algorithms and statistical tests to compare and analyse different neural circuits and identify anatomical connectivity patterns.

2.2 Hard-wired lattice light-sheet microscopy

The results discussed in this chapter have been published in *Optic Express*. The publication is reproduced in Appendix A2.

In order to improve acquisition time and resolution, in Appendix A2 (Stockhausen et al., 2020), we explore the capabilities of various light sheet microscopy methods, emphasizing their potential for elucidating developmental processes. By juxtaposing the resolution and performance of lattice light-sheet microscopy with Gaussian light sheet microscopy, we provide a detailed analysis of each method's strengths and weaknesses across different excitation wavelengths.

A primary challenge with the Gaussian beam, especially when used with thicker samples in conjunction with tissue expansion, was its limited field of view (FOV). This was largely due to pronounced beam divergence, which subsequently reduced acquisition speed. To address this, we introduced a propagation invariant beam, termed lattice light-sheet microscopy (LLSFM). Tailored for transparent expanded samples, LLSFM offers enhanced axial resolution and a significant reduction in imaging time.

The lattice light-sheet microscope setup, employing an array of Bessel-Gaussian beams, produces a low-diverging light sheet with consistent thickness ensuring uniform sample illumination. Unlike the LLSFM configuration by Chen et al. (Chen et al., 2014), which utilized a spatial light modulator (SLM), our setup does not require an SLM. This eliminates the need for electronic control and complex SLM programming, thereby reducing the overall implementation cost. Instead, we have innovated a straightforward lattice light-sheet microscope using a micro-fabricated fixed ring mask for lattice light-sheet generation. The integration of this high-precision hardware mask further accentuates the method's capability for simultaneous multicolor imaging, given the constant z-position of the lattice across different excitation wavelengths.

Our experimental approach centered on imaging mouse brain samples processed using a refined expansion protocol. Notably, antibody staining against EGFP was performed post-digestion, optimizing tissue permeability and minimizing non-specific binding effects. A preliminary check of successful sample preparation was conducted using a confocal laser scanning microscope.

To ensure stability during measurements in our upright setup, expanded gel samples were anchored to a coverslip using poly-L-lysine. The chamber was subsequently filled with deionized water, and the pH was meticulously adjusted to 7.4 to enhance fluorophore stability over time. This protocol facilitated sample expansion by approximately fourfold, enabling high-resolution imaging across vast tissue extensions. Imaging was executed using simultaneous excitation wavelengths of 405 and 488 nm. As the sample moved through the lattice light sheet, we captured volumetric data, unveiling expanded DG neurons and their neurites in exceptional detail.

Image acquisition was achieved with a single frame exposure time of 30 ms. In total, a stack of 2000 frames was acquired in 143 seconds, corresponding to a frame rate of 14 Hz. A transparent sample volume of 1 mm^3 was imaged in under 40 minutes, adhering to the Nyquist criterion—a significant improvement over our previous approach.

The lattice light sheet's homogeneous excitation resulted in a substantially larger usable field of view. With an axial resolution of 1.2 µm over a field of view of (333 µm)^2, the lattice light sheet covers twice the area compared to a Gaussian illumination field of view of (198 µm)^2 with equivalent axial resolution.

A maximum intensity projection of a stack showcased dendritic projections with unparalleled clarity across the complete FOV, revealing individual spines and slender spine necks in sharp resolution. The intensity profile of a spine neck exhibited a full width at half maximum (FWHM) of 640 nm. Considering the expansion factor of four, this equates to a mere 160 nm—impressively below the optical diffraction limit.

In conclusion, our study underscored the efficacy of our optimized expansion protocol and showcased the potential of LLSFM in imaging intricate details over expansive scales. We successfully imaged mouse brain samples that were twice the thickness of those processed by the original expansion protocol. Furthermore, we highlighted the potential of post-digestion immunolabelling, which amplified the signal of preserved fluorescent proteins, demonstrating LLSFM's potential for simultaneous multicolor imaging. This was evidenced by green-fluorescent granule cells labelled post-digestion with Alexa488-immunostaining against EGFP and cell nuclei staining using the UV-excitable dye DAPI.

2.3 Imaging expanded human brain organoids from the millimeter to the nanometer range

The results discussed in this chapter have been published in *Development*. The publication is reproduced in Appendix A3.

In our most recent work, Appendix A3 (Rodriguez-Gatica et al., 2022), we explore a cutting-edge setup that seamlessly combines organoid tissue expansion with light sheet fluorescence microscopy. This innovative approach is designed to image and quantify various spatial parameters during organoid development. By reconfiguring the microscope to an upright design and integrating an objective revolver within the LSFEM technique, we have pioneered a method that enables a smooth transition from a mesoscopic perspective to super-resolution, all within a single imaging session. This publication introduces a groundbreaking brain-organoid analysis pipeline, utilizing LSFEM to capture entire brain organoids across developmental stages in 3D.

Recent advancements in stem cell technology have catalyzed the evolution of three-dimensional (3D) cultures based on pluripotent stem cells, notably brain organoids. These self-assembling cellular structures emulate pivotal aspects of *in vivo* brain development, encompassing early neurogenesis, polarized neuroepithelium formation, and maturation to synapse formation. However, visualizing these multifaceted processes in their true three-dimensional form remains a significant challenge.

Brain organoids, given their density and size that can reach several millimeters, present inherent challenges for traditional imaging techniques. Their opacity often results in subpar contrast when subjected to conventional light microscopy. Moreover, their substantial size often precludes the use of high-resolution optical methods, which require objectives with a high NA and short working distances. However, by synergizing LSFM with a fully optimized protocol for organoid clearing and expansion, we have overcome these barriers, enabling in-depth analyses of organoids up to 15 mm in diameter and tracking their development over an impressive time span of up to 14 months.

Our initial experiments focused on optimizing organoid permeabilization. After fixation, the organoid tissue was treated with CHAPS, ensuring the preservation of autofluorescent proteins and enabling efficient staining of expansive whole-organoids using commercial antibodies. This setup, spanning four channels, visualizes selected cell types or stained cell structures, complemented by DNA staining to label all cell nuclei.

Through the application of optimized buffer solutions, we achieved tissue expansion ranging from 1.5-fold to 4-fold, preserving fluorophore stability and ensuring that the organoid's intrinsic structure remained intact. The clearing process significantly amplified contrast and overall image quality.

Microscopically relevant regions of interest in human brain organoids vary in size. LSFEM achieves effective super-resolution with a lateral resolution of less than 100 nm and an axial resolution of up to 300 nm. However, high-resolution images of large sample volumes present challenges. An organoid of 1 mm^3, after expansion, reaches a volume of 64 mm^3. Imaging this structure, considering the Nyquist theorem, generates a massive data set of 340 TB. Therefore, initial imaging should be at the mesoscopic level to locate regions of interest, which can subsequently be imaged at super-resolution if needed. This approach allows examination over length scales from centimeters to a few tens of nanometers, spanning over 5 orders of magnitude.

For imaging clarified and 1.5-fold expanded brain organoids at the mesoscale, we employed a low magnification/low NA objective. By expanding 4-fold and using a high magnification/high NA objective, we achieved super-resolution images over specific regions of interest. This allowed us to clearly visualize cell somata and neurites with extensions of several hundred micrometers. In the magnified sample regions, numerous spiny processes on the neurons indicated advanced differentiation and the formation of neuronal connections.

LSFEM's capabilities extend to the mesoscopic scale of organoid development, enabling examination and 3D visualization of rosette-forming neuroepithelial structures. This provides invaluable insights into their size and shape variations. At the microscale, LSFEM identifies outer radial glia (oRG) cells, with specific antibody staining enhancing their detection within the 3D image stack. While LSFEM's nanoscale imaging might not rival electron microscopy's resolution, its compatibility with multicolor fluorescence imaging is unparalleled. This feature enables synapse identification using both pre- and postsynaptic markers, allowing meticulous counting and spatial analysis of synapses in brain organoids without physical sectioning.

Our findings include the detection of oRG within extended organoids, clear demarcation of mitotic cleavage planes and dendritic spine formation. Notably, we are at the forefront of highlighting and introducing the 3D spatial co-localization of pre- and postsynaptic proteins in brain organoids.

3 Summary and Outlook

The primary aim of this study was to pioneer a technique that enables rapid, multicolor fluorescent imaging of extended nervous tissue samples at super-resolution, paving the way for the creation of a comprehensive connectome.

In pursuit of this goal, we established, evaluated, and applied a combination of light sheet fluorescence microscopy (LSFM) and expansion microscopy (ExM) to resolve neuronal circuits. The adaptability of expansion microscopy, which employs commercially available compounds and universally accessible optical systems, democratizes super-resolution imaging, making it accessible to a broader range of laboratories. By harnessing the optical sectioning capabilities and swift acquisition speed of LSFM, we overcame the challenges associated with imaging thick tissue sections, encompassing entire neuronal circuits, brain areas and even whole organs.

To facilitate the examination of expanded mouse brain sections, a light sheet microscope was developed in the initial phase of this work. This microscope drew inspiration from the design blueprint proposed by Baumgart & Kubitscheck (Baumgart and Kubitscheck, 2012). Its inaugural configuration boasted a custom-built light sheet fluorescence microscope, characterized by a digitally scanned light sheet and confocal slit detection. This setup aimed to validate the efficacy of confocal slit detection in augmenting contrast and signal-to-noise ratios in light sheet microscopes, without a particular focus on point spread function (PSF) optimization.

To further refine resolution, we integrated a novel sample chamber and undertook a thorough redesign of the microscope. We assessed the resolution of this LSFM using model bead samples embedded in polyacrylamide gel, identical to the gel used for expanded samples. The empirical results not only met but also exceeded our initial results. When compared with the preliminary setup, the axial PSF showcased a significant enhancement, registering at (1.1 ± 0.1) µm—a substantial 52% leap. The final lateral PSF, clocking in at (0.38 ± 0.02) µm, marked a notable 27% improvement. Deviations from the expected values (242 nm for lateral PSF and 790 nm for axial PSF) can be attributed primarily to two factors. Firstly, it is essential to acknowledge that slight compromises in resolution are to be expected due to the inherent presence of non-calculable aberrations encountered during experimentation. Secondly, in the case of lateral resolution, the maximum achievable resolution of 346 nm is determined by the effective pixel size of 173 nm, adhering to the Nyquist theorem.

Our overarching goal was to attain a resolution that could discern thin dendrites and spines over vast distances. We realized this through the successful imaging of expanded samples using LSFM and light sheet fluorescence expansion microscopy (LSFEM). However, perfecting this technique presented its own set of challenges, which we will delve into in the subsequent section.

3.1 Achievements

In Appendix A1, we showcased the synergy of Light sheet fluorescence expansion microscopy (LSFEM) techniques to achieve super-resolution images of biological samples. LSFM's strength lies in its ability to image large tissue volumes at high-resolution with minimal photodamage, making it particularly suited for studying neural circuits in the brain at subcellular resolution. By combining LSFM with ExM, we physically expanded the sample, thereby enhancing the effective resolution and capturing intricate subcellular structures like dendritic spines and synaptic junctions.

Historically, imaging and quantifying pre- to postsynaptic distances necessitated the use of high-resolution microscopy techniques, such as electron microscopy (EM) or super-resolution optical microscopy, which could detail synaptic structures. While EM offers unmatched resolution, it is not without its challenges. The intensive sample preparation it demands can be both time-consuming and error-prone with the potential introduction of artifacts that hinder data processing. Advanced imaging techniques like correlative light and electron microscopy (CLEM) (Boer et al., 2015) and serial block-face scanning electron microscopy (SBF-SEM) (Denk and Horstmann, 2004) provide 3D ultrastructural insights at nanometer-scale resolution (Friedrichsen et al., 2022; Schneider-Mizell et al., 2016; Serrano et al., 2022; Winding et al., 2023). Yet, CLEM demands significant expertise and resources, while SBF-SEM can inflict considerable photodamage.

Super-resolution optical microscopy techniques, including stimulated emission depletion (STED) microscopy (Hell and Wichmann, 1994), and structured illumination microscopy (SIM) (Gustafsson, 2005) deliver high resolution but are constrained by their limited sample volume (Lin et al., 2019; Sawada et al., 2018). This limitation becomes pronounced given the extensive travel of axons across brain regions (Economo et al., 2018; Kita and Kita, 2012; Oh et al., 2014). Techniques like Single-molecule localization microscopy (SMLM) (Betzig et al., 2006; Hess et al., 2006) offer high-resolution imaging of sub-synaptic structures, but they can be time-intensive. SMLM of single image frames can range from seconds to minutes due to the sequential activation and localization of individual fluorophores or molecules, requiring more time to continuously activate new fluorophores for imaging (Kashiwagi et al., 2019; Kashiwagi and Okabe, 2021; Lelek et al., 2021; Nägerl et al., 2008).

Our LSFEM technique has proven transformative, delivering comparable resolution but with expedited imaging times and reduced sample preparation costs. The fusion of LSFM and ExM magnified the microscope's effective resolution, facilitating super-resolution imaging. This method also supports larger analysis volumes, a stark contrast to the limited range of methods like STED. Notably, and in contrast to EM, LSFEM is versatile, compatible with a plethora of staining and labeling techniques, enabling for selective identification of specific cell types or structures.

We demonstrated the utility of LSFEM for mapping neural circuits in the mouse hippocampus and cortex providing new insights into the organizational principles of these circuits. We believe LSFEM's application extends beyond neuroscience, with the potential to provide breakthroughs in fields like developmental biology and cancer research.

In Appendix A2, building on our successes, we introduced a new iteration of lattice light-sheet microscopy (LLSM) specifically tailored for imaging expanded biological samples, which we termed "hard-wired" LLSM. This design was aimed at achieving super-resolution imaging of expanded samples, surpassing the capabilities of our previous LSFM approach. Moreover, it proved to be a faster and more efficient method of imaging these samples compared to earlier LLSM techniques (Chen et al., 2014). We showcased the efficacy of hard-wired LLSM in imaging neural tissue, enabling us to examine samples that were five times thicker than those analyzed using our prior approach. These samples, prepared with an optimized expansion method, were imaged with high spatial resolution and minimal distortion.

However, this technique is not without its own challenges. The use of a mask to generate the light pattern increases the energy losses in the laser as it passes through the mask. This makes it necessary to have a high-power laser before the mask, and to increase the exposure times on the sample, increasing the possibility of photobleaching and phototoxicity. Additionally, the diminished final illumination due to mask losses complicates the use of autofluorescent proteins, making it imperative to pre-stain samples with antibodies. This demands meticulous planning of the staining protocol, especially for thicker samples. The complexity of the required equipment, coupled with the need for specialized optical devices and efficient staining methods, can render this technique more intricate and costlier than conventional LSFM.

A study by Chang et al. (Chang et al., 2020) undertook a systematic and quantitative comparison of lattice and Gaussian light sheet microscopy, evaluating their resolution capabilities. Their findings indicated that lattice light-sheet microscopy marginally outperformed Gaussian light sheet microscopy in terms of resolution. Specifically, when measuring the full width at half maximum (FWHM) of a fluorescent bead under comparable imaging conditions, the lattice light-sheet microscopy achieved about 220 nm, while the Gaussian counterpart reached approximately 250 nm. Despite the promise of hard-wired LLSM as a cutting-edge technique for high-resolution imaging of expanded biological samples, its intricate nature and equipment demands might pose barriers to its broad adoption.

Given that a more intricate illumination does not significantly enhance resolution, we opted for Gaussian illumination in LSFM. Our final design was holistic, aiming to extract maximum information from the sample across multiple scales without dissecting it. This strategy, often termed "multiscale imaging" or "multiscale microscopy", tailors the imaging modality and resolution to the specific biological query and the sample's spatial scale.

Our optimization's final phase honed in on two pivotal aspects: refining the light sheet microscope's design to allow magnification shifts during a single acquisition session and fine-tuning the expansion technique to ensure consistent sample expansion at two distinct magnifications (1.5- and 4-fold).

Given the inherent challenges of working with brain organoids such as sample size variations and inter-organoid variability, the multi-scale imaging capabilities of our technique are invaluable. It allows for the capture of high-resolution images of specific regions while concurrently preserving a broader contextual view.

With this novel approach, we successfully obtained high-resolution images of outer radial glial cells (oRG), which represent only a minor fraction of the total neural progenitor cell population in the developing brain. This method capitalizes on its ability to scan entire samples, effectively addressing the spatial distribution challenges associated with these cells. Furthermore, it distinctly marks mitotic cleavage planes across expansive regions and captures dendritic spine formation, along with the 3D spatial co-localization of pre- and post-synaptic proteins in brain organoids, underscoring the need for super-resolution capabilities.

Appendix A3 pivoted to leveraging this novel imaging technique to delve into the development and organization of brain organoids across scales, from millimeters to the nanometers. While other studies have ventured into this domain (Mansour et al., 2018; Paşca et al., 2015; Yakoub and Sadek, 2019), they often resorted to dissecting the organoids, losing intrinsic sample information. Our research stands out as the pioneer in quantifying 3D synaptic distances in brain organoids, without the need for tissue dissection.

3.2 Conclusion and Outlook

At the microscopic level, confocal microscopy has successfully captured high-resolution images of tissue sections and small model organisms. Conversely, tomographic techniques have been developed for larger, centimeter-sized samples, albeit at reduced resolution. LSFM, as highlighted by Wan and Stelzer in their reviews (Stelzer et al., 2021; Wan et al., 2019), bridges this gap, enabling cellular resolution imaging of millimeter-sized samples.

LSFM, now enhanced by LSFEM, offers a groundbreaking approach to super-resolution imaging of expanded millimeter-sized samples. This technique not only achieves details previously reserved for super-resolution methods but also merges the benefits of small-scale imaging with large-scale tomographic imaging.

This fusion of scales aligns seamlessly with the “Smart imaging” concept. This concept is geared towards optimizing imaging performance by selectively targeting specific portions of a vast volume. It adeptly addresses temporal imaging constraints and achieves a harmonious balance between sample health, spatial resolution, field of view, and temporal resolution. In this context, upright microscopes, such as the one developed in this work, offer enhanced accessibility and versatility in light sheet microscopy. They can accommodate samples of diverse sizes and are instrumental in facilitating high-throughput imaging using multi-sample holders. Moreover, these pioneering designs herald new avenues in optical engineering and the integration of varied imaging modalities (Daetwyler and Fiolka, 2023).

As neuroscience increasingly employs "Smart imaging" to study intricate and dynamic cellular processes in the brain, LSFEM's capabilities become even more pertinent. Adaptive data acquisition schemes are evolving; they no longer strictly adhere to Nyquist sampling throughout the data set, but instead apply the finest sampling selectively. This algorithm-driven selection of regions of interest promises to eliminate human biases, enhancing the reproducibility of imaging studies.

Our work has significantly advanced our understanding of neural connectivity by enabling imaging of thick samples, preserving entire brain areas with their neuronal ensembles intact. Predominantly, this approach visualizes without disrupting desired neuron trajectories, thus avoiding information distortion or loss, a common issue with serial sectioning approaches.

By leveraging this technique, researchers can visualize detailed cellular and subcellular structures in larger samples, offering a holistic understanding of tissue architecture and organization. This is especially valuable for studying neural circuit connectivity, developmental processes and the spatial relationships between different cell types within tissues and organs. The ability to produce three-dimensional images provides the opportunity to include realistic spatial geometries into these models, improving their predictive power.

The technique has been extensively tested and evaluated using various sample types and biomarkers, demonstrating the feasibility and versatility of the chosen approaches. However, challenges remain, especially in data management and analysis due to the vast amounts of data generated. Light sheet microscopes employed in this technique can capture high-resolution images with exceptional spatial and temporal fidelity, leading to a substantial increase in data volume—approximately three orders of magnitude higher than conventional confocal microscopes (Kubitscheck, 2017). While the multi-scale approach is effective, the issues concerning data management and analysis of such vast amounts of data remain an ongoing challenge (Lichtman et al., 2014; Motta et al., 2019).

The burgeoning development of artificial intelligence (AI) tools in image analysis (Chamier et al., 2019; Durkee et al., 2021; Ravindran, 2022), provide a comprehensive review that explores the application of AI techniques, including deep learning and graph theory, in connectomics research. Similarly, Jain et al., 2010; Vu et al., 2018 discusses how machine learning holds great promise as an addition to the arsenal of analysis tools for discovering how the brain works at multiple stages and levels of neuroscience investigation. These tools can enhance the reliability and automation of tasks from image pre-processing to circuit reconstruction and analysis.

The synergy of AI methods with the technique developed in this thesis presents a potent combination to tackle the connectome problem, aligning with the emerging field of “Smart imaging”(Guo et al., 2022; Madhusoodanan, 2023).

Looking ahead, our innovative measurement method offers immense potential for investigating various biological processes. Its adaptability is a standout feature; it is not restricted to any specific sample type. By leveraging the sample holder's wide range of movement, combined with different magnification values and physical expansion techniques, neural circuits can be visualized within an impressive final volumetric space of 24x24x8 mm^3. Moreover, the intrinsic transparency of the expanded sample markedly enhances imaging depth. This not only propels advancements in connectomics research but also sheds light on the spatial distribution and morphology of biological structures.

Our advancements have paved the way for collaborations with valuable groups, e.g. the Developmental and Cellular Biology group led by Prof. Dr. Jens Schwamborn at the University of Luxembourg, focusing on midbrain-striatum assembloids to delve into Parkinson's disease (Barmpa et al. Manuscript in preparation). Additionally, our collaboration with Dr. Matthias Schneider's group from the Department of Neurosurgery at the University Hospital Bonn centers on studying glioblastoma spheroids embedded in human brain slices.

Although this work has primarily showcased the digestion of samples using proteinase K, the technique has also been successfully applied to other samples such as mouse kidneys (Chozinski et al., 2018; Möller-Kerutt et al., 2021), where an additional digestion step was implemented to remove collagen. This opens up possibilities for incorporating extra digestion steps tailored to specific sample requirements, such as breast cancer organoids embedded in a collagen matrix (Koorman et al., 2022; Mohan et al., 2021).

Furthering our collaborative endeavors, we have joined forces with Dr. Cristiana Lungu from the Institute of Cell Biology and Immunology at the University of Stuttgart. Together, we are exploring collagen-embedded spheroids to investigate breast-to-bone cancer metastasis.

Addressing the challenge of imaging thicker samples, we have amalgamated Light Sheet Fluorescence Expansion Microscopy with serial block face sectioning of expanded samples, utilizing a custom-developed microtome equipped with a 50 µm thin stainless-steel wire. While related physical sectioning techniques like KESM (Mayerich et al., 2008), fMOST (Li et al., 2010), SPT (Economo et al., 2016), and HLTP (Yang et al., 2018) have been proposed, their integration with LSFEM remains unprecedented and was first suggested by Schwarz and Kubitscheck (Schwarz and Kubitscheck, 2022). Our preliminary results, demonstrating an optimized protocol for the isometric expansion of 2 mm thick samples that also preserves the fluorescence of autofluorescent proteins, were presented at the Neuroscience Conference of the Society for Neuroscience in San Diego 2022.

Our ongoing research focuses on studying sensory perception, particularly in olfaction, where the horizontal limb of the diagonal band of Broca (HDB) influences olfactory bulb (OB) output. By using our optimized protocol on ~2 mm thick sagittal mouse brain slices, our aim is to elucidate synaptic connections between OB interneurons and HDB projection neurons. Preliminary results are shown in Figure 3.1A-E.

By deploying a device tailored for expanded samples, we can image an axially extended region of the sample at high speeds and then physically remove the imaged specimen slab, repeating the process until the entire sample is imaged. This iterative approach promises to image samples with virtually unlimited axial extensions, all while retaining super-resolution capabilities.

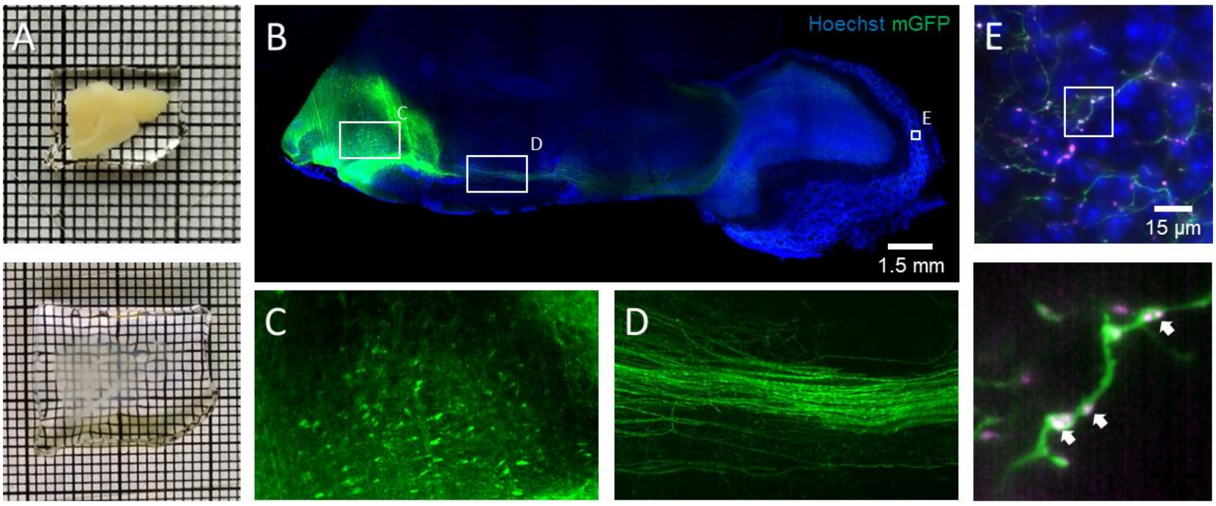

Figure 3.1. HDB-OB connectome project. (A) (Top) 2 mm thick sagittal cut of a mouse brain embedded in a polyacrylamide gel. (Bottom) The same sample after proteinase K digestion, which resulted in a clearing of the organoid and an approximately 1.5-fold expansion. (B) Maximum intensity projection comprising 200 images of the cleared and 1.5-fold expanded organoid showing mGFP positive cells. We infected the HBD region of wt cre-mice with a pAAV expressing mGFP in whole cells and mRuby in the pre-synaptic terminals by the expression of mRuby. (C) Site of the injection in the HDB area, (D) fiber path and (E) (top) Magnification of the ROI marked in B. projected fiber in the OB. (bottom) Zoom-in region highlighting the accumulation of pre-synaptic protein Synaptophysin expressed by mRuby, confirming the preservation of small clusters of fluorescent proteins. (Rodriguez-Gatica et al. in preparation)

References

Abbott, A. (2003). Cell culture: biology's new dimension. *Nature* **424**, 870–872. doi:10.1038/424870a.

Abbott, L. F., Bock, D. D., Callaway, E. M., Denk, W., Dulac, C., Fairhall, A. L., Fiete, I., Harris, K. M., Helmstaedter, M. and Jain, V. et al. (2020). The Mind of a Mouse. *Cell* **182**, 1372–1376. doi:10.1016/j.cell.2020.08.010.

Adhya, D., Chennell, G., Crowe, J. A., Valencia-Alarcón, E. P., Seyforth, J., Hosny, N. A., Yasvoina, M. V., Forster, R., Baron-Cohen, S. and Vernon, A. C. et al. (2021). Application of Airy beam light sheet microscopy to examine early neurodevelopmental structures in 3D hiPSC-derived human cortical spheroids. *Molecular autism* **12**, 4. doi:10.1186/s13229-021-00413-1.

Ahrens, M. B. and Engert, F. (2015). Large-scale imaging in small brains. *Current opinion in neurobiology* **32**, 78–86. doi:10.1016/j.conb.2015.01.007.

Ahrens, M. B., Orger, M. B., Robson, D. N., Li, J. M. and Keller, P. J. (2013). Whole-brain functional imaging at cellular resolution using light-sheet microscopy. *Nat Methods* **10**, 413–420. doi:10.1038/nmeth.2434.

Albanese, A., Swaney, J. M., Yun, D. H., Evans, N. B., Antonucci, J. M., Velasco, S., Sohn, C. H., Arlotta, P., Gehrke, L. and Chung, K. (2020). Multiscale 3D phenotyping of human cerebral organoids. *Sci Rep* **10**, 21487. doi:10.1038/s41598-020-78130-7.

Axelrod, D. (1981). Cell-substrate contacts illuminated by total internal reflection fluorescence. *The Journal of cell biology* **89**, 141–145. doi:10.1083/jcb.89.1.141.

Baumgart, E. and Kubitscheck, U. (2012). Scanned light sheet microscopy with confocal slit detection. *Optics express* **20**, 21805–21814. doi:10.1364/OE.20.021805.

Benito-Kwiecinski, S., Giandomenico, S. L., Sutcliffe, M., Riis, E. S., Freire-Pritchett, P., Kelava, I., Wunderlich, S., Martin, U., Wray, G. A. and McDole, K. et al. (2021). An early cell shape transition drives evolutionary expansion of the human forebrain. *Cell* **184**, 2084-2102.e19. doi:10.1016/j.cell.2021.02.050.

Bershteyn, M., Nowakowski, T. J., Pollen, A. A., Di Lullo, E., Nene, A., Wynshaw-Boris, A. and Kriegstein, A. R. (2017). Human iPSC-Derived Cerebral Organoids Model Cellular Features of Lissencephaly and Reveal Prolonged Mitosis of Outer Radial Glia. *Cell Stem Cell* **20**, 435-449.e4. doi:10.1016/j.stem.2016.12.007.

Betzig, E., Patterson, G. H., Sougrat, R., Lindwasser, O. W., Olenych, S., Bonifacino, J. S., Davidson, M. W., Lippincott-Schwartz, J. and Hess, H. F. (2006). Imaging intracellular fluorescent proteins at nanometer resolution. *Science* **313**, 1642–1645. doi:10.1126/science.1127344.

Bhaduri, A., Andrews, M. G., Mancia Leon, W., Jung, D., Shin, D., Allen, D., Jung, D., Schmunk, G., Haeussler, M. and Salma, J. et al. (2020). Cell stress in cortical organoids impairs molecular subtype specification. *Nature* **578**, 142–148. doi:10.1038/s41586-020-1962-0.

Boer, P. de, Hoogenboom, J. P. and Giepmans, B. N. G. (2015). Correlated light and electron microscopy: ultrastructure lights up! *Nature methods* **12**, 503–513. doi:10.1038/nmeth.3400.

Brémond Martin, C., Simon Chane, C., Clouchoux, C. and Histace, A. (2021). Recent Trends and Perspectives in Cerebral Organoids Imaging and Analysis. *Frontiers in Neuroscience* **15**. doi:10.3389/fnins.2021.629067.

Briggman, K. L. and Bock, D. D. (2012). Volume electron microscopy for neuronal circuit reconstruction. *Current opinion in neurobiology* **22**, 154–161. doi:10.1016/j.conb.2011.10.022.

Bürgers, J. (2016). Realization of Two-Color Excitation and Detection in a Multiphoton Scanned Light-Sheet Microscope. *Master thesis,* **Rheinische Friedrich-Wilhelms-Universität Bonn**, Bonn, Germany.

Bürgers, J., Pavlova, I., Rodriguez-Gatica, J. E., Henneberger, C., Oeller, M., Ruland, J. A., Siebrasse, J. P., Kubitscheck, U. and Schwarz, M. K. (2019). Light-sheet fluorescence expansion microscopy: fast mapping of neural circuits at super resolution. *Neurophotonics* **6**, 15005. doi:10.1117/1.NPh.6.1.015005.

Cajal, S. R. (1899). *Textura del sistema nervioso del hombre y de los vertebrados: estudios sobre el plan estructural y composición histológica de los centros nerviosos adicionados de consideraciones fisiológicas fundadas en los nuevos descubrimientos*: Moya.

Cella Zanacchi, F., Lavagnino, Z., Perrone Donnorso, M., Del Bue, A., Furia, L., Faretta, M. and Diaspro, A. (2011). Live-cell 3D super-resolution imaging in thick biological samples. *Nat Methods* **8**, 1047–1049. doi:10.1038/nmeth.1744.

Chamier, L. von, Laine, R. F. and Henriques, R. (2019). Artificial intelligence for microscopy: what you should know. *Biochemical Society transactions* **47**, 1029–1040. doi:10.1042/BST20180391.

Chang, B.-J., Dean, K. M. and Fiolka, R. (2020). Systematic and quantitative comparison of lattice and Gaussian light-sheets. *Optics express* **28**, 27052–27077. doi:10.1364/OE.400164.

Chang, J.-B., Chen, F., Yoon, Y.-G., Jung, E. E., Babcock, H., Kang, J. S., Asano, S., Suk, H.-J., Pak, N. and Tillberg, P. W. et al. (2017). Iterative expansion microscopy. *Nat Methods* **14**, 593–599. doi:10.1038/nmeth.4261.

Chen, B.-C., Legant, W. R., Wang, K., Shao, L., Milkie, D. E., Davidson, M. W., Janetopoulos, C., Wu, X. S., Hammer, J. A. and Liu, Z. et al. (2014). Lattice light-sheet microscopy: imaging molecules to embryos at high spatiotemporal resolution. *Science (New York, N.Y.)* **346**, 1257998. doi:10.1126/science.1257998.

Chen, F., Tillberg, P. W. and Boyden, E. S. (2015). Optical imaging. Expansion microscopy. *Science (New York, N.Y.)* **347**, 543–548. doi:10.1126/science.1260088.

Chozinski, T. J., Halpern, A. R., Okawa, H., Kim, H.-J., Tremel, G. J., Wong, R. O. L. and Vaughan, J. C. (2016). Expansion microscopy with conventional antibodies and fluorescent proteins. *Nat Methods* **13**, 485–488. doi:10.1038/nmeth.3833.

Chozinski, T. J., Mao, C., Halpern, A. R., Pippin, J. W., Shankland, S. J., Alpers, C. E., Najafian, B. and Vaughan, J. C. (2018). Volumetric, Nanoscale Optical Imaging of Mouse and Human Kidney via Expansion Microscopy. *Sci Rep* **8**, 10396. doi:10.1038/s41598-018-28694-2.

Chung, K., Wallace, J., Kim, S.-Y., Kalyanasundaram, S., Andalman, A. S., Davidson, T. J., Mirzabekov, J. J., Zalocusky, K. A., Mattis, J. and Denisin, A. K. et al. (2013). Structural and molecular interrogation of intact biological systems. *Nature* **497**, 332–337. doi:10.1038/nature12107.

Collinson, L. M., Bosch, C., Bullen, A., Burden, J. J., Carzaniga, R., Cheng, C., Darrow, M. C., Fletcher, G., Johnson, E. and Narayan, K. et al. (2023). Volume EM: a quiet revolution takes shape. *Nat Methods* **20**, 777–782. doi:10.1038/s41592-023-01861-8.

Conchello, J.-A. and Lichtman, J. W. (2005). Optical sectioning microscopy. *Nat Methods* **2**, 920–931. doi:10.1038/nmeth815.

Corsetti, S., Gunn-Moore, F. and Dholakia, K. (2019). Light sheet fluorescence microscopy for neuroscience. *Journal of Neuroscience Methods* **319**, 16–27. doi:10.1016/j.jneumeth.2018.07.011.

Daetwyler, S. and Fiolka, R. P. (2023). Light-sheets and smart microscopy, an exciting future is dawning. *Communications biology* **6**, 502. doi:10.1038/s42003-023-04857-4.

Dean, K. M., Roudot, P., Welf, E. S., Danuser, G. and Fiolka, R. (2015). Deconvolution-free Subcellular Imaging with Axially Swept Light Sheet Microscopy. *Biophysical journal* **108**, 2807–2815. doi:10.1016/j.bpj.2015.05.013.

Dekkers, J. F., Alieva, M., Wellens, L. M., Ariese, H. C. R., Jamieson, P. R., Vonk, A. M., Amatngalim, G. D., Hu, H., Oost, K. C. and Snippert, H. J. G. et al. (2019). High-resolution 3D imaging of fixed and cleared organoids. *Nature Protocols* **14**, 1756–1771. doi:10.1038/s41596-019-0160-8.

Denk, W., Strickler, J. H. and Webb, W. W. (1990). Two-photon laser scanning fluorescence microscopy. *Science (New York, N.Y.)* **248**, 73–76. doi:10.1126/science.2321027.

Denk, W. and Horstmann, H. (2004). Serial block-face scanning electron microscopy to reconstruct three-dimensional tissue nanostructure. *PLoS biology* **2**, e329. doi:10.1371/journal.pbio.0020329.

Di Lullo, E. and Kriegstein, A. R. (2017). The use of brain organoids to investigate neural development and disease. *Nature Reviews Neuroscience* **18**, 573–584. doi:10.1038/nrn.2017.107.

Dodt, H.-U. (2015). Microscopy. The superresolved brain. *Science (New York, N.Y.)* **347**, 474–475. doi:10.1126/science.aaa5084.

Dodt, H.-U., Leischner, U., Schierloh, A., Jährling, N., Mauch, C. P., Deininger, K., Deussing, J. M., Eder, M., Zieglgänsberger, W. and Becker, K. (2007). Ultramicroscopy: three-dimensional visualization of neuronal networks in the whole mouse brain. *Nat Methods* **4**, 331–336. doi:10.1038/nmeth1036.

Doerr, J., Schwarz, M. K., Wiedermann, D., Leinhaas, A., Jakobs, A., Schloen, F., Schwarz, I., Diedenhofen, M., Braun, N. C. and Koch, P. et al. (2017). Whole-brain 3D mapping of human neural transplant innervation. *Nature communications* **8**, 14162. doi:10.1038/ncomms14162.

Düring, D. N., Rocha, M. D., Dittrich, F., Gahr, M. and Hahnloser, R. H. R. (2019). Expansion Light Sheet Microscopy Resolves Subcellular Structures in Large Portions of the Songbird Brain. *Frontiers in neuroanatomy* **13**, 2. doi:10.3389/fnana.2019.00002.

Durkee, M. S., Abraham, R., Clark, M. R. and Giger, M. L. (2021). Artificial Intelligence and Cellular Segmentation in Tissue Microscopy Images. *The American journal of pathology* **191**, 1693–1701. doi:10.1016/j.ajpath.2021.05.022.

Ebeling, W., Hennrich, N., Klockow, M., Metz, H., Orth, H. D. and Lang, H. (1974). Proteinase K from Tritirachium album Limber. *European journal of biochemistry* **47**, 91–97. doi:10.1111/j.1432-1033.1974.tb03671.x.

Economo, M. N., Clack, N. G., Lavis, L. D., Gerfen, C. R., Svoboda, K., Myers, E. W. and Chandrashekar, J. (2016). A platform for brain-wide imaging and reconstruction of individual neurons. *eLife* **5**, e10566. doi:10.7554/eLife.10566.

Economo, M. N., Viswanathan, S., Tasic, B., Bas, E., Winnubst, J., Menon, V., Graybuck, L. T., Nguyen, T. N., Smith, K. A. and Yao, Z. et al. (2018). Distinct descending motor cortex pathways and their roles in movement. *Nature* **563**, 79–84. doi:10.1038/s41586-018-0642-9.

Edwards, S. J., Carannante, V., Kuhnigk, K., Ring, H., Tararuk, T., Hallböök, F., Blom, H., Önfelt, B. and Brismar, H. (2020). High-Resolution Imaging of Tumor Spheroids and Organoids Enabled by Expansion Microscopy. *Frontiers in Molecular Biosciences* **7**. doi:10.3389/fmolb.2020.00208.

Ellefsen, K. L. and Parker, I. (2018). Dynamic Ca2+ imaging with a simplified lattice light-sheet microscope: A sideways view of subcellular Ca2+ puffs. *Cell Calcium* **71**, 34–44. doi:10.1016/j.ceca.2017.11.005.

Fahrbach, F. O. and Rohrbach, A. (2012). Propagation stability of self-reconstructing Bessel beams enables contrast-enhanced imaging in thick media. *Nature communications* **3**, 632. doi:10.1038/ncomms1646.

Fish, K. N. (2009). Total internal reflection fluorescence (TIRF) microscopy. *Current protocols in cytometry* **Chapter 12**, Unit12.18. doi:10.1002/0471142956.cy1218s50.

Friedrich, M., Gan, Q., Ermolayev, V. and Harms, G. S. (2011). STED-SPIM: Stimulated emission depletion improves sheet illumination microscopy resolution. *Biophysical journal* **100**, L43-5. doi:10.1016/j.bpj.2010.12.3748.

Friedrichsen, K., Ramakrishna, P., Hsiang, J.-C., Valkova, K., Kerschensteiner, D. and Morgan, J. L. (2022). Reconstructing neural circuits using multiresolution correlated light and electron microscopy. *Frontiers in neural circuits* **16**, 753496. doi:10.3389/fncir.2022.753496.

Fu, Q., Martin, B. L., Matus, D. Q. and Gao, L. (2016). Imaging multicellular specimens with real-time optimized tiling light-sheet selective plane illumination microscopy. *Nature communications* **7**. doi:10.1038/ncomms11088.

Fujiwara, K. and Pollard, T. D. (1980). Chapter 12 Techniques for Localizing Contractile Proteins with Fluorescent Antibodies. In *Current Topics in Developmental Biology : Immunological Approaches to Embryonic Development and Differentiation Part II* (ed. A. A. Moscona and A. Monroy), pp. 271–296: Academic Press.

Gao, R., Asano, S. M., Upadhyayula, S., Pisarev, I., Milkie, D. E., Liu, T.-L., Singh, V., Graves, A., Huynh, G. H. and Zhao, Y. et al. (2019). Cortical column and whole-brain imaging with molecular contrast and nanoscale resolution. *Science* **363**. doi:10.1126/science.aau8302.

Germroth, P. G., Gourdie, R. G. and Thompson, R. P. (1995). Confocal microscopy of thick sections from acrylamide gel embedded embryos. *Microscopy research and technique* **30**, 513–520. doi:10.1002/jemt.1070300608.

Giandomenico, S. L., Mierau, S. B., Gibbons, G. M., Wenger, L. M. D., Masullo, L., Sit, T., Sutcliffe, M., Boulanger, J., Tripodi, M. and Derivery, E. et al. (2019). Cerebral organoids at the air–liquid interface generate diverse nerve tracts with functional output. *Nature Neuroscience* **22**, 669–679. doi:10.1038/s41593-019-0350-2.

Gong, S., Doughty, M., Harbaugh, C. R., Cummins, A., Hatten, M. E., Heintz, N. and Gerfen, C. R. (2007). Targeting Cre recombinase to specific neuron populations with bacterial artificial chromosome constructs. *The Journal of neuroscience : the official journal of the Society for Neuroscience* **27**, 9817–9823. doi:10.1523/JNEUROSCI.2707-07.2007.

Gonzalez (2009). *Digital Image Processing Using MATLAB*.

Guo, S., Xue, J., Liu, J., Ye, X., Guo, Y., Di Liu, Zhao, X., Xiong, F., Han, X. and Peng, H. (2022). Smart imaging to empower brain-wide neuroscience at single-cell levels. *Brain informatics* **9**, 10. doi:10.1186/s40708-022-00158-4.

Gustafsson, M. G. (2000). Surpassing the lateral resolution limit by a factor of two using structured illumination microscopy. *Journal of microscopy* **198**, 82–87. doi:10.1046/j.1365-2818.2000.00710.x.

Gustavsson, A.-K., Petrov, P. N. and Moerner, W. E. (2018). Light sheet approaches for improved precision in 3D localization-based super-resolution imaging in mammalian cells Invited. *Optics express* **26**, 13122–13147. doi:10.1364/OE.26.013122.

Hama, H., Kurokawa, H., Kawano, H., Ando, R., Shimogori, T., Noda, H., Fukami, K., Sakaue-Sawano, A. and Miyawaki, A. (2011). Scale: a chemical approach for fluorescence imaging and reconstruction of transparent mouse brain. *Nature Neuroscience* **14**, 1481–1488. doi:10.1038/nn.2928.

Haupts, U., Maiti, S., Schwille, P. and Webb, W. W. (1998). Dynamics of fluorescence fluctuations in green fluorescent protein observed by fluorescence correlation spectroscopy. *Proceedings of the National Academy of Sciences of the United States of America* **95**, 13573–13578. doi:10.1073/pnas.95.23.13573.

Hell, S. W. and Wichmann, J. (1994). Breaking the diffraction resolution limit by stimulated emission: stimulated-emission-depletion fluorescence microscopy. *Optics Letters* **19**, 780–782. doi:10.1364/OL.19.000780.

Helmchen, F. and Denk, W. (2005). Deep tissue two-photon microscopy. *Nat Methods* **2**, 932–940. doi:10.1038/nmeth818.

Huisken, J., Swoger, J., Del Bene, F., Wittbrodt, J. and Stelzer, E. H. K. (2004). Optical sectioning deep inside live embryos by selective plane illumination microscopy. *Science (New York, N.Y.)* **305**, 1007–1009. doi:10.1126/science.1100035.

Iefremova, V., Manikakis, G., Krefft, O., Jabali, A., Weynans, K., Wilkens, R., Marsoner, F., Brändl, B., Müller, F.-J. and Koch, P. et al. (2017). An Organoid-Based Model of Cortical Development Identifies Non-Cell-Autonomous Defects in Wnt Signaling Contributing to Miller-Dieker Syndrome. *Cell Reports* **19**, 50–59. doi:10.1016/j.celrep.2017.03.047.

Igarashi, M., Nozumi, M., Wu, L.-G., Cella Zanacchi, F., Katona, I., Barna, L., Xu, P., Zhang, M., Xue, F. and Boyden, E. (2018). New observations in neuroscience using superresolution microscopy. *The Journal of neuroscience : the official journal of the Society for Neuroscience* **38**, 9459–9467. doi:10.1523/JNEUROSCI.1678-18.2018.

Jain, A., Yang, A. H. J. and Erickson, D. (2012). Gel-based optical waveguides with live cell encapsulation and integrated microfluidics. *Optics Letters* **37**, 1472–1474. doi:10.1364/OL.37.001472.

Jain, V., Seung, H. S. and Turaga, S. C. (2010). Machines that learn to segment images: a crucial technology for connectomics. *Current opinion in neurobiology* **20**, 653–666. doi:10.1016/j.conb.2010.07.004.

Jorgenson, L. A., Newsome, W. T., Anderson, D. J., Bargmann, C. I., Brown, E. N., Deisseroth, K., Donoghue, J. P., Hudson, K. L., Ling, G. S. F. and MacLeish, P. R. et al. (2015). The BRAIN Initiative: developing technology to catalyse neuroscience discovery. *Philosophical transactions of the Royal Society of London. Series B, Biological sciences* **370**. doi:10.1098/rstb.2014.0164.

Kashiwagi, Y., Higashi, T., Obashi, K., Sato, Y., Komiyama, N. H., Grant, S. G. N. and Okabe, S. (2019). Computational geometry analysis of dendritic spines by structured illumination microscopy. *Nature communications* **10**, 1285. doi:10.1038/s41467-019-09337-0.

Kashiwagi, Y. and Okabe, S. (2021). Imaging of spine synapses using super-resolution microscopy. *Anatomical science international* **96**, 343–358. doi:10.1007/s12565-021-00603-0.

Keller, P. J. (2013). In vivo imaging of zebrafish embryogenesis. *Methods (San Diego, Calif.)* **62**, 268–278. doi:10.1016/j.ymeth.2013.03.015.

Keller, P. J. and Ahrens, M. B. (2015). Visualizing whole-brain activity and development at the single-cell level using light-sheet microscopy. *Neuron* **85**, 462–483. doi:10.1016/j.neuron.2014.12.039.

Keller, P. J. and Dodt, H.-U. (2012). Light sheet microscopy of living or cleared specimens. *Current opinion in neurobiology* **22**, 138–143. doi:10.1016/j.conb.2011.08.003.

Keller, P. J., Schmidt, A. D., Wittbrodt, J. and Stelzer, E. H. K. (2008). Reconstruction of zebrafish early embryonic development by scanned light sheet microscopy. *Science* **322**, 1065–1069. doi:10.1126/science.1162493.

Khairy, K. and Keller, P. J. (2011). Reconstructing embryonic development. *Genesis (New York, N.Y. : 2000)* **49**, 488–513. doi:10.1002/dvg.20698.

Kiernan, J. A. (2000). Formaldehyde, Formalin, Paraformaldehyde And Glutaraldehyde: What They Are And What They Do. *Micros. Today* **8**, 8–13. doi:10.1017/S1551929500057060.

Kim, S.-Y., Chung, K. and Deisseroth, K. (2013). Light microscopy mapping of connections in the intact brain. *Trends in cognitive sciences* **17**, 596–599. doi:10.1016/j.tics.2013.10.005.

Kita, T. and Kita, H. (2012). The subthalamic nucleus is one of multiple innervation sites for long-range corticofugal axons: a single-axon tracing study in the rat. *The Journal of neuroscience : the official journal of the Society for Neuroscience* **32**, 5990–5999. doi:10.1523/JNEUROSCI.5717-11.2012.

Kneen, M., Farinas, J., Li, Y. and Verkman, A. S. (1998). Green fluorescent protein as a noninvasive intracellular pH indicator. *Biophysical journal* **74**, 1591–1599. doi:10.1016/S0006-3495(98)77870-1.

Koorman, T., Jansen, K. A., Khalil, A., Haughton, P. D., Visser, D., Rätze, M. A. K., Haakma, W. E., Sakalauskaitè, G., van Diest, P. J. and Rooij, J. de et al. (2022). Spatial collagen stiffening promotes collective breast cancer cell invasion by reinforcing extracellular matrix alignment. *Oncogene* **41**, 2458–2469. doi:10.1038/s41388-022-02258-1.

Korobchevskaya, K., Lagerholm, B., Colin-York, H. and Fritzsche, M. (2017). Exploring the Potential of Airyscan Microscopy for Live Cell Imaging. *Photonics* **4**, 41. doi:10.3390/photonics4030041.

Kromm, D., Thumberger, T. and Wittbrodt, J. (2016). Chapter 5 - An eye on light-sheet microscopy. In *Methods in Cell Biology : The Zebrafish* (ed. H. W. Detrich, M. Westerfield and L. I. Zon), pp. 105–123: Academic Press.

Ku, T., Swaney, J., Park, J.-Y., Albanese, A., Murray, E., Cho, J. H., Park, Y.-G., Mangena, V., Chen, J. and Chung, K. (2016). Multiplexed and scalable super-resolution imaging of three-dimensional protein localization in size-adjustable tissues. *Nature biotechnology* **34**, 973–981. doi:10.1038/nbt.3641.

Kubitscheck, U., ed. (2017). *Fluorescence microscopy: From principles to biological applications / edited by Ulrich Kubitscheck*. Weinheim: Wiley-VCH.

LaMonica, B. E., Lui, J. H., Hansen, D. V. and Kriegstein, A. R. (2013). Mitotic spindle orientation predicts outer radial glial cell generation in human neocortex. *Nature communications* **4**. doi:10.1038/ncomms2647.

Lancaster, M. A., Corsini, N. S., Wolfinger, S., Gustafson, E. H., Phillips, A. W., Burkard, T. R., Otani, T., Livesey, F. J. and Knoblich, J. A. (2017). Guided self-organization and cortical plate formation in human brain organoids. *Nature biotechnology* **35**, 659–666. doi:10.1038/nbt.3906.

Lancaster, M. A., Renner, M., Martin, C.-A., Wenzel, D., Bicknell, L. S., Hurles, M. E., Homfray, T., Penninger, J. M., Jackson, A. P. and Knoblich, J. A. (2013). Cerebral organoids model human brain development and microcephaly. *Nature* **501**, 373–379. doi:10.1038/nature12517.

Lelek, M., Gyparaki, M. T., Beliu, G., Schueder, F., Griffié, J., Manley, S., Jungmann, R., Sauer, M., Lakadamyali, M. and Zimmer, C. (2021). Single-molecule localization microscopy. *Nature reviews. Methods primers* **1**. doi:10.1038/s43586-021-00038-x.

Li, A., Gong, H., Zhang, B., Wang, Q., Yan, C., Wu, J., Liu, Q., Zeng, S. and Luo, Q. (2010). Micro-optical sectioning tomography to obtain a high-resolution atlas of the mouse brain. *Science* **330**, 1404–1408. doi:10.1126/science.1191776.

Lichtman, J. W., Pfister, H. and Shavit, N. (2014). The big data challenges of connectomics. *Nature Neuroscience* **17**, 1448–1454. doi:10.1038/nn.3837.

Lichtman, J. W. and Sanes, J. R. (2008). Ome sweet ome: what can the genome tell us about the connectome? *Current opinion in neurobiology* **18**, 346–353. doi:10.1016/j.conb.2008.08.010.

Lin, H.-Y., Chu, L.-A., Yang, H., Hsu, K.-J., Lin, Y.-Y., Lin, K.-H., Chu, S.-W. and Chiang, A.-S. (2019). Imaging through the Whole Brain of Drosophila at λ/20 Super-resolution. *iScience* **14**, 164–170. doi:10.1016/j.isci.2019.03.025.

Madhusoodanan, J. (2023). Smart microscopes spot fleeting biology. *Nature* **614**, 378–380. doi:10.1038/d41586-023-00336-2.

Mansour, A. A., Gonçalves, J. T., Bloyd, C. W., Li, H., Fernandes, S., Quang, D., Johnston, S., Parylak, S. L., Jin, X. and Gage, F. H. (2018). An in vivo model of functional and vascularized human brain organoids. *Nature biotechnology* **36**, 432–441. doi:10.1038/nbt.4127.

Mappes, T., Jahr, N., Csaki, A., Vogler, N., Popp, J. and Fritzsche, W. (2012). The invention of immersion ultramicroscopy in 1912-the birth of nanotechnology? *Angewandte Chemie International Edition* **51**, 11208–11212. doi:10.1002/anie.201204688.

Masselink, W., Reumann, D., Murawala, P., Pasierbek, P., Taniguchi, Y., Bonnay, F., Meixner, K., Knoblich, J. A. and Tanaka, E. M. (2019). Broad applicability of a streamlined Ethyl Cinnamate-based clearing procedure. *Development*. doi:10.1242/dev.166884.

Mayerich, D., Abbott, L. and McCormick, B. (2008). Knife-edge scanning microscopy for imaging and reconstruction of three-dimensional anatomical structures of the mouse brain. *Journal of microscopy* **231**, 134–143. doi:10.1111/j.1365-2818.2008.02024.x.

Memarhosseini, S. (2016). Characterization and Evaluation of Expansion Microscopy on Light Sheet Fluorescence Microscopy. *Master Thesis,* **Rheinische Friedrich-Wilhelms-Universität Bonn**, Bonn, Germany.

Mertz, J. and Kim, J. (2010). Scanning light-sheet microscopy in the whole mouse brain with HiLo background rejection. *Journal of biomedical optics* **15**, 16027. doi:10.1117/1.3324890.

Method of the Year 2014 (2015). *Nat Methods* **12**, 1. doi:10.1038/nmeth.3251.

Micheva, K. D., Busse, B., Weiler, N. C., O'Rourke, N. and Smith, S. J. (2010). Single-synapse analysis of a diverse synapse population: proteomic imaging methods and markers. *Neuron* **68**, 639–653. doi:10.1016/j.neuron.2010.09.024.

Migliori, B., Datta, M. S., Dupre, C., Apak, M. C., Asano, S., Gao, R., Boyden, E. S., Hermanson, O., Yuste, R. and Tomer, R. (2018). Light sheet theta microscopy for rapid high-resolution imaging of large biological samples. *BMC biology* **16**, 57. doi:10.1186/s12915-018-0521-8.

Mikula, S. and Denk, W. (2015). High-resolution whole-brain staining for electron microscopic circuit reconstruction. *Nat Methods* **12**, 541–546. doi:10.1038/nmeth.3361.

Minsky, M. (1988). Memoir on inventing the confocal scanning microscope. *Scanning* **10**, 128–138. doi:10.1002/sca.4950100403.

Mohan, S. C., Lee, T.-Y., Giuliano, A. E. and Cui, X. (2021). Current Status of Breast Organoid Models. *Frontiers in bioengineering and biotechnology* **9**, 745943. doi:10.3389/fbioe.2021.745943.

Möller-Kerutt, A., Rodriguez-Gatica, J. E., Wacker, K., Bhatia, R., Siebrasse, J.-P., Boon, N., van Marck, V., Boor, P., Kubitscheck, U. and Wijnholds, J. et al. (2021). Crumbs2 Is an Essential Slit Diaphragm Protein of the Renal Filtration Barrier. *Journal of the American Society of Nephrology : JASN* **32**, 1053–1070. doi:10.1681/ASN.2020040501.

Motta, A., Schurr, M., Staffler, B. and Helmstaedter, M. (2019). Big data in nanoscale connectomics, and the greed for training labels. *Current opinion in neurobiology* **55**, 180–187. doi:10.1016/j.conb.2019.03.012.

Nägerl, U. V., Willig, K. I., Hein, B., Hell, S. W. and Bonhoeffer, T. (2008). Live-cell imaging of dendritic spines by STED microscopy. *Proceedings of the National Academy of Sciences of the United States of America* **105**, 18982–18987. doi:10.1073/pnas.0810028105.

Neil, M. A., Juskaitis, R. and Wilson, T. (1997). Method of obtaining optical sectioning by using structured light in a conventional microscope. *Optics Letters* **22**, 1905–1907. doi:10.1364/OL.22.001905.

Neyra, E. G., Martínez-Matos, Ó. and Vaveliuk, P. (2020). Ultra-long light sheets via curved beam intercrossing. *OSA Continuum* **3**, 2062. doi:10.1364/OSAC.393073.

Oeller, M. (2016). Expansion Microscopy. *Bachelor Thesis,* **Rheinische Friedrich-Wilhelms-Universität Bonn**, Bonn, Germany.

Oh, S. W., Harris, J. A., Ng, L., Winslow, B., Cain, N., Mihalas, S., Wang, Q., Lau, C., Kuan, L. and Henry, A. M. et al. (2014). A mesoscale connectome of the mouse brain. *Nature* **508**, 207–214. doi:10.1038/nature13186.

Osten, P. and Margrie, T. W. (2013). Mapping brain circuitry with a light microscope. *Nat Methods* **10**, 515–523. doi:10.1038/nmeth.2477.

Paşca, A. M., Sloan, S. A., Clarke, L. E., Tian, Y., Makinson, C. D., Huber, N., Kim, C. H., Park, J.-Y., O'Rourke, N. A. and Nguyen, K. D. et al. (2015). Functional cortical neurons and astrocytes from human pluripotent stem cells in 3D culture. *Nature methods* **12**, 671–678. doi:10.1038/nmeth.3415.

Peddie, C. J., Genoud, C., Kreshuk, A., Meechan, K., Micheva, K. D., Narayan, K., Pape, C., Parton, R. G., Schieber, N. L. and Schwab, Y. et al. (2022). Volume electron microscopy. *Nat Rev Methods Primers* **2**. doi:10.1038/s43586-022-00131-9.

Peitz, M., Krutenko, T. and Brüstle, O. (2020). Protocol for the Standardized Generation of Forward Programmed Cryopreservable Excitatory and Inhibitory Forebrain Neurons. *STAR Protocols* **1**, 100038. doi:10.1016/j.xpro.2020.100038.

Planchon, T. A., Gao, L., Milkie, D. E., Davidson, M. W., Galbraith, J. A., Galbraith, C. G. and Betzig, E. (2011). Rapid three-dimensional isotropic imaging of living cells using Bessel beam plane illumination. *Nat Methods* **8**, 417–423. doi:10.1038/nmeth.1586.

Pollen, A. A., Bhaduri, A., Andrews, M. G., Nowakowski, T. J., Meyerson, O. S., Mostajo-Radji, M. A., Di Lullo, E., Alvarado, B., Bedolli, M. and Dougherty, M. L. et al. (2019). Establishing Cerebral Organoids as Models of Human-Specific Brain Evolution. *Cell* **176**, 743-756.e17. doi:10.1016/j.cell.2019.01.017.

Power, R. M. and Huisken, J. (2017). A guide to light-sheet fluorescence microscopy for multiscale imaging. *Nat Methods* **14**, 360–373. doi:10.1038/nmeth.4224.

Preibisch, S., Saalfeld, S. and Tomancak, P. (2009). Globally optimal stitching of tiled 3D microscopic image acquisitions. *Bioinformatics (Oxford, England)* **25**, 1463–1465. doi:10.1093/bioinformatics/btp184.

Qian, K., Huang, C.-L., Chen, H., Blackbourn, L. W., Chen, Y., Cao, J., Yao, L., Sauvey, C., Du, Z. and Zhang, S.-C. (2014). A Simple and Efficient System for Regulating Gene Expression in Human Pluripotent Stem Cells and Derivatives. *STEM CELLS* **32**, 1230–1238. doi:10.1002/stem.1653.

Qian, X., Song, H. and Ming, G. (2019). Brain organoids: advances, applications and challenges. *Development* **146**. doi:10.1242/dev.166074.

Quadrato, G., Brown, J. and Arlotta, P. (2016). The promises and challenges of human brain organoids as models of neuropsychiatric disease. *Nature Medicine* **22**, 1220–1228. doi:10.1038/nm.4214.

Quadrato, G., Nguyen, T., Macosko, E. Z., Sherwood, J. L., Min Yang, S., Berger, D. R., Maria, N., Scholvin, J., Goldman, M. and Kinney, J. P. et al. (2017). Cell diversity and network dynamics in photosensitive human brain organoids. *Nature* **545**, 48–53. doi:10.1038/nature22047.

Ragan, T., Kadiri, L. R., Venkataraju, K. U., Bahlmann, K., Sutin, J., Taranda, J., Arganda-Carreras, I., Kim, Y., Seung, H. S. and Osten, P. (2012). Serial two-photon tomography for automated ex vivo mouse brain imaging. *Nat Methods* **9**, 255–258. doi:10.1038/nmeth.1854.

Ravindran, S. (2022). Five ways deep learning has transformed image analysis. *Nature* **609**, 864–866. doi:10.1038/d41586-022-02964-6.

Richardson, D. S. and Lichtman, J. W. (2015). Clarifying Tissue Clearing. *Cell* **162**, 246–257. doi:10.1016/j.cell.2015.06.067.

Ritter, J. G., Veith, R., Siebrasse, J.-P. and Kubitscheck, U. (2008). High-contrast single-particle tracking by selective focal plane illumination microscopy. *Optics express* **16**, 7142–7152. doi:10.1364/oe.16.007142.

Ritter, J. G., Veith, R., Veenendaal, A., Siebrasse, J. P. and Kubitscheck, U. (2010). Light sheet microscopy for single molecule tracking in living tissue. *PloS one* **5**, e11639. doi:10.1371/journal.pone.0011639.

Robinson, R. W. and Snyder, J. A. (2004). An innovative fixative for cytoskeletal components allows high resolution in colocalization studies using immunofluorescence techniques. *Histochem Cell Biol* **122**, 1–5. doi:10.1007/s00418-004-0656-2.

Rodriguez-Gatica, J. E., Iefremova, V., Sokhranyaeva, L., Yeung, Si Wah Christina Au, Breitkreuz, Y., Brüstle, O., Schwarz, M. K. and Kubitscheck, U. (2022). Imaging three-dimensional brain organoid architecture from meso- to nanoscale across development. *Development* **149**. doi:10.1242/dev.200439.

Rust, M. J., Bates, M. and Zhuang, X. (2006). Sub-diffraction-limit imaging by stochastic optical reconstruction microscopy (STORM). *Nature methods* **3**, 793–795. doi:10.1038/nmeth929.

Saleh, B. E. A. and Teich, M. C. (2013). *Fundamentals of photonics*. Hoboken, N.J.: John Wiley & Sons.

Sawada, K., Kawakami, R., Shigemoto, R. and Nemoto, T. (2018). Super-resolution structural analysis of dendritic spines using three-dimensional structured illumination microscopy in cleared mouse brain slices. *The European journal of neuroscience* **47**, 1033–1042. doi:10.1111/ejn.13901.

Schindelin, J., Arganda-Carreras, I., Frise, E., Kaynig, V., Longair, M., Pietzsch, T., Preibisch, S., Rueden, C., Saalfeld, S. and Schmid, B. et al. (2012). Fiji: an open-source platform for biological-image analysis. *Nat Methods* **9**, 676–682. doi:10.1038/nmeth.2019.

Schmid, B., Shah, G., Scherf, N., Weber, M., Thierbach, K., Campos, C. P., Roeder, I., Aanstad, P. and Huisken, J. (2013). High-speed panoramic light-sheet microscopy reveals global endodermal cell dynamics. *Nat Commun* **4**, 2207. doi:10.1038/ncomms3207.

Schneider-Mizell, C. M., Gerhard, S., Longair, M., Kazimiers, T., Li, F., Zwart, M. F., Champion, A., Midgley, F. M., Fetter, R. D. and Saalfeld, S. et al. (2016). Quantitative neuroanatomy for connectomics in Drosophila. *eLife* **5**. doi:10.7554/eLife.12059.

Schwarz, M. K. and Kubitscheck, U. (2022). Expansion light sheet fluorescence microscopy of extended biological samples: Applications and perspectives. *Progress in Biophysics and Molecular Biology* **168**, 33–36. doi:10.1016/j.pbiomolbio.2021.09.004.

Schwarz, M. K., Scherbarth, A., Sprengel, R., Engelhardt, J., Theer, P. and Giese, G. (2015). Fluorescent-protein stabilization and high-resolution imaging of cleared, intact mouse brains. *PloS one* **10**, e0124650. doi:10.1371/journal.pone.0124650.

Serrano, M. E., Kim, E., Petrinovic, M. M., Turkheimer, F. and Cash, D. (2022). Imaging Synaptic Density: The Next Holy Grail of Neuroscience? *Frontiers in Neuroscience* **16**, 796129. doi:10.3389/fnins.2022.796129.

Siedentopf, H. and Zsigmondy, R. (1902). Uber Sichtbarmachung und Größenbestimmung ultramikoskopischer Teilchen, mit besonderer Anwendung auf Goldrubingläser. *Ann. Phys.* **315**, 1–39. doi:10.1002/andp.19023150102.

Silvestri, L., Bria, A., Sacconi, L., Iannello, G. and Pavone, F. S. (2012). Confocal light sheet microscopy: micron-scale neuroanatomy of the entire mouse brain. *Optics express* **20**, 20582–20598. doi:10.1364/OE.20.020582.

Stelzer, E. H. K. (2015). Light-sheet fluorescence microscopy for quantitative biology. *Nat Methods* **12**, 23–26. doi:10.1038/nmeth.3219.

Stelzer, E. H. K., Strobl, F., Chang, B.-J., Preusser, F., Preibisch, S., McDole, K. and Fiolka, R. (2021). Light sheet fluorescence microscopy. *Nat Rev Methods Primers* **1**. doi:10.1038/s43586-021-00069-4.

Stockhausen, A., Bürgers, J., Rodriguez-Gatica, J. E., Schweihoff, J., Merkel, R., Prigge, J. M., Schwarz, M. K. and Kubitscheck, U. (2020). Hard-wired lattice light-sheet microscopy for imaging of expanded samples. *Optics express* **28**, 15587–15600. doi:10.1364/OE.393728.

Susaki, E. A., Tainaka, K., Perrin, D., Kishino, F., Tawara, T., Watanabe, T. M., Yokoyama, C., Onoe, H., Eguchi, M. and Yamaguchi, S. et al. (2014). Whole-brain imaging with single-cell resolution using chemical cocktails and computational analysis. *Cell* **157**, 726–739. doi:10.1016/j.cell.2014.03.042.

Tainaka, K., Kuno, A., Kubota, S. I., Murakami, T. and Ueda, H. R. (2016). Chemical Principles in Tissue Clearing and Staining Protocols for Whole-Body Cell Profiling. *Annual review of cell and developmental biology* **32**, 713–741. doi:10.1146/annurev-cellbio-111315-125001.

Tanaka, T., Fillmore, D., Sun, S.-T., Nishio, I., Swislow, G. and Shah, A. (1980). Phase Transitions in Ionic Gels. *Phys. Rev. Lett.* **45**, 1636–1639. doi:10.1103/PhysRevLett.45.1636.

Tang, J., Germain, R. N. and Cui, M. (2012). Superpenetration optical microscopy by iterative multiphoton adaptive compensation technique. *Proceedings of the National Academy of Sciences of the United States of America* **109**, 8434–8439. doi:10.1073/pnas.1119590109.

Tillberg, P. W. and Chen, F. (2019). Expansion Microscopy: Scalable and Convenient Super-Resolution Microscopy. *Annual review of cell and developmental biology* **35**, 683–701. doi:10.1146/annurev-cellbio-100818-125320.

Tillberg, P. W., Chen, F., Piatkevich, K. D., Zhao, Y., Yu, C.-C. J., English, B. P., Gao, L., Martorell, A., Suk, H.-J. and Yoshida, F. et al. (2016). Protein-retention expansion microscopy of cells and tissues labeled using standard fluorescent proteins and antibodies. *Nature biotechnology* **34**, 987–992. doi:10.1038/nbt.3625.

Titze, B. and Genoud, C. (2016). Volume scanning electron microscopy for imaging biological ultrastructure. *Biology of the Cell* **108**, 307–323. doi:10.1111/boc.201600024.

Toomre, D. and Bewersdorf, J. (2010). A new wave of cellular imaging. *Annual review of cell and developmental biology* **26**, 285–314. doi:10.1146/annurev-cellbio-100109-104048.

Truong, T. V., Supatto, W., Koos, D. S., Choi, J. M. and Fraser, S. E. (2011). Deep and fast live imaging with two-photon scanned light-sheet microscopy. *Nat Methods* **8**, 757–760. doi:10.1038/nmeth.1652.

Tsien, R. Y. (2009). Constructing and exploiting the fluorescent protein paintbox (Nobel Lecture). *Angewandte Chemie International Edition* **48**, 5612–5626. doi:10.1002/anie.200901916.

Ueda, H. R., Ertürk, A., Chung, K., Gradinaru, V., Chédotal, A., Tomancak, P. and Keller, P. J. (2020). Tissue clearing and its applications in neuroscience. *Nature Reviews Neuroscience* **21**, 61–79. doi:10.1038/s41583-019-0250-1.

Velasco, S., Kedaigle, A. J., Simmons, S. K., Nash, A., Rocha, M., Quadrato, G., Paulsen, B., Nguyen, L., Adiconis, X. and Regev, A. et al. (2019). Individual brain organoids reproducibly form cell diversity of the human cerebral cortex. *Nature* **570**, 523–527. doi:10.1038/s41586-019-1289-x.

Vettenburg, T., Dalgarno, H. I. C., Nylk, J., Coll-Lladó, C., Ferrier, D. E. K., Čižmár, T., Gunn-Moore, F. J. and Dholakia, K. (2014). Light-sheet microscopy using an Airy beam. *Nat Methods* **11**, 541–544. doi:10.1038/nmeth.2922.

Vigouroux, R. J., Belle, M. and Chédotal, A. (2017). Neuroscience in the third dimension: shedding new light on the brain with tissue clearing. *Molecular brain* **10**, 33. doi:10.1186/s13041-017-0314-y.

Voie, A. H., Burns, D. H. and Spelman, F. A. (1993). Orthogonal-plane fluorescence optical sectioning: three-dimensional imaging of macroscopic biological specimens. *Journal of microscopy* **170**, 229–236. doi:10.1111/j.1365-2818.1993.tb03346.x.

Vu, M.-A. T., Adalı, T., Ba, D., Buzsáki, G., Carlson, D., Heller, K., Liston, C., Rudin, C., Sohal, V. S. and Widge, A. S. et al. (2018). A Shared Vision for Machine Learning in Neuroscience. *The Journal of neuroscience : the official journal of the Society for Neuroscience* **38**, 1601–1607. doi:10.1523/JNEUROSCI.0508-17.2018.

Wan, Y., McDole, K. and Keller, P. J. (2019). Light-Sheet Microscopy and Its Potential for Understanding Developmental Processes. *Annual review of cell and developmental biology* **35**, 655–681. doi:10.1146/annurev-cellbio-100818-125311.

Wen, G., Vanheusden, M., Acke, A., Valli, D., Neely, R. K., Leen, V. and Hofkens, J. (2020). Evaluation of Direct Grafting Strategies via Trivalent Anchoring for Enabling Lipid Membrane and Cytoskeleton Staining in Expansion Microscopy. *ACS nano* **14**, 7860–7867. doi:10.1021/acsnano.9b09259.

Werner, C., Sauer, M. and Geis, C. (2021). Super-resolving Microscopy in Neuroscience. *Chemical reviews* **121**, 11971–12015. doi:10.1021/acs.chemrev.0c01174.

Winding, M., Pedigo, B. D., Barnes, C. L., Patsolic, H. G., Park, Y., Kazimiers, T., Fushiki, A., Andrade, I. V., Khandelwal, A. and Valdes-Aleman, J. et al. (2023). The connectome of an insect brain. *Science (New York, N.Y.)* **379**, eadd9330. doi:10.1126/science.add9330.

Yakoub, A. M. and Sadek, M. (2019). Analysis of Synapses in Cerebral Organoids. *Cell transplantation* **28**, 1173–1182. doi:10.1177/0963689718822811.

Yang, B., Treweek, J. B., Kulkarni, R. P., Deverman, B. E., Chen, C.-K., Lubeck, E., Shah, S., Cai, L. and Gradinaru, V. (2014). Single-cell phenotyping within transparent intact tissue through whole-body clearing. *Cell* **158**, 945–958. doi:10.1016/j.cell.2014.07.017.

Yang, X., Zhang, Q., Huang, F., Bai, K., Guo, Y., Zhang, Y., Li, N., Cui, Y., Sun, P. and Zeng, S. et al. (2018). High-throughput light sheet tomography platform for automated fast imaging of whole mouse brain. *Journal of biophotonics* **11**, e201800047. doi:10.1002/jbio.201800047.

Yingling, J., Youn, Y. H., Darling, D., Toyo-oka, K., Pramparo, T., Hirotsune, S. and Wynshaw-Boris, A. (2008). Neuroepithelial Stem Cell Proliferation Requires LIS1 for Precise Spindle Orientation and Symmetric Division. *Cell* **132**, 474–486. doi:10.1016/j.cell.2008.01.026.

Zhao, S., Todorov, M. I., Cai, R., -Maskari, R. A. I., Steinke, H., Kemter, E., Mai, H., Rong, Z., Warmer, M. and Stanic, K. et al. (2020). Cellular and Molecular Probing of Intact Human Organs. *Cell* **180**, 796-812.e19. doi:10.1016/j.cell.2020.01.030.

Zhu, D., Larin, K. V., Luo, Q. and Tuchin, V. V. (2013). Recent progress in tissue optical clearing. *Laser & photonics reviews* **7**, 732–757. doi:10.1002/lpor.201200056.

Zhu, X., Xia, Y., Wang, X., Si, K. and Gong, W. (2017). Optical Brain Imaging: A Powerful Tool for Neuroscience. *Neuroscience bulletin* **33**, 95–102. doi:10.1007/s12264-016-0053-6.

List of Figures

Appendix A1

Appendix A2

Appendix A3

Acknowledgments

First and foremost, I extend my deepest gratitude to Prof. Ulrich Kubitscheck for entrusting me with such a riveting and challenging research topic. His unwavering support, coupled with the autonomy he granted me in pursuing my research questions, has been invaluable. I am also indebted for the numerous enriching conferences and workshops, both domestic and international, that I had the privilege to attend during my PhD journey.

My sincere thanks go to Prof. Dr. Rudolf Merkel for graciously accepting the role of the second reviewer. I am also grateful to Prof. Dr. Arne Lützen and Prof. Dr. Benjamin Odermatt for their prompt and kind willingness to be part of the review committee.

A special mention to Dr. Martin Schwarz, whose expertise in neuroscience was instrumental in translating my ideas into tangible results. His dedication, despite his commitments, in offering guidance and reviewing my work is deeply appreciated. To his team, my gratitude extends to Dr. Jens Tillman, Lydia Fisher, and especially Irina Kim for their invaluable assistance and insightful discussions.

I am thankful to Prof. Dr. Oliver Brüstle for our productive collaboration and, in particular, to Dr. Vira Iefremova for our engaging discussions and collaboration on our recent work.

Dr. Jan-Peter Siebrasse deserves special mention. With his broad knowledge of microscopy and data analysis, his invaluable feedback during the group presentations, during the grills and in every conversation has been of great support.

My appreciation goes to the staff of the precision mechanics and the electronics workshop of the Institute of Physical and Theoretical Chemistry, in particular, to Mr. Daniel Poetes and Mr. Rolf Paulig for their expertise and innovative ideas for the construction of numerous microscope components. I would also like to thank Knut Hintzen for his support in solving IT challenges.

A big thank you to both, past and present members of the Biophysical Chemistry working group for fostering a pleasant working atmosphere, their warm welcome, and their work- and cultural integration, especially during my first days. For the invaluable help with the German bureaucracy (to this day). To all, thanks for the camaraderie, trust and shared moments in the lab and beyond. The video game nights, barbecues and our collective attempts at exercise have been memorable.

I am grateful to ANID (Chilean National Commission for Scientific and Technological Research) and DAAD (German Academic Exchange Service) for their financial support.

On a personal note, my heartfelt thanks to my mother, siblings, and in-laws for their unwavering support and belief in me. To my friends in Bonn-Köln, for the countless moments of relaxation, laughter, and shared beers, thank you.

Last but certainly not least, my deepest gratitude to my wife, Fernanda. Her unwavering support and encouragement have been my pillar of strength. This journey would not have been possible without her by my side.

Appendices

A1. First paper: Light sheet fluorescence expansion microscopy: Fast mapping of neural circuits at super resolution

Reproduced with permission from

Bürgers, J., Pavlova, I., Rodriguez-Gatica, J. E., Henneberger, C., Oeller, M., Ruland, J. A., Siebrasse, J. P., Kubitscheck, U. and Schwarz, M. K. (**2019**). Light-sheet fluorescence expansion microscopy: fast mapping of neural circuits at super resolution. Neurophotonics 6, 15005.

DOI: https://doi.org/10.1117/1.NPh.6.1.015005

Contributions

- Part of sample preparation
- Part of data acquisition
- Data analysis
- Writing the manuscript

Neurophotonics 6(1), 015005 (Jan–Mar 2019)

Light-sheet fluorescence expansion microscopy: fast mapping of neural circuits at super resolution

Jana Bürgers,[a,†] Irina Pavlova,[b,†] Juan E. Rodriguez-Gatica,[a,†] Christian Henneberger,[c,d] Marc Oeller,[a] Jan A. Ruland,[a] Jan P. Siebrasse,[a] Ulrich Kubitscheck,[a,*] and Martin K. Schwarz[b,*]
[a]University of Bonn, Institute of Physical and Theoretical Chemistry, Bonn, Germany
[b]University of Bonn Medical School, Institute of Experimental Epileptology and Cognition Research, Bonn, Germany
[c]University of Bonn Medical School, Institute of Cellular Neurosciences, German Center for Neurodegenerative Diseases, Bonn, Germany
[d]University College London, Institute of Neurology, London, United Kingdom

Abstract. The goal of understanding the architecture of neural circuits at the synapse level with a brain-wide perspective has powered the interest in high-speed and large field-of-view volumetric imaging at subcellular resolution. Here, we developed a method combining tissue expansion and light-sheet fluorescence microscopy to allow extended volumetric super resolution high-speed imaging of large mouse brain samples. We demonstrate the capabilities of this method by performing two color fast volumetric super resolution imaging of mouse CA1 and dentate gyrus molecular-, granule cell-, and polymorphic layers. Our method enables an exact evaluation of granule cell and neurite morphology within the context of large cell ensembles spanning several orders of magnitude in resolution. We found that imaging a brain region of 1 mm^3 in super resolution using light-sheet fluorescence expansion microscopy is about 17-fold faster than imaging the same region by a current state-of-the-art high-resolution confocal laser scanning microscope. [DOI: 10.1117/1.NPh.6.1.015005]

Keywords: connectomics; super resolution; tissue expansion; dentate gyrus; light-sheet fluorescence microscopy.

Paper 18043RR received Aug. 8, 2018; accepted for publication Jan. 9, 2019; published online Feb. 8, 2019.

1 Introduction

One of the prime goals in today's neuroscience is the volumetric architectural mapping of neural circuits spanning several magnitudes of resolution, i.e., imaging large fields of view up to several millimeters in super resolution, preferably using a single, straightforward light microscopic process. This challenge has drawn the attention of scientists beginning with Ramon y Cajal, who used the Golgi technique to draw detailed pictures of neurons containing most of their neurites[1] and culminates in today's electron microscopy (EM), which allows to decode the finest details of neuronal circuit structure.[2] EM's key advantage is the possibility to identify and distinguish presynaptic active zones containing synaptic vesicles from apposed postsynaptic structures and the visualization of even the finest axonal branches. However, EM connectivity mapping is extremely time consuming and requires expensive high-tech systems, both for image acquisition and image analysis. Most importantly, the sample contrast preparation is largely incompatible with rich molecular phenotyping, which can provide critical information on cell and synapse type. Thus, an ideal analysis method would generate super resolution data sets, allowing to reconstruct the critical details of synaptic connectivity from intact brain samples linked to the molecular information on the types of cells and synapses and even to dynamic information on natural activity pattern history, which is causally relevant to animal behavior.

To date light-based imaging approaches combined with specific genetic labeling methods are important tools to visualize the structural and functional architecture of nervous tissue in high resolution.[3] Confocal microscopy allows high-resolution 3-D reconstruction of nervous tissue without the need for ultrathin physical sectioning.[4] The development of two-photon microscopy further increased imaging depths to several hundred micrometers and the use of adaptive optics has improved imaging depth even further.[5,6]

However, due to the opaqueness of nervous system tissue and the size of a mouse brain—several millimeters in all spatial dimensions—light microscopy remains limited for volumetric imaging at nanometer resolution through intact brain samples. A possible solution to this problem is to slice the brain into thin sections followed by confocal-, or 2P imaging.[7,8] However, detailed labeling and high-resolution connectivity reconstruction of thin sections is limited to small volumes and/or by the diffraction barrier of conventional light microscopes. Thus, an ideal integrative approach into this direction would be to selectively, fluorescently label individual structures within extended brain volumes and image these intact large brain samples at nanoscale resolution, that is, below the light microscope diffraction limit. A first promising step into this direction was the development of chemical tissue clearing approaches that largely eliminate light scattering (reviewed by Refs. 9–12). While some clearing methods rely on genetic labeling of cells, others also allow the accessibility of the native antigens to antibody and nucleic acid probes after the clearing process.[13,14] Yet, none of these methods achieved resolutions in the nanoscale range.

Recently, expansion microscopy, a radically new technique that virtually enhances the resolution of light microscopy by rather increasing the size of the tissue sample than equipment-wise, was introduced.[15–17] To bypass hardware limitations, the tissue is modified to utilize water adsorbent polymers to

---

*Address all correspondence to Martin K. Schwarz, E-mail: martin.schwarz@ukbonn.de; Ulrich Kubitscheck, E-mail: u.kubitscheck@uni-bonn.de

[†]These authors contributed equally to this research

physically expand enzymatically treated tissue samples in an isotropic manner. As a result of this expansion, fluorescent moieties spaced closer than the optical diffraction limit (≈250 nm) can be optically resolved resulting in effective super resolution images. Notably, the heavy adsorption of water during the expansion process renders the expanded tissue fully transparent. Thus, due to its transparency, expanded tissue represents an ideal object for light microscopic imaging at nanoscale resolution.[18] Still one caveat is now the large size of the expanded tissue sample.

Therefore, to image large neuronal populations at high speed and at high-resolution volumetric imaging methods are required. The approach of light-sheet fluorescence microscopy (LSFM) has emerged as a useful platform for meeting these goals and has already been used to image entire fluorescently labeled mouse brains at cellular resolution.[19–22] In LSFM, the sample is illuminated with a thin sheet of light and the emitted signal detected by an orthogonally arranged wide-field detection arm.[23,24] This setup allows for ultrafast imaging by simultaneous sampling of an entire optical plane that is visualized by a sensitive camera. LSFM features a gentle fluorophore excitation with very low photobleaching compared to other fluorescence microscopy techniques, such as wide-field or confocal microscopy, since excitation is confined to the detection plane.[25] This creates also an intrinsic optical sectioning. Image contrast is improved compared to techniques such as epi-illumination microscopy and can even further be amended by using a digitally scanned laser beam for illumination and a correspondingly moving line detection using rolling shutter readout by a scientific CMOS (sCMOS) camera, which produces a confocal line detection scheme.[20,26]

Volumetric data are acquired by moving the sample through a stationary light sheet. However, this light microscopic approach is fundamentally limited in resolution to about 250 nm laterally due to the diffraction barrier. Thus, only the combination of tissue expansion and light-sheet microscopy provides a methodological platform that allows high-speed light microscopic multicolor fluorescent imaging of large nervous tissue samples in super resolution. Here, we show the feasibility of this approach by imaging fluorescently labeled hippocampal neurons with neurites of the CA1 as well as the mouse dentate gyrus through all different layers at once and in super resolution. Moreover, we show data demonstrating two color labeling of pre- and postsynaptic proteins. We also identified GABAergic cells as postsynaptic targets of mossy fibers by identifying filopodial extensions of mossy terminals contacting GABAergic neurites.

Based on our results, we calculated that this approach would allow a nanoscale volumetric anatomical analysis of fluorescently and densely labeled neurons along the entire DG (≈1 mm^3) in 110 h with our current LSFM setup. Using an optimally tailored instrument, this time can be reduced to ∼5 h assuming an imaging frame rate of 40 Hz.

2 Results

In this study, we focused on a super resolution analysis of large GFP-labeled granule cells ensembles in mouse dorsal DG. Coronal DG sections were prepared for tissue expansion and LSFM analysis from a PROX1-cre mouse injected with rAAV-DIO-EGFP-WPRE to achieve selective expression of EGFP in DG granule cells. Details of the sample preparation are given in Sec. 4.

2.1 *Confocal Airyscan Imaging Is Not Practical for a Detailed Volumetric Reconstruction of Extended Fluorescently Labeled Connectivity Maps*

In a first approach, we explored the capabilities of state-of-the-art confocal laser scanning microscopy to obtain detailed high-resolution volumetric images of extended DG neuronal networks. For imaging EGFP-labeled DG granule cells (GC), we used a Zeiss LSM 880 with Airyscan detector, which is able to achieve a lateral full width at half maximum (FWHM) resolution of 120 nm under very optimal conditions.[27] Figure 1(a) shows a single high-resolution confocal plane of a 70-μm-thick coronal section through the dorsal DG, containing EGFP-labeled granule cells. The Airyscan-processed image was acquired using a water immersion (WI) objective lens with a numerical aperture (NA) of 1.2 and a pixel size of 50 nm. This image was generated from 5×8 individual tiles comprising 2048×2048 pixels each. Tiles were acquired with 10% overlap and stitched using the ZEN software (ZEN Black 2.3 SP1, Carl Zeiss Microscopy GmbH). The magnification demonstrates the excellent resolution of the Airyscan processed image, that allows to separate densely packed dendrites [Fig. 1(b)]. However, we encountered two principal limitations for extended volumetric neural network reconstructions performing these imaging experiments. First and most importantly, it is well known that image acquisition of confocal microscopes is inherently slow due to the sequential, pixelwise data acquisition. Thus, the total imaging duration of a single confocal plane with a resolution of 2048×2048 pixels/image covering a field of 102.4×102.4 μm^2 required about 10.1 s, when no averaging was performed. Acquisition of a complete image field of 742×452 μm^2, as shown in Fig. 1(a), required 400 s, since the tiles were acquired with 10% overlap for stitching. Thus, imaging of a 32-μm-thick volume with this field size using the optimal axial step size of 0.21 μm according to the Nyquist theorem required 1020 min or 17 h. Extrapolation of this data acquisition time to the total DG volume of 1 mm^3 yields a total duration of more than 1900 h. Moreover, *post-hoc* 3-D rendering of a $96 \times 165 \times 32$ μm^3 large region of interest (ROI) demonstrated that the achieved resolution was not sufficient to allow the unambiguous evaluation of

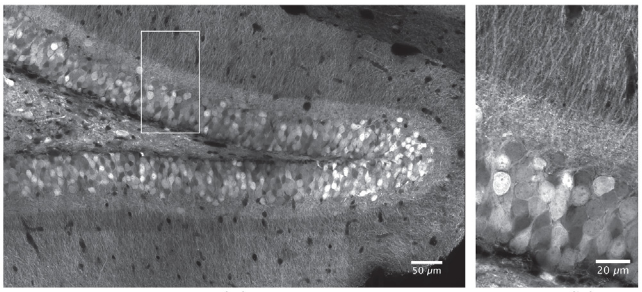

(a) (b)

Fig. 1 Coronal section of a dorsal mouse dentate gyrus containing EGFP-expressing granule cells imaged by high-resolution confocal microscopy. The endogenous EGFP fluorescence was enhanced by antibody staining against EGFP (see Sec. 4). (a) A single confocal plane acquired using an Airyscan detector and a 40× 1.2 NA WI imaging objective lens. The total field size in (a) was 742×452 μm^2, achieved by combining 8×5 single image stacks comprising 2048×2048 pixels in each frame. The individual tile stacks were acquired with 10% spatial overlap to enable efficient stitching using the algorithm described in Ref. 28. (b) Magnification of the ROI marked in Fig. 1(a).

the 3-D structure of the densely labeled granule cells due to melding together of individual neurites, although the image acquisition was done as carefully as possible. An additional increase of the applied laser intensity from 0.65 to 1 $\mathrm{kW/cm^2}$ improved the signal-to-noise ratio but not the effective resolution. In addition, the higher laser intensity caused notable bleaching of the sample during confocal image acquisition (see Sec. 4).

In conclusion, we here used the latest high-resolution confocal laser scanning instrument with Airyscan detector and were able to laterally resolve neuronal structures as small as 160 nm (FWHM, see Sec. 4). The achieved axial resolution was 810 nm.

2.2 *Light-Sheet Fluorescence Expansion Microscopy for Volumetric Imaging*

LSFM is known for its high-speed imaging requiring only low irradiances.[29] Unfortunately, volumetric imaging of mouse brain tissue by LSFM is complicated since it requires transparent specimens due to the necessity to illuminate the object from the side with a thin sheet of light to generate the optical sections. To overcome this problem and to increase the effective resolution, we decided to expand the mouse brain sections before light sheet imaging to achieve virtual optical super resolution in large tissue volumes at an imaging speed outperforming the currently fastest point scanning devices. Note that expansion of tissue has the great advantage that the heavy adsorption of water renders the samples completely transparent.

Expansion of a 70-μm-thick anti-EGFP-labeled mouse brain slice from a PROX1-cre mouse, injected with rAAV-DIO-EGFP-WPRE to achieve selective expression of EGFP in DG granule cells was performed according to Ref. 16. The refractive index of the sample gel matched almost that of pure water and the expanded samples became completely transparent, excellently suited for LSFM using WI detection objectives.[15,17] Sample expansion was isotropic[15] and enlarged our DG sample by a factor of 3.9 (see Sec. 4). We employed a custom-built LSFM to image respective samples of expanded DG sections. A 25× objective lens with a NA of 1.1 was used together with a 1.5× magnification lens and yielded a field of view of $355 \times 355\ \mu\mathrm{m}^2$. Thus, images of expanded DG samples had to be acquired in a mosaic fashion. For each mosaic tile, a z-stack of 300 images with a $\Delta z = 1\ \mu\mathrm{m}$ was acquired with a frame rate of 1.8 Hz. After imaging, the tile stacks were contrast-adjusted and stitched yielding views of the dorsal DG sections of unprecedented resolution (Fig. 2). Figure 2(a) shows a single LSFM plane of the stitched volume at a depth of 151 μm. The field size was $3600 \times 1240\ \mu\mathrm{m}^2$ after expansion corresponding to a size of about $920 \times 320\ \mu\mathrm{m}^2$ before expansion considering the magnification factor of 3.9 ± 0.3 (see Sec. 4). Figure 2(b) shows the magnification of the ROI marked in Fig. 2(a), and the possibility to detect individual spines demonstrates the remarkable resolution of the image. Note, that only small segments of the dendrites are visible in this single optical section. However, a maximum projection of the complete region that was imaged revealed the 3-D outline of entire dendritic fields [Fig. 2(c)]. The high virtual resolution of 100 nm laterally and 415 nm axially (see Sec. 4) and the superb contrast allowed to trace and segment the dendritic trees of three individual granule cells revealing their detailed morphoanatomical shape [Fig. 2(d)]. Thus, we achieved a lateral resolution about twofold lower than STED microscopy (25 to 80 nm),[30] but clearly better than structured illumination microscopy (130 to 160 nm)[30,31] or high-resolution confocal microscopy (>120 nm,[27]) using an Airyscan detector. Our axial resolution was lower than achievable by STED and structured illumination microscopy (150 to 600 nm and 250 nm, respectively[30]), but higher than for high-resolution confocal microscopy (>550 nm,[27,30] and Sec. 4).

Note that a sample volume of 1 mm^3 would be transformed by expansion to a volume of ($3.9 \times 3.9 \times 3.9\ \mathrm{mm}^3$). The step size of imaging should be 0.8 μm in order to fulfill the Nyquist criterion, since the FWHM of our axial resolution was 1.62 μm (see Sec. 4). This yields a total number of 5000 sections. The lateral extension of such a sample requires the use of 12×12 tiles each having a field of view of 355 μm. Thus, a total number of 720.000 images will cover the complete volume, what would require 111 h for imaging at a rate of 1.8 Hz. Thus, light-sheet fluorescence expansion microscopy (LSFEM) imaging of a complete dentate gyrus is faster by a factor of 17 compared to Airyscan confocal microscopy.

Figure 1, which was acquired by Airyscan confocal laser scanning microscopy, showed a brain region of similar spatial extension before tissue expansion. Visual comparison between Figs. 1 and 2 readily reveals the gain in contrast and axial resolution achieved by light-sheet expansion microscopy. This was demonstrated by plotting line profiles of the dense neurite region of Figs. 1(b) and 2(b) (Fig. 3). The figure demonstrates the lower number of dendrites containing in an optical slice of the LSFEM with its effective thickness of 415 nm compared to the optical slice of the Airyscan image with its axial extension of 810 nm.

2.3 *Sparsely Labeled Expanded Mouse Brain Slices*

GC in brain slices of dorsal DG display an extremely narrow arrangement of cell bodies and neurites, as can be seen in Figs. 1 and 2. Individual neurites may optically be resolved, yet, tracing them over their entire spatial extension is possible only in rare cases. This is due to the fact that entire neurons are unlikely to be entirely contained within a single tissue section and, although we achieve effective super resolution, melding together of closely together lying individual structures can virtually not be avoided in densely packed structures. One solution to this problem is using a more "sparse labeling" approach. To this end, we infected the hippocampal CA1 region of wt mice with a rAAV-expressing EGFP under control of the human synapsin1 promoter by stereotaxic virus injection and stained afterward with an antibody against EGFP (for details, see Sec. 4). The use of low virus titers (10E8/ml) resulted in a stochastic and relatively sparse labeling of CA1 pyramidal neurons. This experimental approach allowed us to unequivocally identify individual dendritic networks and follow them over 1.3 mm in this experiment [Fig. 4(a) and Video 3]. Note that the image stack shown in Fig. 4 was obtained using an axial step size of only 0.3 μm revealing even the tiniest dendritic structures in nanoscale resolution. E.g., individual dendritic spines can be visualized in the high-resolution images [Figs. 4(b)–4(d) and Video 4]. Figure 4(e) demonstrates that even spine necks can be recognized.

Notably, these images were acquired using a 25× NA1.1 objective lens combined with a 1.5× magnification, which achieved a theoretical FWHM lateral optical resolution of 310 nm and a nominal FWHM axial resolution of 1010 nm at the emission maximum of the used dye, ATTO647N (664 nm). The expansion process magnified all labeled object structures by a factor of 3.9, thus transforming these values

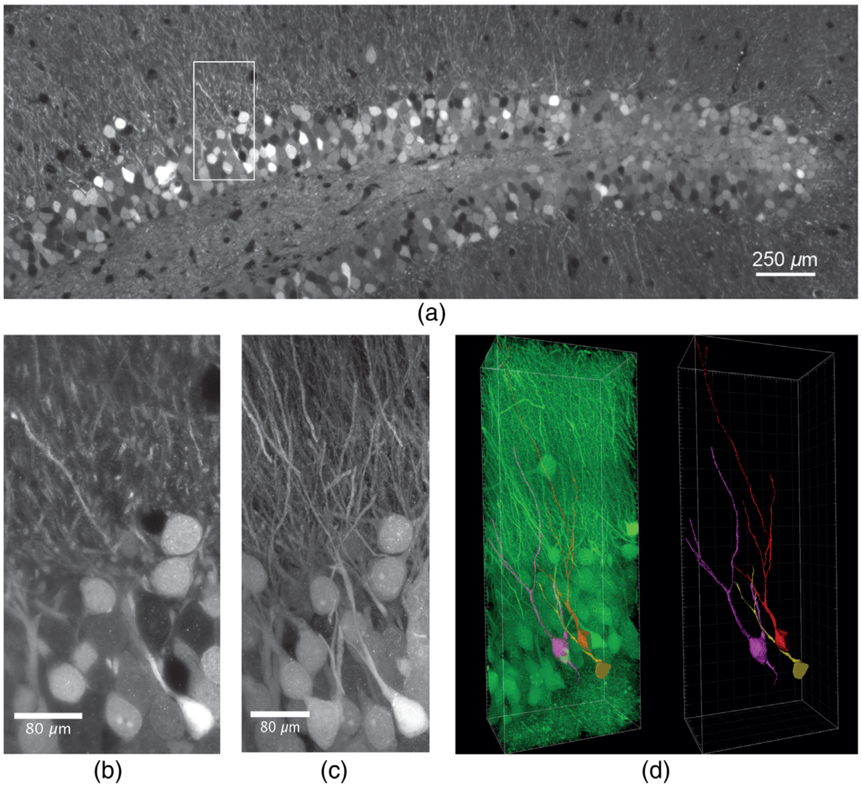

Fig. 2 Expanded, antibody-stained mouse brain slice imaged by LSFM. The sample was expanded and imaged with a custom-built light-sheet microscope. In total 70 z-stacks with a step size of 1 μm, covering a depth of 275 μm with 30% overlap were stitched to generate the image. (a) Single plane of the stitched volume at a depth of 65 μm. The total volume shown after expansion was $3600 \times 1240 \times 275\ \mu\text{m}^3$ (Video 1, MP4, 32 MB [URL: https://doi.org/10.1117/1.NPh.6.1.015005.1]). (b) Magnification of the region marked in (a), lateral field size $254 \times 492\ \mu\text{m}^2$. (c) Maximum projection of the selected region marked in (a) comprising 76 slices of the stack, lateral field size $254 \times 492\ \mu\text{m}^2$. Single granule cells and dendrites can well be distinguished and separated. The stack was median-filtered to remove staining artifacts before the maximum projection. (d) Segmentation and tracing of the neurites of three selected granule cells (Video 2, MP4, 19 MB [URL: https://doi.org/10.1117/1.NPh.6.1.015005.2]). Left panel: segmented GCs in the neuronal network, right panel: segmented GCs with traced neurites.

into an expected virtual lateral and axial resolution of ≈80 and 260 nm, respectively. Experimentally, we did not reach the theoretical expectation, but rather determined values of 135 and 590 nm for the FWHM values of the lateral and axial virtual optical resolution, respectively (see Sec. 4). Presumably, this discrepancy was partly due to the fact that a dipping objective was used for imaging because it featured a high NA and a long working distance. It contained a correction collar for adjusting it also for the use with a cover slip and was employed in this way. We suspect, however, that in this configuration the objective did not deliver its full performance. Hence, we assume that it is optimal for imaging expanded samples using long working distance dipping objective lenses in an upright optical detection path.

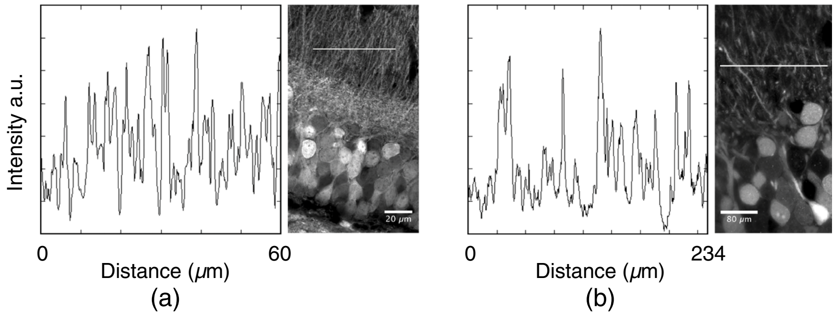

Fig. 3 Contrast in Airyscan and LSFM microscopy images. (a) Line profile determined in a 0.3-μm-wide line with a length of 60 μm. The right panel shows the position of the line in Fig. 1(b). (b) Line profile determined in a $3.9 \times 0.3\ \mu$m wide line with a length of $3.9 \times 60\ \mu$m. The right panel shows the position of the line in Fig. 2(b).

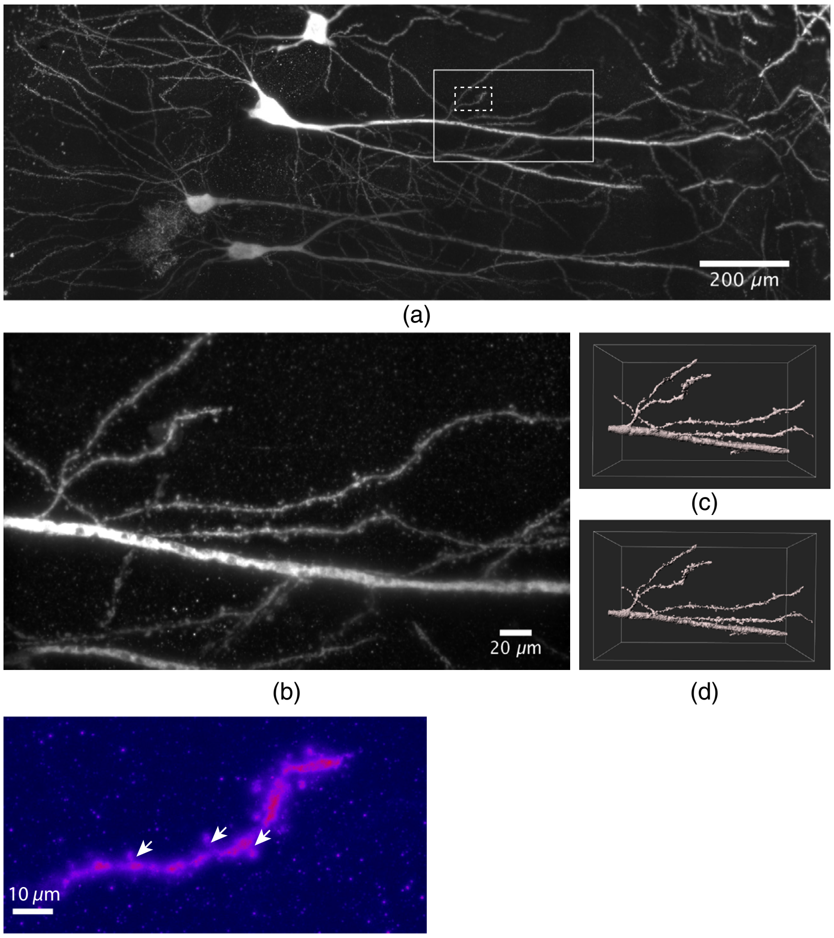

Fig. 4 Dendritic segments of sparsely labeled pyramidal neurons in CA1. (a) Maximum projection of a total of 24 stacks with an axial step size of 0.3 μm covering a depth of 450 μm were acquired and stitched together (Video 3, MP4, 39 MB [URL: https://doi.org/10.1117/1.NPh.6.1.015005.3]). The sparse labeling and small axial imaging step size allowed to reconstruct the labeled granule cells and dendrites over distances of 1.3 mm after expansion. (b) Magnification of the large ROI marked in (a). The high virtual optical resolution allowed to identify finest detail, e.g., the morphology of individual synaptic spines. (c) 3-D surface rendering of a region of the data shown in (b), the dimensions were $256 \times 152 \times 205\ \mu m^3$. (d) Deconvolution of the image data using the experimental PSF yielded a significant increase in data quality (Video 4, MP4, 4 MB [URL: https://doi.org/10.1117/1.NPh.6.1.015005.4]). (e) A maximum projection of 250 frames of a magnified region of the image stack shown in (a) (see dashed ROI) containing a single dendrite demonstrates that even dendritic spine necks (arrows) can be recognized.

2.4 *Multicolor Imaging of Sparsely Labeled DG Neurons After Tissue Expansion*

In order to show the possibility of neural connectivity mapping, we performed experiments demonstrating multicolor labeling of pre- and postsynaptic proteins. Briefly, we labeled virus-infected EGFP-positive pyramidal neurons with antibodies against EGFP to outline neurite morphology and subsequently stained for the postsynaptic protein shank2 (Alexa568, green) and the presynaptic protein Bassoon (Alexa 647, red). Figure 5(a) shows a region with an axial extension of 390 μm, which was imaged using 1300 sections. Figure 5(b) shows a magnification of the ROI marked in (a) as maximum projection of 13 images extending over a distance of 3.6 μm. Figure 5(c) shows a contrast-enhanced magnification of a region marked in (b) by a white arrow with a lateral field size of $17.3 \times 17.3\ \mu m^2$, indicating synaptic connectivity. Figure 5(d) shows a 3-D surface rendering of the synapse region shown in (c) to demonstrate the spatial arrangement of the fluorescent labels within the context of the synapse. Using the image data shown in Fig. 5, we measured the distances between 10 shank2-bassoon pairs [see Fig. 5(d)]. The maximum intensity projection of those regions was used from 10 to 15 planes. The intensity profiles—obtained by drawing a line perpendicular to the synapse surface—were fitted by Gaussian functions to determine the respective maximum positions of the label distribution. This yielded the expected distance of 160 ± 50 nm between pre- and postsynaptic proteins. Altogether, Fig. 5 demonstrates the capability of our approach to visualize details of synaptic connectivity, which is a prerequisite for systematic connectivity analysis.

In addition, we generated DG samples containing sparsely expressing EGFP-positive GCs in order to visualize the mossy fibers within hilus of the DG. We then performed

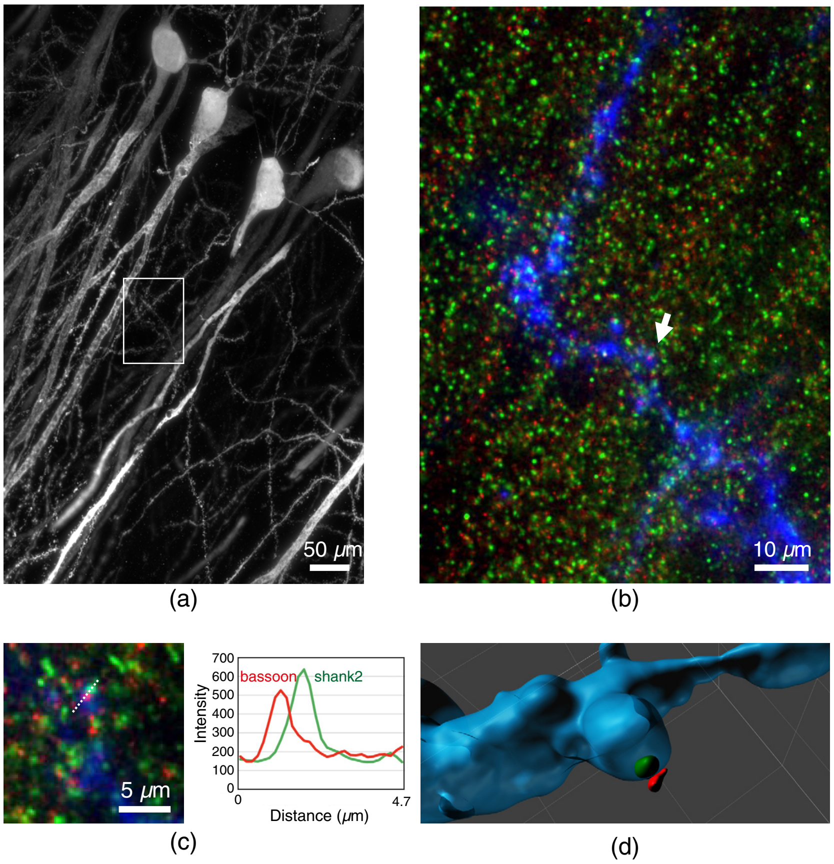

(a) (b) (c) (d)

Fig. 5 Multicolor imaging of sparsely labeled pyramidal neurons in CA1 imaged by LSFEM. (a) Maximum intensity projection of an expanded mouse brain slice expressing EGFP. The endogenous EGFP fluorescence was enhanced by antibody staining against EGFP, the secondary antibody was conjugated to Alexa 488. The total axial extension was 390 μm. (b) Magnification of the ROI marked in (a). Dendrites were stained with Alexa488 (blue), postsynaptic proteins (shank2) stained with Alexa568 (green), presynaptic proteins (bassoon) stained with Alexa647 (red). The shown images were deconvolved. (c) Magnification a region indicated in (b) (white arrow), lateral field size 17.3×17.3 μm^2, indicating synaptic connectivity. The right panel in (c) shows the intensity profiles along the dotted line. (d) 3-D surface rendering of the synapse region shown in (c).

antibody stainings against parvalbumin on these EGFP-positive, anti-EGFP stained sections to selectively label hilar GABAergic interneurons in red (Alexa 568). We then performed two-color LSFEM volumetric imaging and used differential color surface rendering to identify GABAergic cells as postsynaptic targets of mossy fibers boutons. Figures 6(a) and 6(b) show an overview of the DG hilus with EGFP-positive mossy fibers in green and parvalbumin-positive GABAergic interneurons in red. Figure 6(c) shows a zoom identifying filopodia on mossy fiber boutons that contact dendrites of GABAergic hilar interneurons. Collectively, we present evidence that the spatial resolution using LSFEM is sufficient to study neuronal connectivity within the context of large neuronal ensembles.

For performing the differential color surface rendering, the volume was deconvolved using Huygens with the corresponding measured PSF for each channel. The deconvolved image data were loaded into Imaris to perform a 3-D rendering of the volume of interest, $171.4 \times 343.2 \times 253.5$ μm^3 for the GABAeric cells and $71 \times 57 \times 147$ μm^3 for the mossy fibers boutons. The connectivity area shown in Fig. 6 was obtained using the surface tool over both channels choosing a surface grain size of 0.346 μm and a manually defined intensity threshold.

3 Discussion

Wide scale volumetric analysis of the topology of neuronal circuits requires a fast and high-resolution nanoscale imaging approach. Here, we developed and explored LSFEM by combining expansion microscopy and LSFM to achieve this goal.

The idea of tissue expansion combined with conventional light microscopy was initially introduced by Chen et al. in 2015[15] and termed expansion microscopy. Using this technique, nanoscale imaging of microtubuli in cultured cells as well as of Bassoon and Homer1 in a Thy1-YFP mouse brain using conventional confocal microscopy was demonstrated.

The initial approach was based on the use of trifunctional labels comprising a linker to the hygroscopic gel, a fluorophore for visualization, and an oligonucleotide that was hybridized to a complementary sequence attached to a secondary antibody. This rather complicated approach was simplified by Chozinski et al. who developed a strategy to perform expansion microscopy using conventional immunostaining,[16] thus circumventing the complicated labeling procedure using custom synthetized trifunctional dyes. They demonstrated nanoscale fluorescence imaging of a THY1- YFP-H mouse brain slice immunostained for YFP, the presynaptic marker protein Bassoon, and the

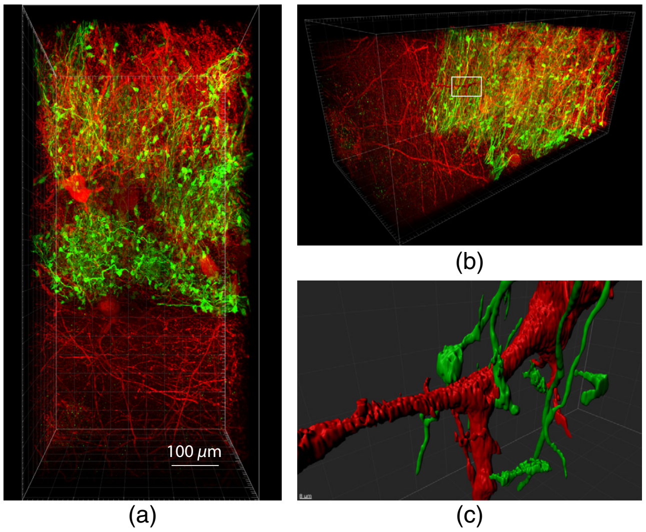

(a) (b) (c)

Fig. 6 Two-color imaging of mossy fibers and GABAergic interneurons in DG. (a) Mossy fibers in the hilus area expressing EGFP. The endogenous EGFP fluorescence was enhanced by antibody staining against EGFP, the secondary antibody was conjugated to Alexa 488 (green). Parvalbumin staining identified GABAergic interneurons shown in red (Video 5, MP4, 65 MB [URL: https://doi.org/10.1117/1.NPh.6.1.015005.5]). 1500 optical slices were acquired with a step size of 0.3 μm, the shown data were deconvolved. Volume size $456 \times 945 \times 390\ \mu\text{m}^3$. (b) Side view of the data shown in (a). (c) Segmented parvalbumin cells and mossy fibers reconstructed in 3-D. Magnification of the ROI marked in (b), showing connection between the cells.

postsynaptic marker Homer1. Further methodological developments demonstrated that expansion could also be performed on samples containing genetically encoded fluorescent proteins, that partly retained their fluorescence after the expansion procedure.[32] This was an important step toward large-volume imaging, since it overcomes the necessity of antibody stainings, that are usually limited by penetration constraints of brain tissue.

Finally, Chang et al. introduced iterative expansion microscopy, which was principally a sequential creation of two different expandable polymer gels, one within the mesh of the other.[17] This approach yielded linear expansion factors of about 20, allowing to image the structural details of dendritic spines.

In recent years, LSFM became a standard method for the analysis of large and extended biological specimen, e.g., fluorescently labeled mouse brains.[33] For fixed specimen, one of the requirements was that the tissue was optically cleared before imaging. Meanwhile, over 10 different clearing agents are in use (for review, see Refs. 9, 11, and 34). While a suitable and effective clearing method was essential for LSFM in the case of non-expanded samples to achieve the required transparency, this aspect became irrelevant when combining it with expansion to LSFEM, because expanded samples were intrinsically transparent due to their high water content.

The LSFEM pipeline introduced here allows to rapidly obtain super-resolved neuronal connectivity maps using a diffraction-limited light-sheet microscope. As a proof of principle, we imaged and reconstructed large and densely fluorescently labeled subregions of the mouse hippocampal DG and CA1 regions. Notably, in the densely packed granule cell layer (gcl) of the dorsal hippocampus, we could image and segment individual granule cells together with their neurites extending deep into the molecular layer in super-resolution revealing their fine structural details.

Note that the imaging resolution was high enough to visualize individual dendritic spines. Moreover, we could also show data demonstrating two color labeling of pre- and postsynaptic proteins and identified GABAergic cells as postsynaptic targets of mossy fibers by visualizing filopodial extensions of mossy terminals contacting GABAergic neurites. The implementation of multicolor staining is especially important in the case of neural network reconstructions that partly rely on the possibility to image the tight association between pre- and postsynaptic specializations. As shown synaptic contacts can be identified by proximity measurements of the pre- to the postsynapse, which affords differential labeling of both structures for reliable connectivity predictions.

A comparison between high-resolution confocal laser scanning microscopy using an Airyscan detector (HR-CLSM) and LSFEM suggests that HR-CLSM is not as practical for volumetric connectivity analysis as our LSFEM approach with regard to the achievable optical resolution and the imaging speed (see Figs. 1 and 2). While high-resolution (high NA) CLSM objectives are superior to the objective used in our LSFM device, these objectives are not optimal to acquire large 3-D scans of the type we are performing to study neuronal connectivity maps. This is because of the relatively short working distance as well as the relatively low imaging speed, and also the relatively high bleaching rates of classical point scanning devices. The high imaging speed is especially beneficial for expanded tissue samples, since it minimizes bleaching of the fluorophores. We could show that imaging of a mosaic tile of $100 \times 100 \times 10\ \mu\text{m}^3$ by Airyscan imaging using a state-of-the-art CLSM required about 480 s, when optimal lateral and axial resolution should be achieved, whereas imaging the same object field (multiplied by the expansion factor 3.9) by LSFEM required only about 30 s.

Extended samples must be imaged in a mosaic-tile fashion and subsequently stitched together. The stitching of the stacks is performed using published algorithms and reconstructed the complete dorsal dentate gyrus of a mouse contained on a 70-μm-thick coronal section out of 70 stacks. Mosaic imaging allowed the use of high NA detection objectives to achieve an optimal optical resolution. The magnification of the objective and the size of the camera chip led to a resolution that well satisfied the Nyquist theorem. Hence, biological details in the order of 100 nm before expansion could well be resolved, which correlates with the length scales necessary for neuronal connectivity mapping.

We would also like to point out that a fair comparison of scanning speed/resolution by CLSM on expanded samples over a large volume is not practical, since the limited working distance and the high rate of bleaching (of the point scanning device) does not allow elaborate volumetric scans to be made.

It is important to mention that sample preparation needs to be done carefully. Especially mounting of the expanded sample requires care since the expanded sample is quite unstable. To avoid destruction of the sample during mounting, we developed a dedicated sample chamber, into which the cover slip with the sample could directly be inserted. Since imaging large volumes at super resolution takes a considerable amount of time, even when using LSFEM important parameters for accurate circuit reconstruction are sample drift and residual probe swelling. Concerning sample drift our instrument was designed for optimum stability and displayed a drift of about 10 nm/h only. However, the positional precision was limited by the motors, which were used to move the sample during image acquisition. The motors displayed a unidirectional repeatability of 100 nm. Yet, any lateral sample drift or movement was of no concern for circuit reconstruction, since it was a requirement to stitch the various image stacks (see Sec. 4). The stitching process corrected for any possible sample movement. Concerning a potential residual swelling of the sample after the expansion process, we did not observe any further swelling when it was prepared according to our given protocol. A size change of the samples was in the order of magnitude of the measurement precision as determined by repeated imaging of fluorescent beads embedded within the expanded gel.

Another important aspect of LSFEM analysis of large volumes is the amount of raw data that is generated. Although the amount of data produced is relatively large (raw data for the image shown in Fig. 2 was 100 GB), it still can be handled with desktop computers equipped with fast graphic cards and sufficient memory (see Sec. 4). The amount of data generated is depending on the volume and the density of labeled neurons. The produced data are in the terabyte range. An issue still remaining is, however, how to compare and analyze connectivity matrices of large brain regions imaged in super resolution. This will likely require new mathematical algorithms for graph analysis as well as statistical tests to compare different neural circuits with each other and to identify anatomical connectivity motifs.

Finally, we would like to stress here that a decisive factor in imaging extended neural networks by expansion light-sheet microscopy is imaging duration. Thus, we are currently optimizing our setup and expect to increase the imaging rate by a factor of 10 to 20. Such a device would allow nanoscale imaging of our specimen (3.9^3 mm^3) in about 10 h. Also, we believe that the use of an appropriately designed lattice light-sheet microscope would allow to further increase the achievable resolution, especially when used in its structured illumination mode.[35]

4 Material and Methods

4.1 *Mice*

Mice were maintained on a 12-h light/12-h dark cycle with food and water always available. All the experiments were carried out in accordance with the German animal protection law (TierSCHG), FELASA and were approved by the animal welfare committee of the University of Bonn.

C57BL/6 mice were purchased from Charles River (Sulzfeld, Germany). The Prox-1 cre line[36] is maintained in the local animal facility (Haus für Experimentelle Therapie).

4.2 *Virus Injection*

Viral injections were performed under aseptic conditions in *Prox1::cre* or C57BL/6 mice up to 10 months old. The mice were anesthetized with a mixture of Fentanyl (Rotexmedica, Germany), Midazolam (Rotexmedica, Germany), and Domitor (Orion Pharma, Finland) via intraperitoneal injection (0.05/5.0/0.5 mg/kg). Analgesia (0.05 mg/kg of buprenorphine; Buprenovet, Bayer, Germany) was administered intraperitoneally prior to the injection, and Xylocain (AstraZeneca, Germany) was used for local anesthesia. Stereotaxic injections were performed using an injection frame (WPI Benchmark/Kopf) and a microprocessor-controlled minipump (World Precision Instruments, Sarasota, Florida), 1000 nl of the viral solution was injected bilaterally into the hippocampus (rAAV-DIO-eGFP; rAAV-syn-GFP; coordinates: rostrocaudal: −2.1 mm from the Bregma; mediolateral: ±1.2 mm from the midline; dorsoventral: −2.1 mm). After the injection, the scalp was sutured with PERMA-HAND Silk Suture (Ethicon), and an antibacterial ointment (Refobacin®, Almirall, Germany) was applied, followed by the intraperitoneal injection of a mixture of Naloxon (B. Braun, Germany), Flumazenil (B. Braun, Germany), and Antisedan (Orion Pharma, Finland) (1.2/0.5/2.5 mg/kg). To prevent the wound pain, analgesia was administered on the 3 following days.

4.3 *Perfusion and Slicing*

Three weeks after the injection, the mice were anesthetized with a mixture of xylazine (10 mg/kg; Bayer Vital, Germany) and ketamine (100 mg/kg; bela-pharm GmbH & Co. KG, Germany). Using a peristaltic pump (Laborschlauchpumpe PLP33, Mercateo, Germany), the mice were perfused transcardially with 1× PBS followed by 4% paraformaldehyde (PFA) in 1 × PBS. All solutions were stored on ice prior to the perfusion. Brains were removed from the skull and post-fixed in 4% paraformaldehyde overnight (ON) at +4°C. After fixation, the brains were moved into PBS containing 0.01% sodium azide and stored at +4°C.

4.4 *Immunochemistry*

Immunohistochemistry was performed according to standard protocols. Briefly, the fixed brains were sectioned coronally (70 or 100 μm) using a vibratome (Leica VT1000 S). To prevent unspecific binding of the primary antibody, the sections were incubated in blocking buffer (1× PBS containing 0.1% TritonX-100 and 5% normal goat serum) on a shaker for 6 h at room temperature. After blocking, the sections were incubated ON in primary antibody (chicken anti-GFP; 1:5000 in blocking buffer; Abcam, ab13970; rabbit anti-parvalbumin diluted 1:1000 in blocking buffer, Swant, PV27) at +4°C. The following day, slices were washed at room temperature in blocking buffer three times for 20 min and incubated ON in Alexa Fluor® 488-conjugated goat antibody against chicken IgY, or Alexa Fluor® 568 goat anti-rabbit (1:400 in blocking buffer; Life Technologies, A-11039, A-11011) at +4°C.

4.5 *Labeling of Pre- and Postsynaptic Proteins*

For pre- and postsynaptic labeling sections were stained against presynaptic active zone protein bassoon (primary antibody mouse anti-bassoon diluted 1:200 in blocking buffer, Enzo Life Sciences, SAP7F407; secondary antibody goat anti-mouse conjugated with biotin diluted 1:200 in blocking buffer, Jackson ImmunoResearch, 115-067-003 followed by Alexa Fluor® 647 Streptavidin, Jackson ImmunoResearch, 016-600-084) and postsynaptic scaffold protein Shank2 (primary antibody guinea pig anti-Shank2 diluted 1:200 in blocking buffer, Synaptic Systems, 162 204; secondary antibody goat anti-guinea pig conjugated with Alexa Fluor® 568 diluted 1:200 in blocking buffer, Life Technologies, A-11075).

4.6 *Gelation and Expansion*

The expansion microscopy protocol was adopted from Refs. 15 and 16. The immunostained sections were incubated with 1 mM methylacrylic acid-NHS (Sigma Aldrich) linker for 1 h. After washing three times in PBS, the sections were incubated for 45 min in the monomer solution (8.6% sodium acrylate, 2.5% acrylamide, 0.15% N,N'- methylenebisacrylamide, and 11.7% NaCl in 1× PBS), followed by 2 h incubation at 37°C in a gelling solution. The gelling solution was prepared by adding 4-hydroxy-TEMPO (0.01%), TEMED (0.2%) and ammonium persulfate (0.2%) to the monomer solution. After the gel formation, the samples were incubated at 37°C ON in the digestion buffer (50 mM Tris, 1 mM EDTA, 0.5% Triton-X100, 0.8M guanidine HCl, and 16 U/ml of proteinase K; pH 8.0). The next day, the digestion buffer was removed and the sections were washed with deionized water for 2.5 h. Subsequently, the samples were stored in deionized water at +4°C until imaging. For microscopic examination, the expanded gel sample was fixed on the bottom coverslip of the imaging chamber with poly-L-lysine to avoid movements during the measurement and the chamber was filled with deionized water.

4.7 *Light Microscopy*

For light-sheet microscopy, we used a custom-built setup based on a Nikon Eclipse Ti-U inverted microscope (Nikon, Düsseldorf, Germany). A previous version of this instrument was described by Ref. 26. Scanned illumination and sample stage were custom-designed, whereas the Eclipse Ti-U provided the detection path. For fluorescence excitation, three fiber-coupled lasers emitting at 488, 638 (Obis LS, Coherent, Santa Clara), and 532 nm (LasNova Green 50 Series, Lasos, Jena, Germany) were employed. Laser light was regulated by an acousto-optical tunable filter (AOTF, TF-525-250-6-3-GH18A, Gooch&Housego, Ilminster). The horizontally scanned light sheet was generated by a galvanometer system with silver-coated mirrors. The adjustment of the beam waist position within the sample chamber was realized by a relay optics mounted on a linear precision stage. The beam waist in the object plane was adjusted to a $1/e^2$ diameter of $7.9 \pm 0.02\ \mu$m for the 488 nm, $8.3 \pm 0.02\ \mu$m for the 532 nm, and $9.5 \pm 0.02\ \mu$m for the 638-nm laser lines. The irradiance at the sample plane amounted to 240, 340, and 380 $\mathrm{W/cm^2}$ at 488, 532, and 638 nm, respectively. Our custom-designed sample chamber featured an illumination window with coverslip thickness (0.17 mm) and a bottom glass coverslip for light detection. The sample chamber could be moved in three spatial directions by motorized microtranslation stages. For illumination we used a Mitutoyo 10× NA 0.28 air objective. The detection objective was a 25× NA 1.1 WI objective with cover slip correction (Nikon). The Eclipse Ti-U had a built-in optional 1.5× magnification, which was employed as indicated. We used a sCMOS camera (2048 × 2048 pixels, pixel size 6.5 μm, Orca Flash 4.0 V2, Hamamatsu Photonics K.K., Hamamatsu City, Japan) for data acquisition in rolling shutter mode. The object field pixel size was $(173\ \mathrm{nm})^2$ corresponding to a field of view of $(355\ \mu\mathrm{m})^2$. All electronic components were controlled by a custom-written LabView program.

The sample was mounted in a custom built sample chamber. The excitation laser beam entered the chamber through the window at the left-hand side, which was formed by a conventional 24 × 24 mm coverslip with 0.17 mm thickness glued to the outer chamber wall. The sample was mounted on a coverslip, which was slid into the interstice in the chamber walls from the front. Eventually, the chamber was closed by a third coverslip at the front side and filled with deionized water. For the waterproofing of the chamber, the slits between the coverslips and the chamber walls were sealed with 2% agarose. The chamber was mounted on a three-axis motor.

The image acquisition speed of our instrument was not optimized for high speed, since it was an experimental system. Image acquisition time depended on the line exposure time and the slit width of the rolling shutter, respectively, the waiting time before line activation. For a typical exposure time of 20 ms per line and a confocal slit width of 256 pixels, we reached a total exposure time of 180 ms for one frame. Due to various signal processing tasks of the instrument, the total time required to acquire one frame amounted in summary to about 500 ms. Altogether, the acquisition time for a stack of 400 frames amounted to 222.7 s corresponding to a frame rate of 1.8 Hz. Acquisition of a complete stack comprising 1500 images using a step size of 0.3 μm at the irradiance of 240 $\mathrm{mW/cm^2}$ resulted in a bleaching of 2% in a central image.

The sample size greatly exceeded the lateral object field size of $(355\ \mu\mathrm{m})^2$. Therefore, the data were acquired in a mosaic-like fashion. To this end, we acquired N image tiles in the direction perpendicular to the laser beam (y direction). The propagation direction of the laser beam corresponded to the x direction. This ensured that the focus of the beam remained always in the center of the field of view. To enable a subsequent stitching of the tiles, two neighboring tiles had 30% spatial overlap. When the border of the sample was reached, the sample chamber was shifted along the optical axis to start the acquisition of the next N stacks, but displaced along the optical axis. Due to the air/water interface in the illumination beam path, the laser focus shifted along the optical axis when the sample chamber was moved in x direction, and it had to be readjusted prior to image acquisition. So far, this readjustment was done manually. To obtain a mosaic of $N \times M$ stacks, the laser focus had to be adjusted M times. The total acquisition time for a mosaic comprising 16 × 5 stacks with 300 images per stack was 5 h. This mosaic covered a volume of $3.6 \times 1.3 \times 0.3\ \mathrm{mm}^3$.

High-resolution confocal microscopy was performed using a Zeiss LSM 880 equipped with Airyscan detector. Images were acquired using a 40× WI objective lens with NA 1.2 according to standard protocols. For Airyscan imaging, a laser power of 0.65 $\mathrm{kW/cm^2}$ was used routinely (0.3% of the available power). After imaging of a complete stack comprising 160 images, the topmost frame was bleached by 25%.

4.8 *Characterization of Optical Resolution*

The lateral resolution theoretically achievable with an objective lens is given by the Rayleigh criterion, d_R, which quantifies the distance between the maximum and first minimum of the point spread function (PSF):

$$d_R = \frac{0.61\lambda}{NA}$$

Here, λ denotes the wavelength of the detected light and NA is the numerical aperture of the objective. Experimentally, this value is difficult to determine. Commonly the full width at half maximum (FWHM_{xy},) is used instead, which is related to d_R as

$$\mathrm{FWHM}_{xy} = 0.84 \cdot d_R.$$

Similarly, the axial detection resolution d_z is given as

$$d_z = \frac{2\lambda n}{NA^2},$$

where n denotes the refractive index of the medium. The value d_z can be related to the FWHM along axial direction, FWHM_z, as

$$\mathrm{FWHM}_z = 0.88 \cdot d_z.$$

The axial width of the LSFM PSF is given by the product of the excitation and detection probability distributions.

In order to measure the resolution realizable with our LSFEM setup, we used fluorescent beads with subresolution diameters and the PSF extraction feature of the deconvolution software Huygens (Scientific Volume Imaging, Hilversum, The Netherlands).

We prepared samples of green and red fluorescent beads with diameters of 100 and 176 nm in 1% agarose gels, respectively. We acquired z-stacks of these samples with both the Airyscan confocal microscope and the light-sheet microscope and determined the PSF using Huygens (Table 1). From the lateral and axial intensity profiles of the PSFs, we derived the respective FWHM values as follows:

Note that the PSF was measured using a lateral object field pixel size of 173 nm. We are restricted to this value, because it is determined by the objective magnification (25×), the supplemental magnification lens (1.5×) and the camera pixel size (6.5 μm). Simulating the imaging of subresolution objects with this pixel size shows that this slight violation of the Nyquist theorem leads to an underestimation of the resolution by 15% to 20%.

For comparison, we also determined the PSF of the Airyscan LSM 880 using a 63× oil immersion objective with NA 1.4. Here, we obtained FWHM values for the PSF of 135 and 515 nm laterally and axially, respectively.

Table 1 Optical resolutions of the utilized microscopes.

	Theoretical FWHM resolution (nm)[a]		Experimental FWHM resolution (nm)[b]		Experimental virtual FWHM resolution (nm)[c]	
LSM/ excitation	Lateral	Axial	Lateral	Axial	Lateral	Axial
Airyscan 488 nm	—	—	160	810	—	—
LSFM 488 nm	242	790	380	1625	100	415
LSFM 640 nm	310	1010	520	2300	135	590

[a] The theoretical FWHM values were determined using the procedures given above and emission wavelengths of 520 and 665 nm for green and red excitation, respectively.

[b] All values have errors of maximally 5%.

[c] The virtual resolution was calculated taking the average expansion factor of 3.9 into account.

4.9 *Image Processing*

3-D stacks of raw 16-bit images were processed using custom-written MATLAB scripts, which allowed parallel data processing. In a first step, the intensity histograms were adjusted to homogenize brightness and contrast throughout the complete data set. Every 3-D stack was first scanned to find its minimum and maximum intensity values. With the respective values, a linear intensity adjustment was performed to cover the full dynamic range.

To achieve complete representations of the mouse DG, several 3-D data sets were stitched together. For this purpose, the stitching plugin of Fiji was used.[28] Stitching was performed in two steps to optimize the processing speed. First, substacks of the 3-D data sets were created using a MATLAB script. Each substack contained 15% of the full stack. In a second step, each substack was stitched to its respective neighboring substack yielding the best overlap in terms of the cross correlation measure. Based on this information, the full 3-D stacks were stitched.

A final step to improve the contrast throughout the 3-D data was performed after stitching. This was done to compensate possible intensity variations of the sample in axial direction. To this end, a histogram equalization was performed in every image plane of the stitched data set. For calculation of z-projections, the maximum intensity projection algorithm of Fiji was used.

Selected image stacks as outlined in the results section were spatially deconvolved using Huygens software (Professional version 17.04, Scientific Volume Imaging, The Netherlands) using theoretical PSFs and the classical maximum likelihood estimation algorithm. The deconvolution software provides as output the PSF, which was determined by analysis of fluorescent microbeads embedded in 1% agarose gel.

The 3-D representation of the data was achieved using the Surpass view in Imaris (Version 9.10 Bitplane Inc., Zurich, Switzerland). Data processing was performed on a workstation equipped with two Intel Xeon Platinum 8160 CPU (2.1 GHz, 24 cores), 512 GB memory, and an Nvidia Quadro P5000 GPU (16 GB GDDR5X) running under Windows 10 Pro.

4.10 *Determination of the Expansion Factor*

The magnification factor of expansion microscopy was experimentally determined by comparing the short width of the cell soma of labeled granule cells in images obtained from samples before expansion (Fig. 1) with those after expansion (Fig. 2). From Fig. 1, we obtained a soma width of 10.1 ± 0.6 μm ($n = 25$). For three different expansion experiments, we determined a soma width of 35.6 ± 1.7, 43.3 ± 1.7, and 39.8 ± 2.6 μm. Thus, the average expansion factor was 3.9 ± 0.3.

Disclosures

No conflicts of interest, financial or otherwise, are declared by the authors.

Acknowledgments

This work was supported by the German Research Foundation (Grant Nos. KU 2474/13-1, INST 217/886-1, SCHW 1578/2-1 and SFB 1089/P03).

References

1. S. Ramón and Y. Cajal, *Textura del sistema nervioso del hombre y de los vertebrados*, Imprenta y Librería de Nicolás Moya, Madrid (1899–1904).
2. S. Mikula and W. Denk, "High-resolution whole-brain staining for electron microscopic circuit reconstruction," *Nat. Methods* **12**(6), 541–546 (2015).
3. P. Osten and T. W. Margrie, "Mapping brain circuitry with a light microscope," *Nat. Methods* **10**(6), 515–523 (2013).
4. J.-A. Conchello and J. W. Lichtman, "Optical sectioning microscopy," *Nat. Methods* **2**(12), 920–931 (2005).
5. F. Helmchen and W. Denk, "Deep tissue two-photon microscopy," *Nat. Methods* **2**(12), 932–940 (2005).
6. J. Tang, R. N. Germain, and M. Cui, "Superpenetration optical microscopy by iterative multiphoton adaptive compensation technique," *Proc. Natl. Acad. Sci. U. S. A.* **109**(22), 8434–8439 (2012).
7. K. D. Micheva et al., "Single-synapse analysis of a diverse synapse population: proteomic imaging methods and markers," *Neuron* **68**(4), 639–653 (2010).
8. T. Ragan et al., "Serial two-photon tomography for automated ex vivo mouse brain imaging," *Nat. Methods.* **9**(3), 255–258 (2012).
9. D. Zhu et al., "Recent progress in tissue optical clearing," *Laser Photonics Rev.* **7**(5), 732–757 (2013).
10. D. S. Richardson and J. L. Cell, "Clarifying tissue clearing," *Cell* **162**(2), 246–257 (2015).
11. K. Tainaka et al., "Chemical principles in tissue clearing and staining protocols for whole-body cell profiling," *Annu. Rev. Cell Dev. Biol.* **32**(1), 713–741 (2016).
12. R. J. Vigouroux, M. Belle, and A. Chédotal, "Neuroscience in the third dimension: shedding new light on the brain with tissue clearing," *Mol. Brain* **10**(1), 33 (2017).
13. S.-Y. Kim, K. Chung, and K. Deisseroth, "Light microscopy mapping of connections in the intact brain," *Trends Cogn. Sci. (Regul. Ed.)* **17**(12), 596–599 (2013).
14. K. Chung et al., "Structural and molecular interrogation of intact biological systems," *Nature* **497**(7449), 332–337 (2013).
15. F. Chen, P. W. Tillberg, and E. S. Boyden, "Optical imaging. Expansion microscopy," *Science* **347**(6221), 543–548 (2015).
16. T. J. Chozinski et al., "Expansion microscopy with conventional antibodies and fluorescent proteins," *Nat. Methods* **13**(6), 485–488 (2016).
17. J.-B. Chang et al., "Iterative expansion microscopy," *Nat. Methods* **14**(6), 593–599 (2017).
18. H.-U. Dodt, "Microscopy. The superresolved brain," *Science* **347**(6221), 474–475 (2015).
19. H.-U. Dodt et al., "Ultramicroscopy: three-dimensional visualization of neuronal networks in the whole mouse brain," *Nat. Methods* **4**(4), 331–336 (2007).
20. L. Silvestri et al., "Confocal light sheet microscopy: micron-scale neuroanatomy of the entire mouse brain," *Opt. Express* **20**(18), 20582–20598 (2012).
21. M. K. Schwarz et al., "Fluorescent-protein stabilization and high-resolution imaging of cleared, intact mouse brains," *PLoS One* **10**(5), e0124650 (2015).
22. J. Doerr et al., "Whole-brain 3D mapping of human neural transplant innervation," *Nat. Commun.* **8**, 14162 (2017).
23. A. H. Voie, D. H. Burns, and F. A. Spelman, "Orthogonal-plane fluorescence optical sectioning: three-dimensional imaging of macroscopic biological specimens," *J. Microsc.* **170**(Pt 3), 229–236 (1993).
24. J. Huisken et al., "Optical sectioning deep inside live embryos by selective plane illumination microscopy," *Science* **305**(5686), 1007–1009 (2004).
25. E. H. K. Stelzer, "Light-sheet fluorescence microscopy for quantitative biology," *Nat. Methods* **12**(1), 23–26 (2015).
26. E. Baumgart and U. Kubitscheck, "Scanned light sheet microscopy with confocal slit detection," *Opt. Express* **20**(19), 21805–21814 (2012).
27. K. Korobchevskaya et al., "Exploring the potential of airyscan microscopy for live cell imaging," *Photonics* **4**, 41 (2017).
28. S. Preibisch, S. Saalfeld, and P. Tomancak, "Globally optimal stitching of tiled 3D microscopic image acquisitions," *Bioinformatics* **25**(11), 1463–1465 (2009).
29. R. M. Power and J. Huisken, "A guide to light-sheet fluorescence microscopy for multiscale imaging," *Nat. Methods* **14**(4), 360–373 (2017).
30. D. Toomre and J. Bewersdorf, "A new wave of cellular imaging," *Annu. Rev. Cell Dev. Biol.* **26**(1), 285–314 (2010).
31. K. Sawada et al., "Super-resolution structural analysis of dendritic spines using three-dimensional structured illumination microscopy in cleared mouse brain slices," *Eur. J. Neurosci.* **47**(9), 1033–1042 (2018).
32. P. W. Tillberg et al., "Protein-retention expansion microscopy of cells and tissues labeled using standard fluorescent proteins and antibodies," *Nat. Biotechnol.* **34**(9), 987–992 (2016).
33. P. J. Keller and H.-U. Dodt, "Light sheet microscopy of living or cleared specimens," *Curr. Opin. Neurobiol.* **22**(1), 138–143 (2012).
34. X. Zhu et al., "Optical brain imaging: a powerful tool for neuroscience," *Neurosci. Bull.* **33**, 95–102 (2017).
35. B.-C. Chen et al., "Lattice light-sheet microscopy: imaging molecules to embryos at high spatiotemporal resolution," *Science* **346**, 439–453 (2014).
36. S. Gong et al., "Targeting Cre recombinase to specific neuron populations with bacterial artificial chromosome constructs," *J. Neurosci.* **27**(37), 9817–9823 (2007).

Jana Bürgers received her bachelor's and master's degrees in physics from the University of Bonn in 2014 and 2016, respectively. Now, she is PhD student in the Biophysical Chemistry Group of the University Bonn. Her research interests include light sheet, lattice light sheet, and expansion microscopy.

Irina Pavlova received her master's degree in neurosciences from the University of Bonn in 2017. Currently, she is a PhD student in the Functional Neuroconnectomics Group at the Institute of Experimental Epileptology and Cognition Research, University of Bonn Medical School. In the present time, her research interests are focused on the odor-driven centrifugal modulation of the olfactory perception.

Juan E. Rodriguez-Gatica studied electronic engineering and received her master's degree from the University of Concepcion, Chile, in 2014, doing internships at Columbia University, USA, and University of Waterloo, Canada. Until 2016, he worked at the SCIAN-Lab at the Universidad de Chile. Currently, he is making his PhD in the Biophysical Chemistry Group at the University of Bonn. His research interests include light sheet and expansion microscopy and analysis of 2-D/3-D microscopic images.

Christian Henneberger studied medicine at the Humboldt and Free University Berlin and received his degree in 2003. After completing his thesis in developmental neurobiology and postdoctoral research at the Charité (Berlin, Germany) and the University College London (United Kingdom), he became professor at the University of Bonn, Germany, in 2011. His research interests include learning processes, the underlying neuronal and non-neuronal processes and their investigation using novel optical tools.

Marc Oeller received his bachelor's and master's degrees from the University of Bonn, Germany, in 2016 and 2018, respectively. Currently, he is a PhD candidate in Prof. Vendruscolo's Group in the Centre for Misfolding Diseases at the University of Cambridge, UK. His main research focus is protein solubility and biophysical analysis of protein folding.

Jan A. Ruland received his bachelor's and master's degrees from the University Bonn in 2014 and 2016, respectively. Now, he is a PhD student at University Bonn, since 2016, in the Biophysical Chemistry Group. His research interests include single molecule tracking, confocal microscopy, and ribosome biogenesis.

Jan P. Siebrasse received his diploma from the Institute of Immunology of the University of Münster, Germany, and his doctoral degree from the Institute of Medical Physics and Biophysics. He was a postdoc in the Nano Channel Optronics Group at the Center for Nanotechnology in Münster and at the Research & Development Department of Teutopharma GmbH, Glandorf, Germany, before joining the Biophysical Chemistry Group of the University Bonn.

Ulrich Kubitscheck leads the Department of Biophysical Chemistry at the University of Bonn, Germany. He obtained his academic degrees from the University of Bremen, spent his career working at The Weizmann Institute of Science, Israel, and the University of Münster, Germany, before taking up his position in Bonn. He develops light sheet fluorescence microscopic and single molecule imaging techniques for studying neuroconnectomics as well as mRNA processing and nucleocytoplasmic transport within living cells.

Martin K. Schwarz received his diploma from the Institute of Molecular Pathology (IMP) in Vienna in 1995 and his doctoral degree from the University of Vienna for his thesis carried out at the Max-Planck Institute for Biophysical Chemistry in Goettingen in 1998. Now, he is leading his Independent Research Group at the Institute of Experimental Epileptology and Cognition Research at the University of Bonn. His research interests include neuroconnectomics, biomedical optics, and their applications.

A2. Second paper: Hard-wired lattice light-sheet microscopy for imaging of expanded samples

Reproduced with permission from

Stockhausen, A., Bürgers, J., **Rodriguez-Gatica, J. E.**, Schweihoff, J., Merkel, R., Prigge, J. M., Schwarz, M. K. and Kubitscheck, U. (**2020**). Hard-wired lattice light-sheet microscopy for imaging of expanded samples. Optics express 28, 15587–15600.

DOI: https://doi.org/10.1364/OE.393728

Contributions

- Experimental design for expansion
- Sample preparation
- Writing the manuscript

Research Article Vol. 28, No. 10 / 11 May 2020 / *Optics Express* 15587

Optics EXPRESS

Hard-wired lattice light-sheet microscopy for imaging of expanded samples

ANNE STOCKHAUSEN,[1,5] JANA BÜRGERS,[1,5] JUAN EDUARDO RODRIGUEZ-GATICA,[1] JENS SCHWEIHOFF,[2] RUDOLF MERKEL,[3] JENS MARKUS PRIGGE,[4] MARTIN KARL SCHWARZ,[2] AND ULRICH KUBITSCHECK[1,*]

[1] *Institute of Physical and Theoretical Chemistry, University of Bonn, Wegelerstr. 12, 53115 Bonn, Germany*
[2] *Institute for Experimental Epileptology and Cognition Research (EECR), University of Bonn Medical School, Sigmund-Freud-Str. 25, 53127 Bonn, Germany*
[3] *Institute of Biological Information Processing 2: Mechanobiology, Forschungszentrum Jülich GmbH, 52425 Jülich, Germany*
[4] *Institute of Biological Information Processing: Mechanics Workshop, Forschungszentrum Jülich GmbH, 52425 Jülich, Germany*
[5] *These authors contributed equally to this research*
[*] *u.kubitscheck@uni-bonn.de*
https://www.chemie.uni-bonn.de/pctc/kubitscheck

Abstract: Light-sheet fluorescence microscopy (LSFM) helps investigate small structures in developing cells and tissue for three-dimensional localization microscopy and large-field brain imaging in neuroscience. Lattice light-sheet microscopy is a recent development with great potential to improve axial resolution and usable field sizes, thus improving imaging speed. In contrast to the commonly employed Gaussian beams for light-sheet generation in conventional LSFM, in lattice light-sheet microscopy an array of low diverging Bessel beams with a suppressed side lobe structure is used. We developed a facile elementary lattice light-sheet microscope using a micro-fabricated fixed ring mask for lattice light-sheet generation. In our setup, optical hardware elements enable a stable and simple illumination path without the need for spatial light modulators. This setup, in combination with long-working distance objectives and the possibility for simultaneous dual-color imaging, provides optimal conditions for imaging extended optically cleared tissue samples. We here present experimental data of fluorescently stained neurons and neurites from mouse hippocampus following tissue expansion and demonstrate the high homogeneous resolution throughout the entire imaged volume. Utilizing our purpose-built lattice light-sheet microscope, we reached a homogeneous excitation and an axial resolution of 1.2 µm over a field of view of (333 µm)^2.

1. Introduction

In the past years, light-sheet fluorescence microscopy (LSFM) revolutionized light microscopic imaging in developmental biology of mammals, insects and plants [1] but also in three-dimensional localization microscopy and large field brain imaging in neuroscience [2,3].

In marked contrast to epi-illumination microscopy in LSFM fluorescence excitation and detection occur along orthogonally arranged beam paths. Typically, the sample is illuminated by a thin sheet of light, which is either stationary and generated by a cylinder lens, or generated by scanning a thin excitation beam. This approach enables fast imaging of an entire illuminated plane, which is in the focus of a detection objective lens and visualized by a sensitive CCD or CMOS camera. Thus LSFM features intrinsic optical sectioning and low photobleaching, since fluorescence excitation and photobleaching are confined to a single object plane. Moreover, image contrast is significantly better compared to epi-illumination microscopy and is further

#393728 https://doi.org/10.1364/OE.393728
Journal © 2020 Received 26 Mar 2020; revised 27 Apr 2020; accepted 28 Apr 2020; published 7 May 2020

improved by using the scanned laser beam configuration for illumination and synchronized line detection, which produces a confocal line detection scheme [4,5].

Initially, scanned light-sheets were generated with classical Gaussian beams [6], but recently also two-photon excitation [7], Bessel [8,9], Airy [10] beams, or even stimulated excitation-depletion (STED) excitation [11] were introduced (for review, see [12]). Briefly, Gaussian beams are straightforward to produce, but their useful Rayleigh length in propagation direction is related to the square of their diameter and thus resulting in a marked reduction of the actual illumination field. Two photon excitation beam profiles are spatially quite confined, however, the instrumentation is fairly expensive. Airy beams are similarly constant along their propagation direction, however, suffer also from strong side lobes. STED excitation is spatially extremely confined, but the required laser setup is complex and expensive. Moreover, it is not compatible with all combinations of fluorescent dyes. Bessel beams are self-reconstructive and have a thin main maximum, which is however surrounded by relatively strong side lobes, which lead to a high out-of-focus contribution.

A few years ago, Eric Betzig and coworkers introduced lattices of Bessel beams as an alternative excitation mode [13]. In their setup a spatial light modulator was used to generate a lattice of Bessel beams that were so close to each other that the side lobes interfered destructively, thus minimizing out of focus contributions. Importantly the Bessel beams retained their feature of being self-reconstructive, which lead to a significantly extended axial range in beam propagation direction. The resulting light lattice could either be swept across the object plane for creating a light-sheet, or alternatively used to increase the axial resolution by moving the lattice step-wise, creating a structured illumination microscopy mode. This instrument setup featured high imaging frame rates and a superior axial resolution and was optimally adjusted to examine small transparent objects. In a previous project we demonstrated the use of classical LSFM to image sections of mouse brain slices following tissue expansion [14]. Tissue expansion allowed us to optically resolve fluorescent structures spaced closer than the optical diffraction limit yielding effective super resolution images. As a result the achieved effective resolution and overall image quality was superior compared to classically cleared tissue imaged by LSFM. However, the large samples size afforded imaging in a mosaic-like fashion. The converging/diverging character of Gaussian beams further reduced the usable field of view for each mosaic tile.

Thus, to increase axial resolution across the excitation field and reduce out-of-focus excitation as well as imaging time of large expanded samples at high resolution we here implemented lattice light-sheet microscopy (LLSFM). LLSFM is ideally suited for this purpose due to the formation of partly self-reconstructive illumination beams leading to larger imaging fields. We here present a purpose-built instrument that provides robust and rapid imaging, especially for transparent extended samples. We report on the construction of this imaging instrument, the quantitative characterization of its optical features and finally its application in imaging expanded mouse brain section samples revealing critical details of neuronal networks.

2. Methods

In any microscope the light pattern in the front focal plane of a lens is determined by the light pattern in the back focal plane of the objective. Both distributions are related to each other by a Fourier transformation. In light-sheet microscopy illumination and detection occur by two distinct objective lenses. Thus, we defined the illumination light pattern in the sample space by placing a defined mask into a plane conjugated to the back focal plane of the illumination objective. The theoretically expected illumination light pattern was calculated using discrete fast Fourier transformation algorithms from MATLAB (Version R2014a, The MathWorks, Inc., Natick, Massachusetts, United States). An infinitely thin ring pattern in the back focal plane results in a Bessel beam along the illumination axis (x-direction). Inspired by Chen et al [13]. we considered a mask featuring thin vertical slots confined on a ring. As demonstrated by Chen et al. ([13], also, see [15]) and our own simulations this leads to a confined optical lattice in the sample plane, whose individual beams are low-diverging Bessel-Gaussian beams. The final result is defined by the parameters of the slit mask, namely the outer diameter of the ring, D_1, its width, d, the number, A, and the width of the slits, T. A finite ring width causes the formation of mixed Bessel-Gaussians beams, which are not completely propagation-invariant like perfect Bessel beams. The number of slits defines the density of the Fourier pattern in the sample space. To generate a homogeneous pattern in the sample plane it is optimal to employ a small number of slits. The lattice pattern is thinner in the direction of the detection beam path (z-direction), if the outermost slits in the mask are tangential to the inner radius of the ring. For these certain distances of the slits the side lobes of the Bessel beams in the lattice interfere efficiently in a destructive manner. The slit width T is inversely related to the width of the overall beam lattice. For a wide lattice achieving illumination of a large object field a small slit width should be chosen. Obviously, this simultaneously limits the light transmission efficiency of the mask.

We decided to use a mask with three slits as shown in Fig. 1. The MATLAB simulation allowed to compute the resulting light distribution in the illumination plane. Program input are the ring parameters, D_1 and d, and the slit parameters, T and A, respectively (Fig. 1(a)). The resulting image, which shows the defined slits confined to the specific ring (Fig. 1(b)), is transformed into a binary 4000×4000 matrix. The matrix entries are set to unity at the light transmitting slit positions and to zero elsewhere. This matrix is two dimensionally Fourier transformed using the function *fft2* and squared to compute the intensity of the optical lattice (Fig. 1(c)). In this way, the expected light pattern of the lattice light-sheet can be simulated.

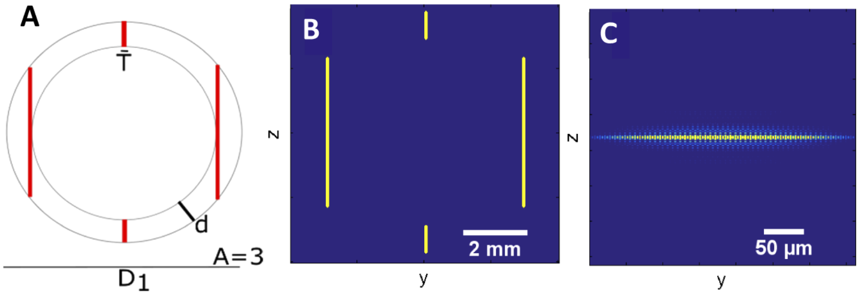

Fig. 1. Mask with three slits. (a) Definition of mask parameters. (b) Sketch of the mask with D_1=7.5 mm, d=0.8 mm, width T=100 µm. (c) Simulated intensity distribution in the central maximum of the diffraction pattern.

The mask was produced in a precision mechanics workshop using a computerized numerical control (CNC) milling machine (DMC 650 V, DMG Mori, Bielefeld, Germany) equipped with a solid carbide miniature end mill (VHM 0.1 mm diameter, Karnasch, Heddesheim, Germany). This machine enabled to create slits with a minimum width of 100 µm in an aluminum plate. The complete beam path of the microscope is shown in Fig. 2.

We used two separate illumination beam paths that allowed us to directly compare the properties of the lattice light-sheet and a Gaussian beam illumination. The illumination arm on the left-hand side generated the lattice light-sheet illumination. The incoming laser beams originating from a laser hub (C-FLEX, Hübner Photonics, Kassel, Germany) emitting laser lines at 405, 488, 561 and 638 nm were brought to the instrument by an optical monomode fiber. The incoming light passed a λ/2 plate and was split by a polarizing beam splitter. Typically, an excitation power of 70 mW per laser line – measured behind the beam splitter – was used. On the right-hand side a normal illumination beam path using a scanned Gaussian beam was assembled [14]. For focusing the beam into the sample, we used an air objective lens (10x, numerical aperture (NA) 0.28, working distance (WD) 33.5 mm, Mitutoyo, Mitutoyo Corp., Kawasaki, Japan). In the

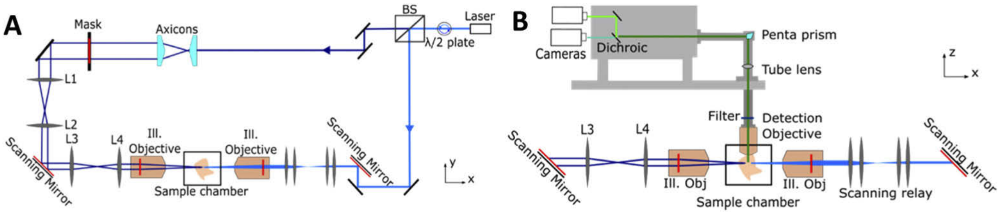

Fig. 2. Setup of the lattice light-sheet microscope. (a) Top view of the illumination beam path comprising the mask (upper section and left) and the Gaussian illumination (right-hand side). Conjugate planes were marked in red. (b) Side view of the instrument showing the detection beam path.

second beam path we used two axicons (AX2510-A, Thorlabs, Bergkirchen, Germany) to create a ring-shaped beam profile. The diameter of the ring profile is defined by the distance between the axicons. The resulting ring beam illuminated the mask. Without the axicons, the major part of the illumination beam would be blocked by the mask. Still, the light loss at the mask amounted to 93.5%. The lenses L1 (f=100 mm) and L2 (f=50 mm) mapped the mask onto the scanning mirror, which dithered the lattice pattern, and de-magnified it by a factor of 2. Two final lenses L$_3$ and L$_4$ (f = 75 and 60 mm, respectively; all lenses from Thorlabs) imaged the dithered mask pattern into the back focal plane of the illumination objective (10x, NA 0.28, WD 33.5 mm, Mitutoyo). Here, typically laser irradiances of 4 mW were measured. The conjugate planes of the mask are marked in red in Fig. 2(a). The scanning mirror, the lenses L$_3$ and L$_4$, as well as the illumination objective were mounted on a linear stage (LNR50K1/M, Thorlabs) to enable the adjustment of the lattice foci with respect to the detection axis.

The light lattice was formed in a custom-built, water-filled sample chamber. The chamber featured entrance windows at both sides with a thickness of 170 μm. The biological specimen itself was fixed by poly-L-lysine on a coverslip, which could be moved on a handle in three spatial directions by individual computer-controlled step motors (Micro Translation Stage M-112.1DG, Physik Instrumente GmbH, Karlsruhe, Germany) to allow automatic image acquisition from any sample location. To image biological samples, the pH value of the solution in the chamber was adjusted to 7.4 to improve fluorophore stability.

For light detection, we used a water dipping objective lens (40x, NA 1.0, Carl Zeiss Microscopy, Jena, Germany) with a WD of 2.5 mm. A tube lens changer allowed to introduce an optional magnification of 1.6. A set of Notch filters centered at the respective excitation wavelengths filtered the emitted fluorescence light, which was guided by a pentaprism into a beam splitter device (W-View Gemini-2C, Hamamatsu Photonics K. K., Hamamatsu City, Japan). The latter allowed to image two different fluorescence channels simultaneously by two sCMOS cameras (Orca Flash 4.0 V3, Hamamatsu Photonics) featuring 2048 × 2048 pixels with a pixel size of 6.5 μm. Using the 40x magnification the field of view amounted to (333 μm)^2 with an object pixel size of 162.5 nm. This pixel size fulfilled the Nyquist condition for green, yellow and red fluorescence, but not for blue. The use of the second tube lens, however, reduced the object field pixel size to 101.6 nm, which was well beyond the Nyquist limit for all fluorescence channels. The complete instrument was governed by a custom-developed LabVIEW software (National Instruments, Austin, Texas, USA) for directing the laser hub, scanners, cameras and motors. It allowed live image display and tiled image stack acquisition.

3. Results

3.1. Illumination pattern

The mask produced the expected diffraction pattern in the sample representing a grid of parallel light beams. The grid could be observed by illuminating the sample chamber filled with a diluted fluorescein solution and imaging the stationary pattern (Fig. 3). Computed and measured illumination light distribution differed mostly by a broad background in the latter. This was created by out of focus light registered by the camera. The distances between the lattice maxima $d_{exp} = (3.4 \pm 0.2)$ µm observed in the fluorescein solution agreed with the simulation-predicted values, $d_{sim} = 3.2$ µm within the standard deviation. We assume that the observed deviations were due to small imperfections in the produced mask and optical aberrations in the illumination beam path.

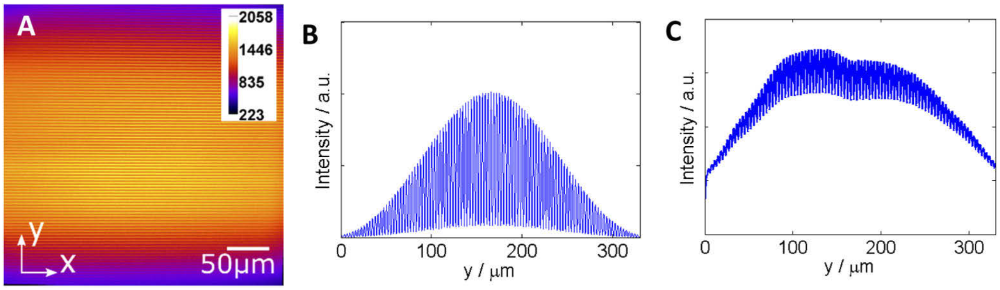

Fig. 3. Optical lattice produced in the sample chamber. (a) Image of the lattice over a field of $(333\,\mu m)^2$. (b) Theoretically calculated intensity distribution in y-direction. (c) Intensity profile in y-direction from Fig. 3(a).

3.2. Variation of excitation wavelength

Comparable diffraction patterns were produced by laser lines exhibiting different wavelengths. For demonstration, water solutions containing Alexa Fluor 532 and Alexa Fluor 647 were prepared and illuminated (Fig. 4). The distances between the maxima and their widths increased linearly with increasing wavelength from 488 nm, over 561 nm to 638 nm as theoretically expected. Similarly, the position of the beam waists in the illumination (x-) direction depends on the excitation wavelength. We adjusted the linear stage that contained a part of the illumination beam path such that the 561 nm laser beam waist was positioned at the location of the detection beam path. The 488 nm laser focus was shifted 10 µm to the left and the 638 nm focus was shifted 12 µm to the right.

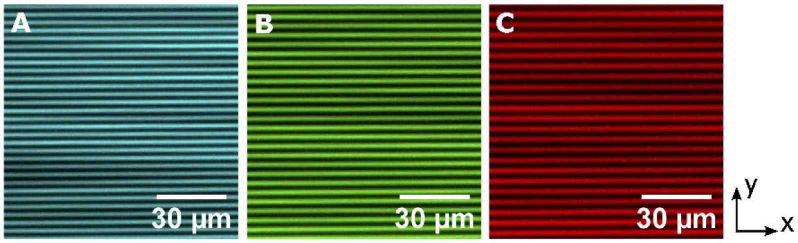

Fig. 4. Optical lattices produced in the sample chamber using different excitation wavelengths over a field of $(100\,\mu m)^2$ for an excitation wavelength of (a) 488 nm, (b) 561 nm, and (c) 638 nm.

Notably, due to the design of a light-sheet microscope the lattices of all three excitation lasers are positioned in a single plane with regard to the detection axis, which is advantageous for simultaneous multicolor imaging.

3.3. Resolution and illumination field size

The convergence and divergence of the Gaussian illumination beam beyond the focus region is a clear disadvantage of classical LSFM, especially when imaging extended samples [14]. A propagation-invariant Bessel beam illumination can definitely improve this situation [8,9]. We therefore expected an improved axial uniformity of the illumination field as a key feature of lattice illumination. In addition, the axial extension of a Bessel lattice is reduced compared to that of a Gaussian beam, resulting in an increased axial resolution across the excitation field and a reduced out-of-focus excitation [13].

For Gaussian beams the usable field width corresponds approximately to twice the Rayleigh length, L_R, of the beam, see below. Beyond this region the divergence of the beam leads to a strong decrease in the optical sectioning capability of the setup. We compared usable illumination field sizes of two different Gaussian beams and of lattice illumination.

To this end we chose Gaussian beams with narrow and wide beam waists, $\omega_{0,n}$ and $\omega_{0,w}$, respectively, with a wavelength of 488 nm. The beam intensity profiles were visualized using the fluorescence that was excited by the stationary beams in a diluted fluorescein solution by means of the sCMOS camera (Figs. 5(a) and (b)).

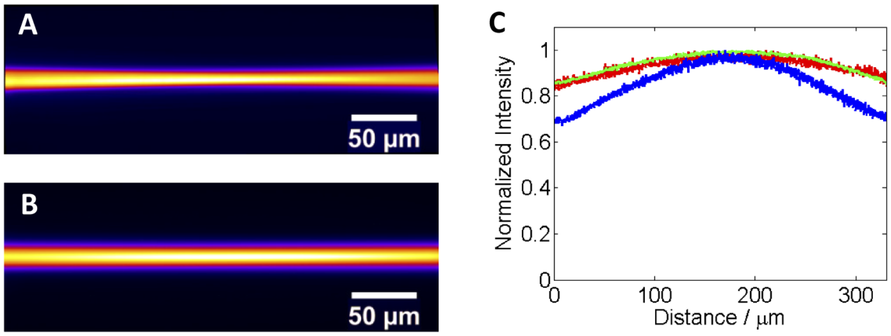

Fig. 5. Images of the various illumination fields imaged in fluorescein: (a) Narrow Gaussian beam, (b) wide Gaussian beam. The narrow beam resulted from a two-fold expansion of the wide Gaussian beam before the illumination objective, what results in a thinner beam waist in the sample plane. (c) Intensity profiles in illumination direction for the two Gaussian beams and the lattice illumination. (red, lattice; green, wide Gaussian beam; blue, narrow Gaussian beam)

The beam waist radii of the Gaussian beams were measured using the knife edge method within the sample chamber. The narrow Gaussian beam was adjusted such that its $1/e^2$-waist $\omega_{0,n} = (3.4 \pm 0.3)$ µm corresponded to that of the lattice beams, $\omega_{0,lb} = (3.5 \pm 0.3)$ µm for λ=488 nm. The widths of the lattice beams were determined by directly imaging the beam profiles using the detection pathway and a 45° mirror at the focus position in the sample chamber.

For Gaussian beams L_R and ω_0 are related to each other by

$$L_R = \frac{n\,\pi\,{\omega_0}^2}{\lambda}, \tag{1}$$

where n denotes the refractive index of the medium. Using Eq. (1) the Rayleigh lengths of the profiles could be directly deduced from the beam waist radii. Therefore, the depth of field of the focused narrow beam amounted to $2\,x\,L_{R,n}$ =(198 ± 17) µm. The observed qualitative beam profile exhibited the typical maximum at the waist position (5C, blue).

The wide Gaussian beam radius was adjusted to $\omega_{0,\mathrm{w}} = (5.5 \pm 0.3)$ µm such that its longitudinal intensity profile corresponded to that of the lattice beams over the field of view (Fig. 5(c), green). The field of view achieved with this beam amounted to $2\,x\,L_{R,w} = (518 \pm 56)$ µm and was close to that determined for the lattice light-sheet, $2\,x\,L_{R,lb} = (535 \pm 43)$ µm. The Rayleigh length of the lattice, $L_{R,lb}$, was estimated by the MATLAB simulation on the basis of the measured beam width, $\omega_{0,\mathrm{lb}} = (3.5 \pm 0.3)$ µm. All values are summarized in Table 1.

Table 1. Comparison of beam waists, field of view and measured axial resolution.

	Lattice	Wide Gaussian	Narrow Gaussian
ω_0 in water n=1.33	(3.5 ± 0.3) µm	(5.5 ± 0.7) µm	(3.4 ± 0.3) µm
Two-fold Rayleigh length at 488nm, n=1.33	(535 ± 43) µm	(518 ± 56) µm	(198 ± 17) µm
Intensity decrease in propagation direction (Fig. 5(c))	85%	85%	70%
Best axial resolution	(1.2 ± 0.2) µm	(1.4 ± 0.2) µm	(1.2 ± 0.2) µm

The optical resolution is determined by the product of the illumination intensity distribution and the detection point spread function. The theoretical expectation for the FWHM of the axial resolution for a sheet created by scanning of the narrow beam at a detection wavelength of 520 nm using a NA 1.0 objective amounted to 1.07 µm. This value was calculated using the approach presented previously [14,16].

The experimentally realized resolution can be measured using submicron-sized fluorescent beads. Thus, we imaged green fluorescent beads with a diameter D=0.2 µm immobilized in a 1% agarose gel. The refractive index of the 1% agarose gel is close to that of water (n=1.332, [17]). The beads were illuminated by 488 nm laser light using the scanned lattice beams and both Gaussian beams. The respective axial resolutions FWHM_z over the image field were determined by the acquisition and evaluation of image stacks with an axial step size of Δz=0.2 µm. The lateral and axial resolutions were determined as a function of position along the illumination axis by plotting the intensity profiles using Fiji [18] as full width at half maximum (FWHM) of the bead signals, $\mathrm{FWHM}_{\mathrm{b,xy}}$ and $\mathrm{FWHM}_{\mathrm{b,z}}$, respectively (Fig. 6(a)). We corrected the measured values for the finite bead size according to $FWHM = \sqrt{FWHM_b^2 - D^2}$. The smallest values for the axial resolution within the illumination fields for the Gaussian beams were observed at the locations of the beam waists, as expected (Fig. 6(b)). The best axial resolutions were obtained for the lattice illumination and for the narrow Gaussian beam, namely $\mathrm{FWHM}_z = (1.2 \pm 0.2)$ µm. The best axial resolution achieved with the wide Gaussian beam corresponded to $\mathrm{FWHM}_z = (1.4 \pm 0.2)$ µm.

In summary, our lattice illumination combined the advantages of a large lateral illumination field size featuring a comparatively constant illumination intensity with a small axial sheet thickness, required to achieve optimal axial resolution.

3.4. Imaging of an expanded mouse brain section

In order to evaluate the performance of the constructed lattice light-sheet microscope in large expanded samples of the dorsal dentate gyrus (DG) of a mouse brain, we imaged GFP-labeled granule cells and their neurites to achieve super resolved representations. Briefly, coronal DG sections were prepared for tissue expansion and LSFM analysis from a PROX1-Cre mouse injected with rAAV-DIO-EGFP-WPRE to achieve selective expression of EGFP in DG granule cells [14]. The samples were prepared in the following way. Prox1-Cre transgenic mice were maintained on a 12 hours light/12 hours dark cycle with food and water always available. All the experiments were carried out in accordance with the German animal protection law (TierSCHG), FELASA and were approved by the animal welfare committee of the University of Bonn. Viral

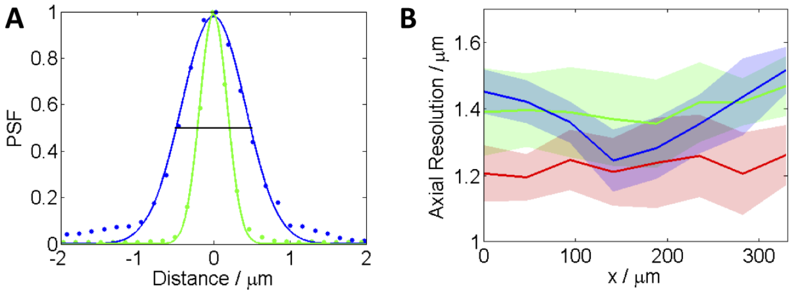

Fig. 6. Axial resolution. (a) Determination of FWHM values of an exemplary bead (blue dotted line, normalized intensity values along the detection axis; green dotted line, normalized intensity values in lateral direction; full line, results of fitting a Gaussian function; FWHM indicated by the black line). (b) Axial resolution as a function of position along the illumination direction. The colored curves show the mean values of N=10 beads in each x-interval, the shaded regions indicate the standard deviations (red, lattice; green, wide Gaussian beam; blue, narrow Gaussian beam)

injections were performed under aseptic conditions in Prox1-Cre mice up to 10 months old. The mice were anesthetized with a mixture of Fentanyl (Rotexmedica, Trittau, Germany), Midazolam (Rotexmedica), and Domitor (Orion Pharma, Hamburg, Germany) via intraperitoneal injection (0.05/5.0/0.5 mg/kg). Analgesia (5 mg/kg of Carprofen) was administered intraperitoneally prior to the injection, and Xylocain (AstraZeneca, Germany) was used for local anesthesia. Stereotactic injections were performed using an injection frame (WPI Benchmark/Kopf) and a microprocessor-controlled minipump (World Precision Instruments, Sarasota, Florida), the viral solution was injected bilaterally into the hippocampus (rAAV-DIO-EGFP-WPRE). After the injection, the scalp was sutured with PERMA-HAND Silk Suture (Ethicon), and an antibacterial ointment (Refobacin, Almirall, Germany) was applied, followed by the intraperitoneal injection of a mixture of Naloxon (B. Braun, Germany), Flumazenil (B. Braun, Germany), and Antisedan (Orion Pharma) (1.2/0.5/2.5 mg/kg). To prevent wound pain, analgesia was administered on the four following days.

After incubation, mice were anesthetized with a mixture of Xylazine (10 mg/kg; Bayer Vital, Germany) and ketamine (100 mg/kg; Bela-pharm GmbH & Co. KG, Germany). Using a peristaltic pump (peristaltic pump PLP33, Mercateo, Germany), the mice were transcardially perfused with phosphate buffered saline (PBS, 137 mM sodium chloride, 2.7 mM potassium chloride, 10 mM di-sodium hydrygen phosphate, 1.8 mM potassium dihydrogen phosphate) followed by 4% paraformaldehyde (PFA) in PBS. Brains were removed from the skull and post-fixed in 4% PFA overnight (ON) at +4°C. After fixation, the brains were moved into PBS containing 0.01% sodium azide and stored at +4°C until sectioning. Fixed brains were sectioned coronally (100 µm) using a vibratome (Leica VT1000 S) and stored in phosphate buffered solution (PBS) containing 0.01% sodium azide at +4 °C.

The expansion microscopy protocol was modified from [19,20]. The sections were incubated with 2 mM methylacrylic acid-hydroxysuccinimide ester (MA-NHS) (Sigma Aldrich) for 2 h on a shaker at room temperature. After washing three times in PBS, the sections were incubated for 1.5 hours in the monomer solution (8.6% sodium acrylate, 2.5% acrylamide, 0.15% N,N'-methylenebisacrylamide, 11.7% NaCl in PBS) on a shaker at +4°C. The sections were transferred to the gelling chamber, followed by 2 h incubation at 37°C in a gelling solution for polymerization. The gelling solution was prepared by adding 4-Hydroxy-2,2,6,6-tetramethylpiperidine 1-oxyl (4-hydroxy-TEMPO, 0.01%), N,N,N′,N′-tetramethylethylenediamine (TEMED, 0.2%), and ammonium persulfate (0.2%) to the monomer solution. After gel formation, the samples were incubated at 37°C for 16 hours in digestion buffer (50 mM Tris, 1 mM EDTA, 0.5% Triton-X100, 0.8 M guanidine hydrochloride and 16 U/ml of proteinase K; pH 8.0). The next day, the digestion buffer was removed and the sections were washed three times with PBS.

Then, the digested brain sections were incubated in blocking buffer (PBS containing 0.1% TritonX-100 and 5% bovine serum albumine) on a shaker for 5 h at room temperature to prevent unspecific binding of the primary antibody. After blocking, the sections were incubated for 24 h with the primary antibody (chicken anti-GFP; 1:500 in blocking buffer; Abcam, ab13970) on a shaker at low speed at +4°C. The following day, the sections were washed at room temperature in blocking buffer three times for 20 minutes and incubated for 24 h in Alexa Fluor 488-conjugated goat antibody against chicken IgY (H + L, 1:400 in blocking buffer; Invitrogen, A-11039) on a shaker at +4°C. For cell nuclear staining, the sample was incubated 3 h in a solution of 0.5 µg/mL 4′,6-diamidine-2′-phenylindole dihydrochloride (DAPI) in water.

For imaging, the expanded gel samples were fixed on a coverslip with poly-L-lysine to avoid movements during the measurements. A quick control of a successful sample preparation was performed using a confocal laser scanning microscope (LSM 880, Carl Zeiss Microscopy). Then, the coverslip was screwed on a sample holder arm and mounted in the imaging chamber as explained above. The chamber was filled with deionized water.

Note, that the antibody staining against EGFP was performed after the digestion step, which greatly improved the tissue permeability and reduced non-specific binding effects. Image acquisition was accomplished using a single frame exposure time of 30 ms. Altogether, acquisition of a stack of 2000 frames took 143 s which corresponds to a frame rate of 14 Hz.

The sample size greatly exceeded the lateral object field size of (333 µm)^2. Therefore, the data were acquired in a tiled manner. Volumetric data of the expanded mouse brain slices were acquired by moving the sample through the light sheet. Figure 7(a) shows a volume rendering of a single neuron, which was imaged using 16 single stacks with 2120 images each and 10% lateral overlap between adjacent stacks and z-steps of 400 nm to fulfill the Nyquist criterion. The sample was illuminated using an excitation wavelength of 488 nm. The complete imaged volume has a size of $1.2 \times 1.2 \times 0.8$ mm^3. Since the sample was expanded by a factor of approximately 4, this corresponded to a size of $0.3 \times 0.3 \times 0.2$ mm^3. After imaging the tile stacks were stitched using Imaris 9.5.1 (Bitplane AG, Zurich, Switzerland) and contrast adjusted. To this end, the intensity histograms were adjusted to homogenize brightness and contrast throughout the complete data set. Every 3D stack was first scanned to find its minimum and maximum intensity values. With the respective values a linear intensity adjustment was performed to cover the full dynamic range.

The volumetric image data shows an expanded DG neuron and its neurites. Figure 7(b) shows a rendered branched neurite from the red square marked region in Fig. 7(a). Note that tiny details and fine dendritic structures can be recognized in high resolution.

A maximum intensity projection of a stack comprising 200 images of a dendrite is shown in Fig. 7(c). Individual spines as well as thin spine necks can be well resolved. Figure 7(d) shows a magnification of the marked field in Fig. 7(c). Finally, Fig. 7(e) shows the intensity profile of a spine neck marked by a red line in the close up view in Fig. 7(d). The full width at half maximum (FWHM) of the spine intensity profile amounted to 640 nm, which corresponds to 160 nm considering the expansion factor of 4 and is thus well below the optical diffraction limit.

For calculation of z-projections, the maximum intensity projection algorithm of Fiji was used. Three-dimensional representation of data was achieved using the Surpass view in Imaris. Data processing was performed on a workstation equipped with an Intel Xeon Gold 6128 CPU (3.40 GHz, 6 cores), 512 GB memory and a Nvidia Geforce GTX 980 GPU running under Windows 10 Pro.

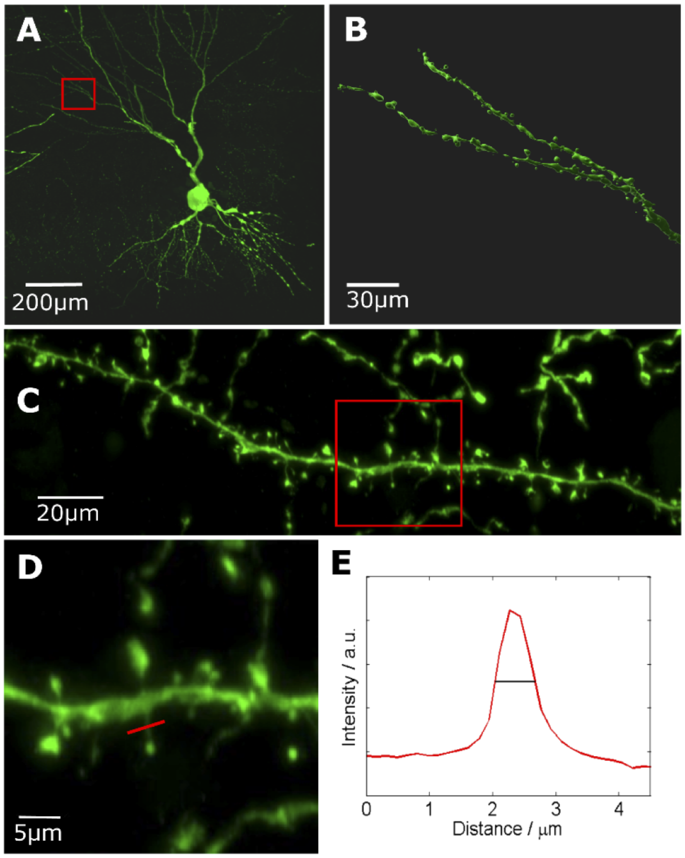

Fig. 7. Antibody stained expanded mouse brain section imaged with the lattice light-sheet. (a) Large stitched volume showing a neuron inside the mouse hippocampus. (b) The close-up shows a rendered dendrite where fine details are resolved. (d) Close up of the dendritic spines marked by the red box in (c). (e) Intensity profile of the spine neck marked with the red line in (e). The black line marks the FWHM with a length of 640 nm. All scales refer to expanded samples.

3.5. Dual-color imaging

The setup was equipped with two sCMOS cameras and a beam-splitter for simultaneous dual camera imaging. This was demonstrated by green fluorescent granule cells labeled by an Alexa488-immunostaining against EGFP and staining of cell nuclei using the UV-excitable dye DAPI. A specimen volume was imaged in 20 tiles with 1630 images each, an axial step size of 400 nm and 10% lateral overlap. The complete sample size amounted to $1.5 \times 1.2 \times 0.6$ mm^3, which corresponded to a true size of $0.38 \times 0.3 \times 0.15$ mm^3 before expansion. Figure 8(a) shows a volume rendering of the stitched and contrast-adjusted DAPI channel (pink) excited with 405 nm and the Alexa488 channel (green) excited with 488 nm. A network of four granule cells is visible together with the surrounding cell nuclei. Figure 8(b) shows a single frame of a stack to highlight the specific overlay of the cell and its DAPI stained cell nucleus.

3.6. Comparison of resolution

To validate the performance of our LLSFM in comparison to a standard Gaussian light-sheet microscope, a stack of the same region inside the expanded mouse hippocampus was acquired

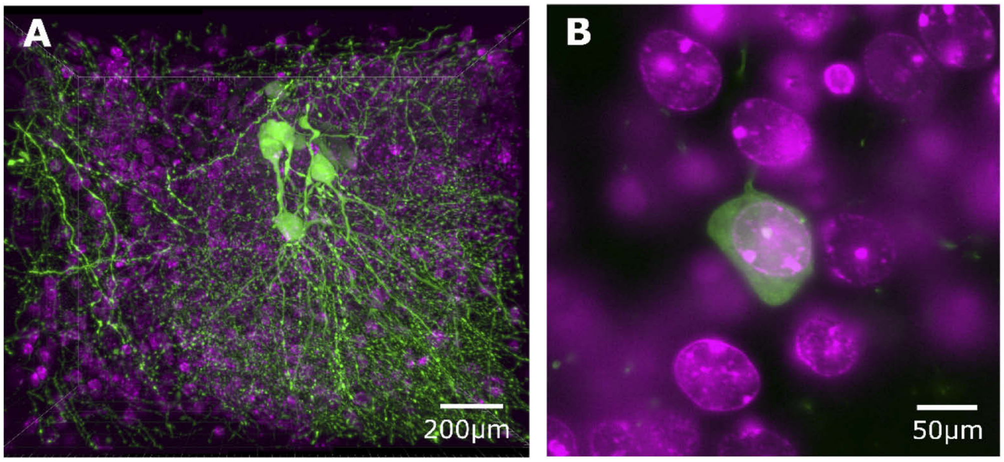

Fig. 8. Two-color imaging of a set of granule cells in an expanded mouse brain hippocampus section. (a) Large volume showing immunostained EGFP-expressing granule cells and dendrites (green) as well as cell nuclei stained by DAPI (pink) excited with 488 and 405 nm, respectively. (b) A single frame of the stack showing the overlay of the cell nucleus and the soma.

using both methods. Here, the z-step size was 300 nm. Figures 9(a) and (b) show the maximum projection of a stack with 1160 images acquired with the lattice light-sheet and the Gaussian

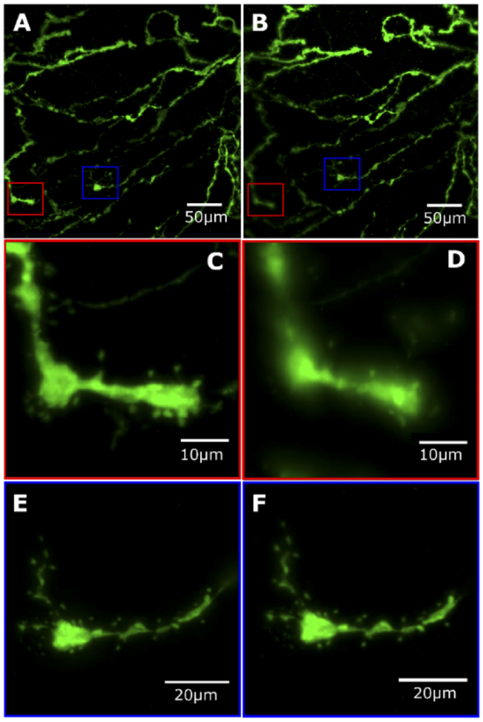

Fig. 9. Maximum intensity projections of dendrites in an expanded mouse hippocampus. (a, c, e): Lattice, (b, d, f): Gaussian. The divergence of the Gaussian beam generates blurred areas at image edges (red box). In the image center the Gaussian beam illumination reaches the resolution of the lattice (blue box).

light-sheet (w_0=3.4 ± 0.3 µm), respectively. The blue and red marked regions were chosen to compare the resolution of both methods at the image edge (blue box) and image center (red). While the Gaussian light-sheet setup yielded the same image quality in terms of resolution compared to the lattice light-sheet setup in the center of the image (compare Figs. 9(e) and (f)), the resolution decreases significantly at the image edges (compare Figs. 9(c) and (d)). Clearly, the lattice light-sheet illumination featured a constant and high resolution over the complete field of view.

4. Discussion

In contrast to conventional light-sheet microscopy employing scanned Gaussian beams for light sheet generation, lattice light-sheet microscopy features a low diverging light sheet with a homogeneous thickness formed by an array of Bessel-Gaussian beams.

We developed and characterized a rather simple and facile, purpose-built lattice light-sheet microscope based on a high precision hardware mask for lattice light-sheet generation. This custom-made mask containing three light slits generated with CNC milling was positioned in a conjugated plane of the back focal plane of the illumination objective. Our microscope setup combines both, a Gaussian and a lattice light-sheet illumination path allowing us to directly compare the features of both methods on the same sample. Notably, the characterization of the generated light lattice in dye-water solutions confirmed the results of prior simulations and thus proved that our method is applicable to simultaneous multicolor imaging due to the highly constant z-position of the lattice for different excitation wavelengths.

To thoroughly compare the performance of the lattice light-sheet microscope to our conventional LSFM setups, two Gaussian beams with different characteristics were used. First, a narrow Gaussian beam with a similar waist diameter as the lattice beams. This beam yielded the same axial resolution of (1.2 ± 0.2) µm at its focus, but the strong divergence of this Gaussian beam caused an inhomogeneous excitation intensity along the illumination direction, which led to a decrease of the axial resolution at the edges of the field of view. Second, a wide Gaussian beam, whose two-fold Rayleigh length approximated the field width of view of the lattice beams, however, featured a larger diameter which resulted in a lower axial resolution. Finally, the lattice light-sheet excitation combined a comparatively homogeneous illumination and a small axial extension which resulted in a high axial resolution. We conclude that the lattice light-sheet microscope offers the possibility for an increased usable field of view (FOV) combined with high resolution.

Compared to the LLSFM configuration by Chen et al [13]. our setup comprised no spatial light modulator (SLM). Thus, an electronic control and complex programming of the SLM is not required and therefore the overall costs for building a lattice light-sheet microscope are significantly reduced and, most notably, the optical setup using a hardware mask for lattice generation is rather straightforward. Furthermore, the aluminum plate withstands higher irradiances than a spatial light modulator, which might prove useful when combining it with pulsed light excitation. However, using a mask for lattice generation has the disadvantage that the mask light transmission is only 6% of the input light, although the incoming laser light was already transformed into a ring shape by the axicons in order to reduce light losses. Therefore, high laser power is required to achieve an adequate fluorescence excitation of the sample.

As a demonstration of the applicability of our setup, we imaged neuronal networks within expanded mouse brain samples allowing us to test its performance in imaging fine and densely packed details over large scales. We imaged mouse brain samples containing labelled EGFP-expressing granule cells additionally labeled with an antibody against EGFP to increase fluorophore density. We also used DAPI to stain the surrounding cell nuclei to demonstrate the possibility of high-resolution double color imaging. In contrast to our previous protocol [14] we here established a modification of the expansion protocol. To improve the permeability of the sample for the antibody we performed the antibody staining after sample digestion. This resulted in a rather isotropic antibody distribution within the sample and also reduced nonspecific binding. It is noteworthy to state that this approach demands a careful optimization of tissue digestion duration in order to avoid a complete destruction of the epitopes.

With our instrument, a maximum frame rate of 14 Hz was reached. A transparent sample volume of 1 mm^3 was imaged in less than 40 min while obeying the Nyquist criterion, which is significantly faster compared to our conventional setup [14]. The homogeneous excitation of the lattice light-sheet lead to a substantially increased usable field of view. In contrast a Gaussian light-sheet with the same waist diameter showed blurred structures at the image borders. This is especially important for fast imaging of large fluorescently labeled brain samples. In fact, sparsely labelled neuronal circuits, eventually spanning an entire mouse brain can theoretically be imaged in less than 3 days. Note that an observation of granule cells and their fine neurites with dendritic spines and spine necks was straightforward with negligible bleaching. Moreover, our lattice light-sheet microscope proved to be well suited for dual-color imaging.

In summary, we demonstrated that a hard-wired lattice light-sheet microscope provides a good alternative to a conventional Gaussian light-sheet microscope. Our setup presented here represents a robust and cost-effective version of a lattice light-sheet microscope and allows fast imaging of large samples at high-resolution.

Funding

Deutscher Akademischer Austauschdienst (to JERG); Comisión Nacional de Investigación Científica y Tecnológica (to JERG); Deutsche Forschungsgemeinschaft (INST 217/886-1, KU 2474/13-1, SCHW 1578/2-1).

Disclosures

The authors declare no conflicts of interest.

References

1. R. M. Power and J. Huisken, "A guide to light-sheet fluorescence microscopy for multiscale imaging," Nat. Methods **14**(4), 360–373 (2017).
2. A.-K. Gustavsson, P. N. Petrov, and W. E. Moerner, "Light sheet approaches for improved precision in 3D localization-based super-resolution imaging in mammalian cells [Invited]," Opt. Express **26**(10), 13122–13147 (2018).
3. S. Corsetti, F. Gunn-Moore, and K. Dholakia, "Light sheet fluorescence microscopy for neuroscience," J. Neurosci. Methods **319**, 16–27 (2019).
4. E. Baumgart and U. Kubitscheck, "Scanned light sheet microscopy with confocal slit detection," Opt. Express **20**(19), 21805–21814 (2012).
5. L. Silvestri, A. Bria, L. Sacconi, G. Iannello, and F. S. Pavone, "Confocal light sheet microscopy: micron-scale neuroanatomy of the entire mouse brain," Opt. Express **20**(18), 20582–20598 (2012).
6. P. J. Keller, A. D. Schmidt, J. Wittbrodt, and E. H. K. Stelzer, "Reconstruction of zebrafish early embryonic development by scanned light sheet microscopy," Science **322**(5904), 1065–1069 (2008).
7. T. V. Truong, W. Supatto, D. S. Koos, J. M. Choi, and S. E. Fraser, "Deep and fast live imaging with two-photon scanned light-sheet microscopy," Nat. Methods **8**(9), 757–760 (2011).
8. T. A. Planchon, L. Gao, D. E. Milkie, M. W. Davidson, J. A. Galbraith, C. G. Galbraith, and E. Betzig, "Rapid three-dimensional isotropic imaging of living cells using Bessel beam plane illumination," Nat. Methods **8**(5), 417–423 (2011).
9. F. O. Fahrbach and A. Rohrbach, "Propagation stability of self-reconstructing Bessel beams enables contrast-enhanced imaging in thick media," Nat. Commun. **3**(1), 632 (2012).
10. T. Vettenburg, H. I. C. Dalgarno, J. Nylk, C. Coll-Lladó, D. E. K. Ferrier, T. Čižmár, F. J. Gunn-Moore, and K. Dholakia, "Light-sheet microscopy using an Airy beam," Nat. Methods **11**(5), 541–544 (2014).
11. M. Friedrich, Q. Gan, V. Ermolayev, and G. S. Harms, "STED-SPIM: Stimulated emission depletion improves sheet illumination microscopy resolution," Biophys. J. **100**(8), L43–L45 (2011).
12. Y. Wan, K. McDole, and P. J. Keller, "Light-Sheet Microscopy and Its Potential for Understanding Developmental Processes," Annu. Rev. Cell Dev. Biol. **35**(1), 655–681 (2019).

13. B.-C. Chen, W. R. Legant, K. Wang, L. Shao, D. E. Milkie, M. W. Davidson, C. Janetopoulos, X. S. Wu, J. A. Hammer, Z. Liu, B. P. English, Y. Mimori-Kiyosue, D. P. Romero, A. T. Ritter, J. Lippincott-Schwartz, L. Fritz-Laylin, R. D. Mullins, D. M. Mitchell, J. N. Bembenek, A.-C. Reymann, R. Böhme, S. W. Grill, J. T. Wang, G. Seydoux, U. S. Tulu, D. P. Kiehart, and E. Betzig, "Lattice light-sheet microscopy: imaging molecules to embryos at high spatiotemporal resolution," Science **346**(6208), 1257998 (2014).
14. J. Bürgers, I. Pavlova, J. E. Rodriguez-Gatica, C. Henneberger, M. Oeller, J. A. Ruland, J. P. Siebrasse, U. Kubitscheck, and M. K. Schwarz, "Light-sheet fluorescence expansion microscopy: fast mapping of neural circuits at super resolution," Neurophotonics **6**(01), 1 (2019).
15. K. L. Ellefsen and I. Parker, "Dynamic Ca2+ imaging with a simplified lattice light-sheet microscope: A sideways view of subcellular Ca2+ puffs," Cell Calcium **71**, 34–44 (2018).
16. J. G. Ritter, R. Veith, J. P. Siebrasse, and U. Kubitscheck, "High-contrast single-particle tracking by selective focal plane illumination microscopy," Opt. Express **16**(10), 7142–7152 (2008).
17. A. Jain, A. H. J. Yang, and D. Erickson, "Gel-based optical waveguides with live cell encapsulation and integrated microfluidics," Opt. Lett. **37**(9), 1472–1474 (2012).
18. J. Schindelin, I. Arganda-Carreras, E. Frise, V. Kaynig, M. Longair, T. Pietzsch, S. Preibisch, C. Rueden, S. Saalfeld, B. Schmid, J.-Y. Tinevez, D. J. White, V. Hartenstein, K. Eliceiri, P. Tomancak, and A. Cardona, "Fiji: an open-source platform for biological-image analysis," Nat. Methods **9**(7), 676–682 (2012).
19. F. Chen, P. W. Tillberg, and E. S. Boyden, "Optical imaging. Expansion microscopy," Science **347**(6221), 543–548 (2015).
20. T. J. Chozinski, A. R. Halpern, H. Okawa, H.-J. Kim, G. J. Tremel, R. O. L. Wong, and J. C. Vaughan, "Expansion microscopy with conventional antibodies and fluorescent proteins," Nat. Methods **13**(6), 485–488 (2016).

A3. Third paper: Imaging three-dimensional brain organoid architecture from meso- to nanoscale across development

Reproduced with permission from

Rodriguez-Gatica, J. E., Iefremova, V., Sokhranyaeva, L., Yeung, Si Wah Christina Au, Breitkreuz, Y., Brüstle, O., Schwarz, M. K. and Kubitscheck, U. (**2022**). Imaging three-dimensional brain organoid architecture from meso- to nanoscale across development. Development 149.

DOI: https://doi.org/10.1242/dev.200439

Contributions

- Experimental design
- Sample preparation
- All data acquisition and analysis
- Writing the manuscript

© 2022. Published by The Company of Biologists Ltd | Development (2022) 149, dev200439. doi:10.1242/dev.200439

HUMAN DEVELOPMENT

TECHNIQUES AND RESOURCES ARTICLE

Imaging three-dimensional brain organoid architecture from meso- to nanoscale across development

Juan Eduardo Rodriguez-Gatica[1,‡], Vira Iefremova[2,*,‡], Liubov Sokhranyaeva[3], Si Wah Christina Au Yeung[2], Yannik Breitkreuz[4], Oliver Brüstle[2,4,§], Martin Karl Schwarz[3,4,§] and Ulrich Kubitscheck[1,§]

ABSTRACT

Organoids are stem cell-derived three-dimensional cultures offering a new avenue to model human development and disease. Brain organoids allow the study of various aspects of human brain development in the finest details *in vitro* in a tissue-like context. However, spatial relationships of subcellular structures, such as synaptic contacts between distant neurons, are hardly accessible by conventional light microscopy. This limitation can be overcome by systems that quickly image the entire organoid in three dimensions and in super-resolution. To that end we have developed a system combining tissue expansion and light-sheet fluorescence microscopy for imaging and quantifying diverse spatial parameters during organoid development. This technique enables zooming from a mesoscopic perspective into super-resolution within a single imaging session, thus revealing cellular and subcellular structural details in three spatial dimensions, including unequivocal delineation of mitotic cleavage planes as well as the alignment of pre- and postsynaptic proteins. We expect light-sheet fluorescence expansion microscopy to facilitate qualitative and quantitative assessment of organoids in developmental and disease-related studies.

KEY WORDS: Brain organoid, Expansion microscopy, Light-sheet fluorescence microscopy, Super-resolution, Synaptogenesis

INTRODUCTION

In recent years, advances in stem cell technologies have enabled rapid progress in the field of pluripotent stem cell-based 3D cultures such as brain organoids. These culture formats represent self-organizing structures that recapitulate certain aspects of *in vivo* brain development. They display complex structures that recapitulate several aspects of early neurogenesis, including the formation of an apical and basal surface, polarized neuroepithelium, neurogenic ventricular and outer radial glia (oRG), the formation of layered, cortex-like architectures and maturation to the level of synapse formation (Paşca et al., 2015; Lancaster et al., 2017). At the same time, proper visualization of these diverse processes in 3D has remained challenging, and most analyses of their cyto- and histoarchitecture are still based on conventional 2D histology of organoid cryosections. However, recently more sophisticated approaches for whole-organoid clearing and imaging that allow addressing the structural features in all three dimensions and preserving the 3D organization by avoiding cryosectioning were introduced and have shown rapid development (Adhya et al., 2021; Albanese et al., 2020; Edwards et al., 2020). Although several studies that employ whole-organoid clearing have been published in recent years, they mainly use small organoids, e.g. to assess early neural differentiation (Benito-Kwiecinski et al., 2021). A number of parameters remain rather challenging in the context of whole-mount analysis of larger organoids. This applies particularly to structures appearing at late stages of organoid differentiation, such as imaging of dendritic spines and synapses (Masselink et al., 2019; Dekkers et al., 2019; Albanese et al., 2020).

Parallel to the development of organoids, novel and fast large-volume imaging methods were introduced that are able to depict fine cellular and subcellular structural features within geometrically extended tissue samples in 3D. The ability to image large neuronal tissue fragments came into reach with the advent of light-sheet fluorescence microscopy (LSFM). This technique allows us to observe, with one or two microscope objective lenses, a fluorescently labeled specimen, the focal plane of which is illuminated perpendicular to the detection axis by a thin sheet of light (Huisken et al., 2004; Dodt et al., 2007). Thus, LSFM offers intrinsic optical sectioning, which can further be amended by confocal line detection (Silvestri et al., 2012; Baumgart and Kubitscheck, 2012) to yield optimal contrast in a scattering specimen. Substantial progress has been made in the past few years by using illumination beam shaping to achieve very thin light sheets to enhance optical resolution over large fields of view. Lattice light sheets (Chen et al., 2014; Ellefsen and Parker, 2018; Stockhausen et al., 2020), Airy beams (Vettenburg et al., 2014) or modifying the Gaussian light-sheet waist across the field of view (Dean et al., 2015; Fu et al., 2016; Neyra et al., 2020) have resulted in extra thin light-sheets with large extensions. Moving the specimen through the illuminating sheet within the detection plane of the imaging objective provides 3D image stacks. When using sensitive and fast CMOS cameras, image rates of hundreds of frames per second can be achieved, significantly decreasing the imaging time for large specimens compared with confocal laser scanning microscopy.

Optimal use of light-sheet microscopy requires the elimination of refractive index inhomogeneities in the probe by using an immersion medium with a refractive index matched to the cellular components of the probe. This can be accomplished by tissue clearing (for a review on different clearing procedures, see Ueda et al., 2020). Combining tissue clearing with LSFM allows effective optical resolutions in the

---

[1]Institute of Physical and Theoretical Chemistry, University of Bonn, Wegelerstr. 12, 53115 Bonn, Germany. [2]Institute of Reconstructive Neurobiology, University of Bonn Medical Faculty and University Hospital Bonn, Venusberg-Campus 1, 53127 Bonn, Germany. [3]Institute of Experimental Epileptology and Cognition Research (IEECR), University of Bonn Medical School, Sigmund-Freud-Str. 25, 53127 Bonn, Germany. [4]LIFE & BRAIN GmbH, Cellomics Unit, Venusberg-Campus 1, D-53127 Bonn, Germany.
*Present address: Department of Molecular and Cell Biology, University of California, 291 Weill Hall, Berkeley, CA 94720, USA.
‡These authors contributed equally to this work

§Authors for correspondence (brustle@uni-bonn.de; Martin.Schwarz@ukbonn.de; u.kubitscheck@uni-bonn.de)

O.B., 0000-0002-1277-0980; M.K.S., 0000-0002-5898-751X; U.K., 0000-0003-3750-5355

Handling Editor: Paola Arlotta
Received 6 December 2021; Accepted 28 June 2022

range of 0.3 µm laterally and 1.0 µm axially when using long-distance objective lenses for imaging with a numerical aperture (NA) of 1.0 or greater. Thus, LSFM is especially well suited for the fast analysis of complex arrangements of large cleared cell clusters and tissue fragments, where it enables, for example, fast light microscopic assessment of the complex 3D architecture of organoids (Albanese et al., 2020; Benito-Kwiecinski et al., 2021).

However, LSFM cannot reveal the very fine details of neuronal networks as these structures are well below the optical diffraction limit. To visualize synapses with spatial information conserved in a 3D human cerebral organoid, super-resolution imaging is necessary. Classical point scanning light microscopy in super-resolution is challenging and restricted to small regions (single synapses), making it virtually impossible to scan entire organoids or even distinct structures within organoids in 3D.

A solution to this issue came into reach with the development of light-sheet fluorescence expansion microscopy (LSFEM), which has enabled the analysis of extended neural circuits in super-resolution (Bürgers et al., 2019; Gao et al., 2019; Schwarz and Kubitscheck, 2021). As in standard expansion microscopy (ExM; Chen et al., 2015; Ku et al., 2016; Tillberg et al., 2016; Chozinski et al., 2016), LSFEM uses water-absorbent polymers to physically expand enzymatically treated tissue samples. Before synthesizing the expandable polymer within the fixed-tissue sample, proteins of interest are labeled with fluorescent antibodies that bind the antigen of interest. The tissue is then partially digested to allow subsequent expansion of the polymer matrix containing the fluorescent labels. As a result of expansion, fluorescent moieties spaced closer than the optical diffraction limit (∼250 nm) can be optically resolved, resulting in effective super-resolution images of organoids. Using LSFEM, we were able to rapidly image extended neuronal circuits in effective super-resolution (Bürgers et al., 2019).

Here, we present a novel brain organoid analysis pipeline, which employs LSFM and LSFEM to image entire brain organoids in 3D during different developmental stages. The methods allow us to zoom in and out on an entire single organoid from meso- to nanoscale optical resolution in order to obtain a comprehensive view of both the brain organoid architecture and subcellular aspects. Careful sample preparation allowed the conservation of fluorescent proteins, which are frequently used to label e.g. neuronal subpopulations. Using effective super-resolution imaging, the finest details of neuronal network parameters within a larger context can be depicted succeeding, for the first time, in identifying clusters of synaptically connected neurons in the context of an entire cleared mature brain organoid.

RESULTS

Clearing, physical expansion and LFSM enable the analysis of mature brain organoids

Fixed brain organoids represent opaque structures. We developed specific sample preparation techniques and imaging approaches to exploit the inherent information optimally. To assess the applicability of our approach to different organoid protocols, we have used two different protocols in our study: a classic ‘organoid’ protocol adapted from Lancaster et al. (2013), and a protocol adapted from Pasça et al. (2015), who term their structures ‘spheroids’. However, the distinction into ‘organoids’ and ‘spheroids’ is somewhat arbitrary, because both are based on self-organized architecture formation. For that reason, we uniformly refer to these structures as ‘organoids’. We have applied our LSFEM approach to both protocols, which we refer to as protocol I and II (for details, see Materials and Methods), to ensure broad applicability.

Following fixation, we permeabilized the organoid tissue using CHAPS instead of Triton X, following a procedure suggested by Zhao and coworkers (Zhao et al., 2020). This enabled especially the preservation of the activity of autofluorescent proteins and staining of complete large organoids using commercial antibodies with high efficiency (see Fig. S1). We usually employ DNA staining to mark all cell nuclei and also include markers for specific cell types or cellular structures highlighting specific types of neurons or subcellular neuronal structures. To allow a light microscopic analysis of these samples, optical clearing is mandatory (Fig. 1A). Therefore, the first steps of ExM include the addition of bifunctional linker coupling protein residues, thereby creating a polyacrylamide gel within the organoid, which keeps the fluorescently labeled structures in place. Digestion by proteinase K renders the sample transparent. Keeping the sample in a buffered aqueous immersion medium such as PBS induces a 1.5-fold expansion (Fig. 1B), whereas the exchange of the medium to bi-distilled water results in an approximately 4-fold physical expansion (Fig. 1C). In either state, the sample can be analyzed using LSFM (Fig. 1D). We performed extensive controls demonstrating that the overall organoid structure was not distorted during the clearing process (Fig. S2). Labeling the tight junctions (ZO1) and the progenitor cells (SOX2) using respective antibodies yielded identical structures. In this comparison it was evident that the clearing process greatly improved contrast and overall image quality. The opaque nature of uncleared organoids prevented imaging of structures located inside the organoids.

LSFM enables analysis of brain organoid structures across development and cell differentiation

Tracing subpopulations of fluorophore-labeled cells

Mesoscale imaging of cleared brain organoids allowed us to follow organoid development from generation until maturation. The key steps of the pipeline for organoid sample preparation and imaging are shown in Fig. 1E, and the various approaches to imaging are summarized in Table 1. Cerebral organoids can reach up to several millimeters in diameter. To cover such dimensions, light-sheet imaging was performed using a low magnification objective lens (10×) with a relatively low NA (0.3) in order to achieve a large field of view for covering the complete organoid with a limited number of mosaic tiles (Fig. 1F,G).

We employed mixed organoids containing 10% EGFP-expressing cells [90% induced pluripotent stem cells (iPSCs) mixed with 10% doxycycline-inducible EGFP-labeled iPSCs from the same genetic background prior to seeding them] and with all cell nuclei labeled by Hoechst. Use of our optimized sample preparation protocol (Bürgers et al., 2019; Stockhausen et al., 2020) allowed us to maintain the fluorescence of autofluorescent proteins, e.g. EGFP, by first optimizing the permeabilization of the sample and then the digestion conditions and the expansion buffer, which avoided the necessity of antibody staining in this case. One month after the generation of the organoid, the distribution of the EGFP cells was found to be not uniform throughout the volume, as could be concluded from 2D images (Fig. 2A-D). Rather, the labeled cells tended to form large clusters. Interestingly, such clusters of EGFP-labeled cells still existed after 14 months. We suspect that the non-uniform distribution of EGFP-positive cells was due to local proliferation of subpopulations of these cells (Fig. 2E-G).

LSFM and LSFEM allow meso- to nanoscale analysis in a single sample

The functional architecture of brain organoids extends over lengths ranging from more than a centimeter to nanometers, and we became

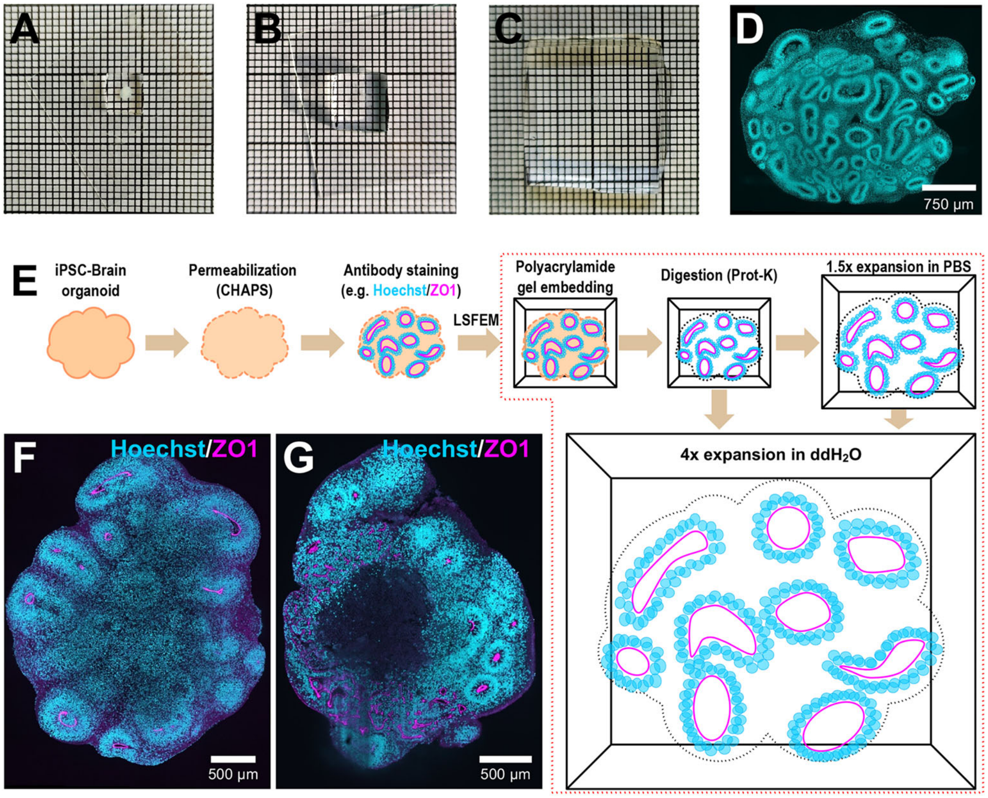

Fig. 1. Organoid sample preparation for LSFEM. (A) Two-month-old brain organoid embedded in a polyacrylamide gel. (B) Two-month-old organoid after proteinase K digestion, which resulted in a clearing of the organoid and an ∼1.5-fold expansion. (C) The same organoid after expansion in bi-distilled water, which yielded an ∼4-fold expansion. (D) Optical section of the cleared and 1.5-fold expanded organoid showing the cell nuclei of an optical section in a depth of 1.2 mm. (E) Pipeline for organoid sample preparation. After fixation of the 3D samples, a permeabilization step is made using a detergent (CHAPS), which is a key step to allow proper whole-body immunostaining of the organoid. Subsequently, immunostaining for identifying specific cell types or structures, along with a nuclear staining, is performed. In the diagram, the tight junction marker ZO1 (magenta) and nuclear staining Hoechst (cyan), are used as example. After immunostaining the sample is embedded in and chemically linked to a polyacrylamide gel. A digestion of the sample using a buffer containing proteinase K (Prot-K) renders the sample transparent, resulting in optimal conditions for light-sheet imaging. Placing the sample after digestion in PBS leads to an isotropic expansion of 1.5-fold (corresponding to B), while placing the digested sample in bi-distilled water leads to a 4-fold expansion (corresponding to C), allowing for the analysis of the whole organoid in super-resolution. (F,G) Optical sections of a 3-month-old brain organoid prepared according to protocol II (F) and a 2-month-old brain organoid prepared according to protocol I (G) are shown as examples. Both are stained against Hoechst and ZO1.

interested in devising an approach that enables recording across these ranges. Cleared and 1.5-fold-expanded complete brain organoids were imaged using a 10× objective lens (Figs 2 and 3A,B). The use of 4-fold expansion, a 1.1 NA objective lens for imaging, an axial step size of 0.3 µm and subsequent deconvolution allowed visualization of selected sample regions at the 100 nm scale (Fig. 3C). Numerous cell somata and neurites with extensions up to hundreds of micrometers were visible and traceable. Close examination of magnified sample regions revealed numerous spine-like structures, suggesting advanced differentiation and formation of neuronal connections (Fig. 3D-F).

Table 1. Imaging brain organoids at various scales with different combinations of the physical sample expansion and specific objectives lenses

LSFEM imaging of brain organoids		
Mesoscale (1.5-fold exp+low mag/NA)	Microscale (1.5-fold exp+high mag/NA)	Nanoscale (4-fold exp+high mag/NA)
ROI – whole organoid: organoid volume; surface area; rosette distribution	ROI – rosettes: cleavage planes; TBR2$^+$ cells/oRGs	ROI – neural projections: neurites and spines; synapses

An example of a region of interest (ROI) is given for each case, followed below by possible corresponding image analysis parameters. Imaging specific ROIs is especially relevant for the micro- and nanoscale owing to the large amount of data that could be generated. exp, expansion; mag, magnification.

Qualitative and quantitative assessment of neuroepithelial architectures

Our approach enables detailed insights into the cellular architecture of brain organoids, because numerous structural parameters may be evaluated. This also allows quantitative analyses, as we demonstrate here using neuroepithelial rosettes as example. Structural analyses can be improved even more when exploiting the fact that antibodies generally penetrate expanded tissue particularly well (Edwards et al., 2020).

These structures typically appear in cerebral organoids, forming ventricular zone (VZ)-like areas, the apical surface of which can be labeled with antibodies to the tight junction protein zonula occludens protein 1 (ZO1, also known as TJP1). ZO1 immunofluorescence thus enables the evaluation of the topology of neuroepithelial rosettes and the ventricle-like space they could enclose (Fig. 4A,B). Fig. 4C shows the cropped apical surface across the whole organoid, demonstrating that these structures exhibit a large variation in size and shape. Some were closed

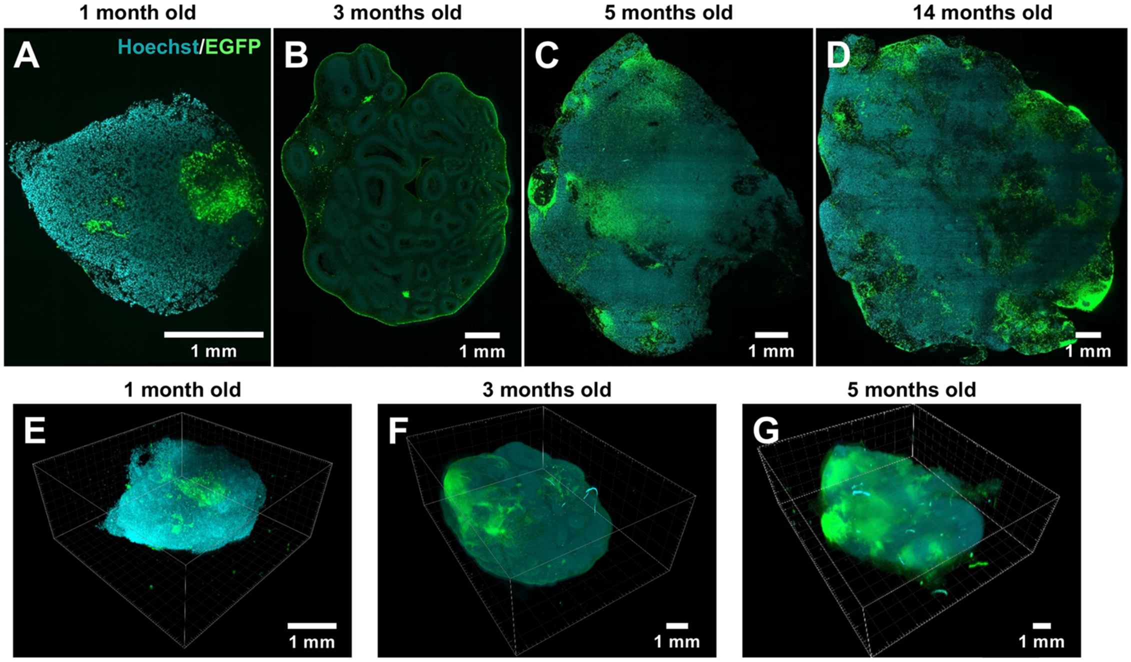

Fig. 2. Development of chimeric brain organoids containing 10% EGFP-expressing cells across a time span of 14 months. (A-D) LSFM of cleared and 1.5-fold expanded brain organoids with cell nuclear staining containing 10% EGFP-expressing cells (green) and nuclei stained with Hoechst (cyan) after 1 month (A), 3 months (B), 5 months (C) and 14 months (D). All organoids were prepared according to protocol I. The shown optical sections were taken at 646 µm, 1140 µm, 1830 µm and 1119 µm depth, respectively. Image sizes were 3.6×3.6 mm^2, 8.6×11.7 mm^2, 13.1×14.9 mm^2, and 16.6×17.3 mm^2, respectively. 3D view of the 1-month-old (E), 3-month-old (F) and 5-month-old (G) brain organoids. The imaged volumes corresponded to 3.6×3.6×1.6 mm^3, 8.6×11.7×4.4 mm^3 and 13.1×14.9×5.2 mm^3, respectively. The Hoechst channel of Fig. 2B was shown in Fig. 1D to illustrate the expansion process.

structures, i.e. enclosing a ventricle-like lumen; others appeared to be relatively flat with complex geometry and a sheet-like topology. Therefore, the measurement of the apical surface of the neuroepithelium appeared to be an appropriate parameter for their characterization. The surface size distribution of the segmented structures of the organoid shown in Fig. 4A is displayed in Fig. 4C.

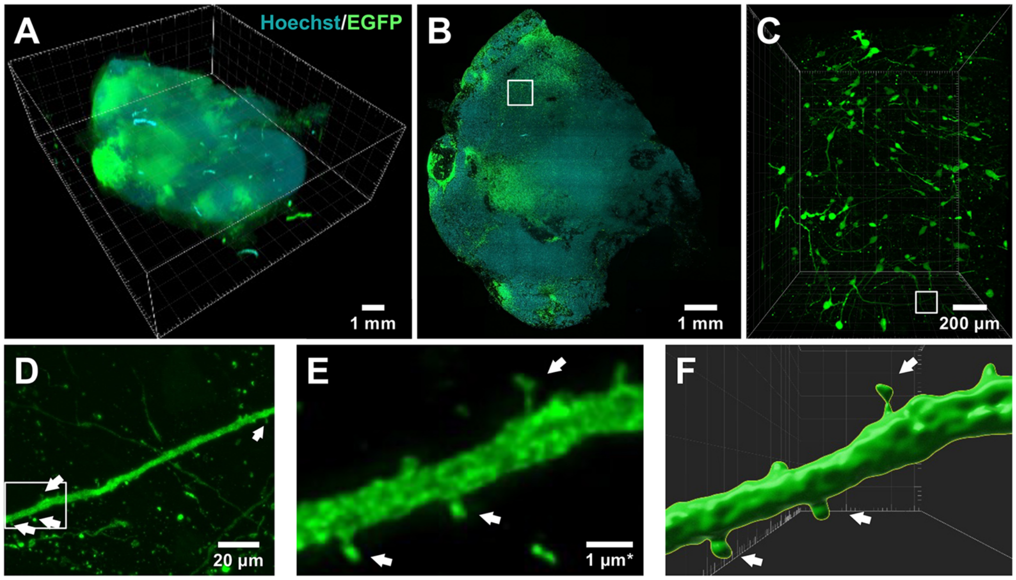

Fig. 3. Five-month-old brain organoid (protocol I) containing GFP-positive cells imaged from the cm to the nm scale. (A) 3D view, volume 13.1×14.9×5.2 mm^3. (B) Optical slice at a depth of 1.8 mm. The image was obtained using a 10× NA 0.3 objective lens and was also used in Fig. 2C as part of the series showing organoid development over time. Size 13.1×14.9 mm^2. (C) Rendering of a 3D stack with a volume of 1248×1548×1275 µm^3 as marked in B (white box). The image was obtained using a 25× NA 1.1 objective lens in the same sample after a 4-fold expansion. (D) Magnification of the boxed region marked in C, 185×132 µm^2, revealing spine-like structures (arrows). (E) Magnification of the boxed region marked in D. The adjusted scale bar 1 µm* considered the 4-fold expansion and physically corresponded to 4 µm. (F) Surface rendering of the neural projection revealed spine-like structures. For C-E the shown image data were deconvolved. In total, 35 image stacks covering a total specimen region of 1248×1548 µm^2 with a total depth of 1275 µm^3, which was covered at an axial step size of 0.3 µm, were acquired from this organoid.

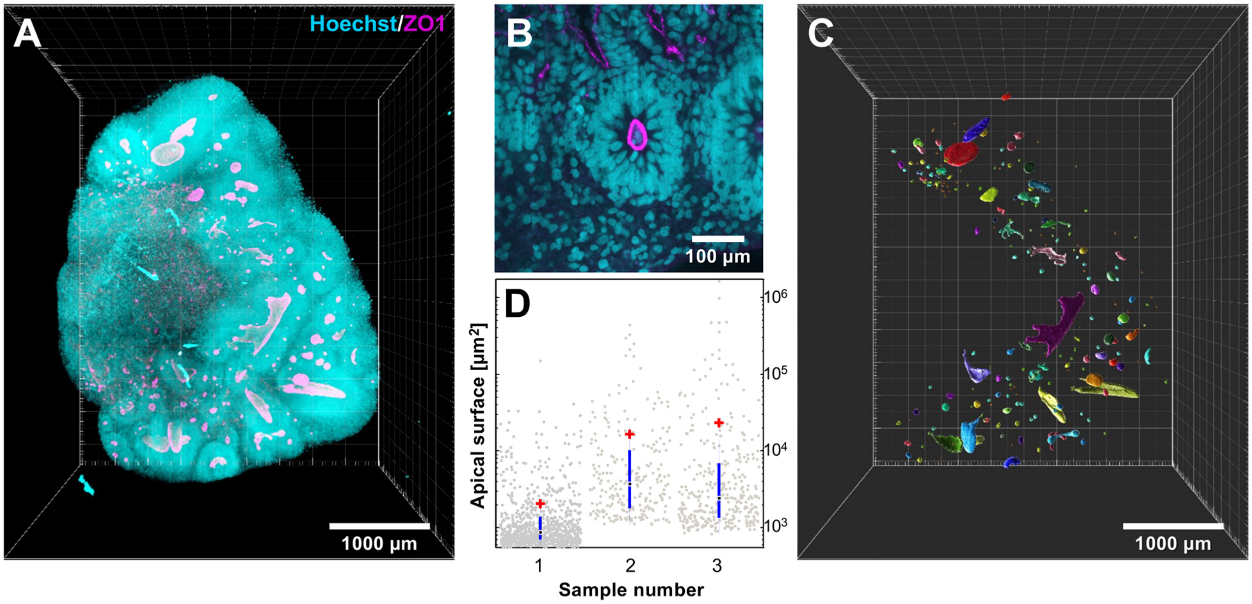

Fig. 4. Labeling of the apical surface of neuroepithelial structures in a 2-month-old brain organoid with an antibody against ZO1 (see Movie 1). Three different 2-month-old organoids were imaged and evaluated to obtain the quantitative parameters as given below. All organoids were prepared according to protocol I and measured in PBS. (A) Cell nuclei (Hoechst, cyan) and ZO1 (magenta). The cyan fluorescent cell nuclei indicate the rough shape of the organoid. In this way, the total organoid volume $(1.36\pm0.55)\times10^{10}$ µm^3 and the total surface area of $(1.2\pm0.6)\times10^8$ µm^2 was obtained. (B) Magnification of an optical section at a depth of 1 mm showing a closed apical surface revealing a VZ-like lumen inside a rosette. Considering that each rosette contains one apical surface, the average number of rosettes within the three whole organoids was evaluated yielding 485±270 rosettes. (C) Cropped apical surfaces of the neuroepithelium inside the organoid shown in A. Color labeling according to surface area, randomly generated. (D) The distribution of the apical surface areas of the three different 2-month-old organoids appears as an appropriate parameter for their characterization, as not all structures enclose a volume. Mean values are indicated by the red cross. Blue lines represent quartiles. Black dots show median values. The overall mean is $1.66\pm4.79\times10^4$ µm^2 and the median is 3710 µm^2.

Data like that shown in Fig. 4C allowed the quantification of numerous parameters (Table 1), e.g. characterizing the apical surface topology (Fig. 4D). Mesoscale parameters were quantified by imaging three different 2-month-old organoids.

Delineation of neural subpopulations

The combination of antibody staining and LSFEM allows straightforward detection of neural subpopulations. As an example, we used co-labeling with antibodies to SOX2 and TBR2 (EOMES), which can, for example, delineate oRG cells, a distinct population of neuronal progenitors in the developing human brain, which are located in the outer subventricular zone (oSVZ). These cells are essential for neurogenesis and expansion of the human cortex (Bershteyn et al., 2017). ORGs are characterized by expressing SOX2, but not TBR2, in the outer region of the VZ (see green arrows in Fig. 5A-C).

However, only identifying SOX2-positive cells and their position is not sufficient for an unequivocal delineation and quantification of oRGs (Pollen et al., 2019). Recent studies have revealed that the vast majority of cells expressing HOPX also expressed the radial glia marker SOX2, but not the intermediate progenitor marker TBR2 (Bhaduri et al., 2020; Pollen et al., 2019). Thus, HOPX is considered a useful marker for oRGs, and we applied it in 3-month-old organoids. In Fig. 6, we show several examples for the identification of oRGs in different samples. Co-staining with an antibody to N-cadherin enabled the delineation of the apical surface of the neuroepithelium and thus a spatial relationship of the HOPX-positive cells to the histoarchitecture (Fig. 6C,D).

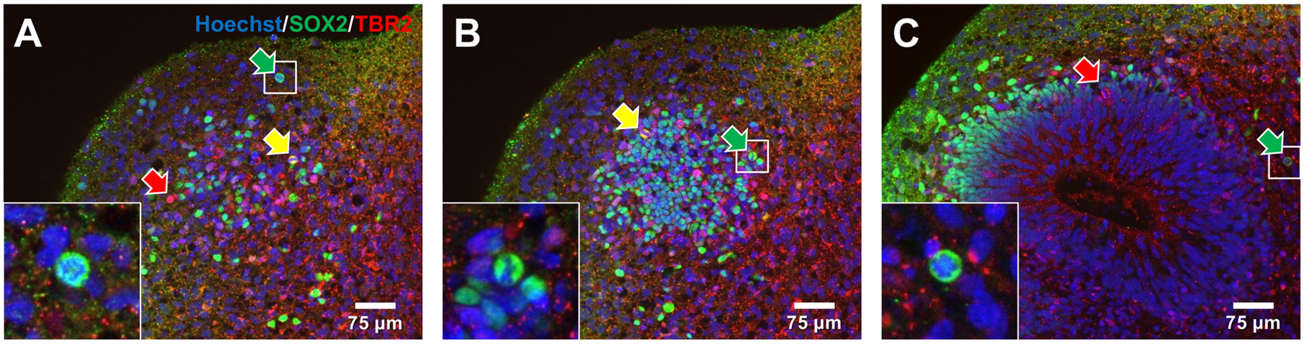

Fig. 5. Identification of different types of cortical progenitor cells (oRGs) using double labeling with antibodies to SOX2 (green) and TBR2 (red) in a 2-month-old organoid (protocol I) in PBS counterstained with Hoechst (blue). (A-C) Single optical slices taken at depths of 53 µm (A), 75 µm (B) and 146 µm (C) of the same sample. Cells being TBR2-positive but SOX2-negative (red arrows), both TBR2- and SOX2-positive (yellow arrows) and TBR2-negative but SOX2-positive (green arrows) were marked. TBR$^-$/SOX2$^+$ cells in such a basal location are indicative of oRGs (Pollen et al., 2019). Total area: 703×651 µm^2. Insets show magnification of boxed areas.

Development (2022) 149, dev200439. doi:10.1242/dev.200439

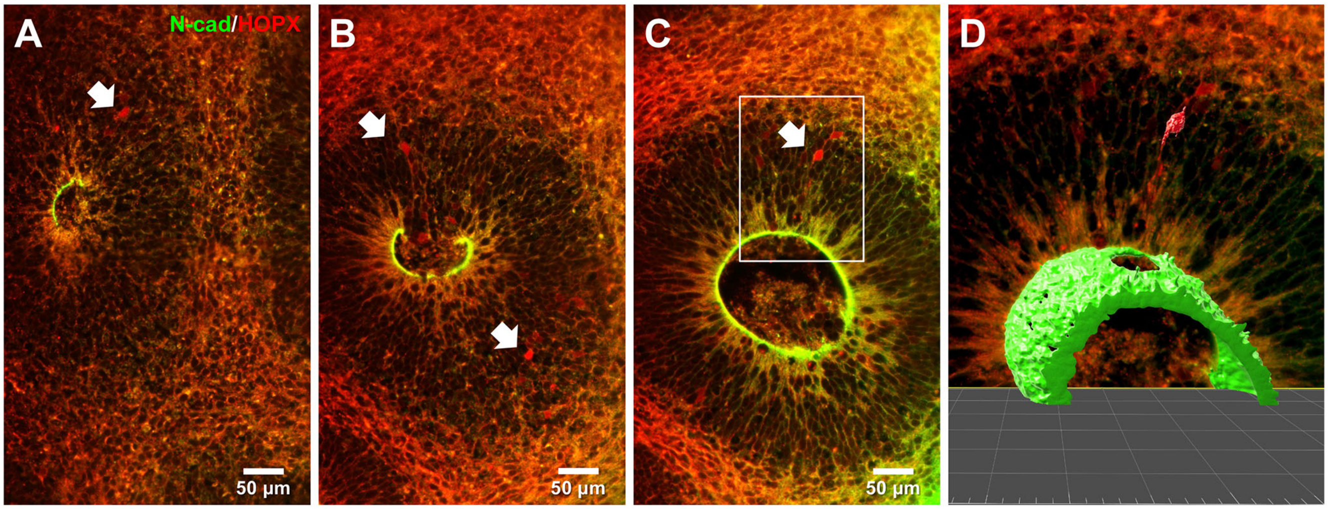

Fig. 6. Definition of the 3D location of oRGs with regard to the VZ surface. (A-C) Three-month-old brain organoid labeled by N-cadherin (N-cad, green) and HOPX (red), with oRGs marked by white arrows. The organoid was prepared according to protocol I and measured in PBS. A-C show maximum intensity projection of 3 µm of optical sections at a depth of 200, 452 and 595 µm, respectively. (D) Surface rendering of oRG and VZ as marked in C.

Imaging of subcellular structures

Orientation of mitotic cleavage planes

A key parameter in neurogenesis during human brain development is the orientation of mitotic cleavage planes of neuronal progenitors with regard to the apical surface of the neuroepithelium (Fig. 7A). The orientation of the mitotic spindle modulates the orientation of the cleavage plane and, therefore, the position of the two daughter cells. The correct spindle orientation during the early stages of human corticogenesis is vital for accomplishing the right ratio between symmetric and asymmetric cell divisions. Most actively dividing neuronal progenitors during early cortical development exhibit a horizontal orientation (i.e. an angle of 0 to 30°) in relation to the ventricular surface cleavage plane, which leads to expansion of the cortical progenitor pool via symmetric cell division. Vertical (60 to 90°) and oblique (30 to 60°) mitotic cleavage planes start to become more predominant immediately before neurogenesis (LaMonica et al., 2013; Yingling et al., 2008). This asymmetric mode of cell division results in the generation of two different daughter cells and leads to an increase in neuronal differentiation. Several studies have shown that a disrupted orientation of the

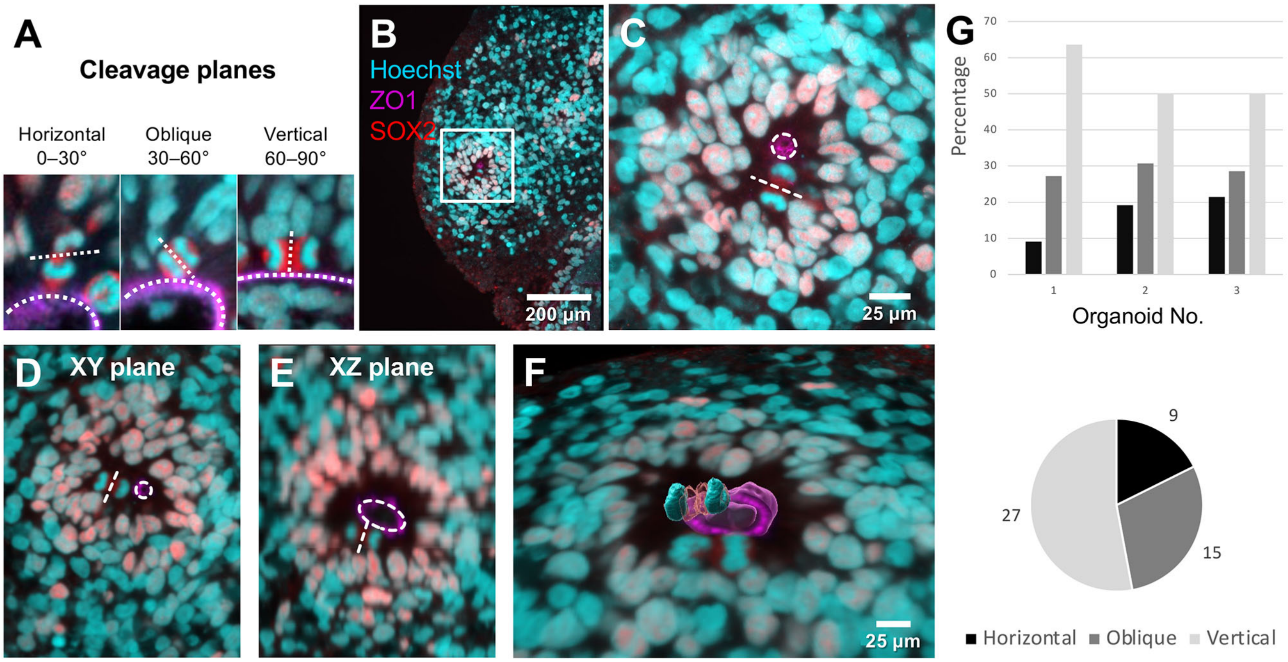

Fig. 7. Analysis of cleavage planes. (A) Definition of cleavage planes with regard to the apical VZ lumen surface. (B) A 2-month-old brain organoid (protocol I) was labeled by ZO1 (magenta), SOX2 (red) and Hoechst (cyan). ZO1 revealed the surface of a VZ lumen. Total area: 703×651 µm^2. (C) Magnification of the boxed region marked in B. The orientation of the cleavage plane of a mitotic cell (dashed line) in relation to the lumen surface could be visualized. Dashed circles in A,C-E depict the apical surface of the neural rosettes. Total area: 277×277 µm^2. (D,E) Using only 2D data may lead to a misinterpretation of the cleavage plane orientation. (F) The true cleavage plane orientation can only be deduced from 3D data (Movie 2). (G) Quantification of the orientation of cleavage planes in three different 2-month-old organoids derived from the 3D data. Lower graph, fractions and sum of respective numbers.

mitotic cleavage planes led to abnormal corticogenesis, reflected in various developmental phenotypes. Lancaster and colleagues performed one of the first landmark studies showing a crucial role of the shift in mitotic cleavage plane orientation and its effect on the development of microcephaly (Lancaster et al., 2013). In two more-recent studies using Miller-Dieker syndrome patient-derived organoids in comparison with controls, they have successfully shown that, under disease conditions, there is a clear shift from the vertical to the horizontal plane of cell division of radial glia without a significant increase in oblique planes, causing early neurogenesis and smaller size of patient-derived 3D cortical cultures (Bershteyn et al., 2017; Iefremova et al., 2017).

We found the combination of DNA staining by Hoechst and immunofluorescence staining for ZO1 and the neural progenitor marker SOX2 suitable for delineating the orientation of cleavage planes with respect to the surface of the neuroepithelium (Fig. 7B,C). Importantly, our image analyses revealed that it is not always possible to assess the orientation of the cleavage plane with regard to the apical surface using 2D projections alone. As shown in Fig. 7D, the *xy*-section suggested a horizontal orientation of the cleavage plane of the mitotic cell with regard to the apical surface, whereas the *xz*-section of the very same cell nucleus indicated a vertical orientation (Fig. 7E). The evaluation of the true orientation requires the full 3D view (Fig. 7F). This was performed for three different 2-month-old brain organoids. The results are shown in Fig. 7G. From the performed analysis, it can be concluded that the majority (53%) of diving cells along the ventricle-like structure exhibit a vertical cleavage plane orientation, which is in line with previously reported data from early stages of cortical organoid cultures (Bershteyn et al., 2017; Iefremova et al., 2017).

Detection and spatial relationship of pre- and postsynaptic structures

The existence of functional neuronal connections in cerebral organoids has been reported previously (Paşca et al., 2015; Quadrato et al., 2017; Giandomenico et al., 2019). However, there are no reported studies using whole cleared organoids showing the co-existence of both pre- and postsynaptic proteins at synapses in a spatial manner (for a review of current organoid imaging, see Brémond Martin et al., 2021). We used again chimeric organoids generated with 10% EGFP-containing cells for such structures. Fig. 8 shows a 14-month-old organoid with a diameter of ∼1.5 cm (Fig. 8A). Regions near the surface of the organoid contained numerous cells with neuronal morphology and long neurites (Fig. 8B). LSFEM with antibodies to the presynaptic protein synapsin1 (SYN1) and the postsynaptic protein HOMER1 revealed diffraction-limited spots within distances of 150±61 nm (mean±s.d.; n=26), with a median value of 130 nm of each other along with neural projections (Fig. 8C-F). In this very same organoid, we determined the number of spines on three different

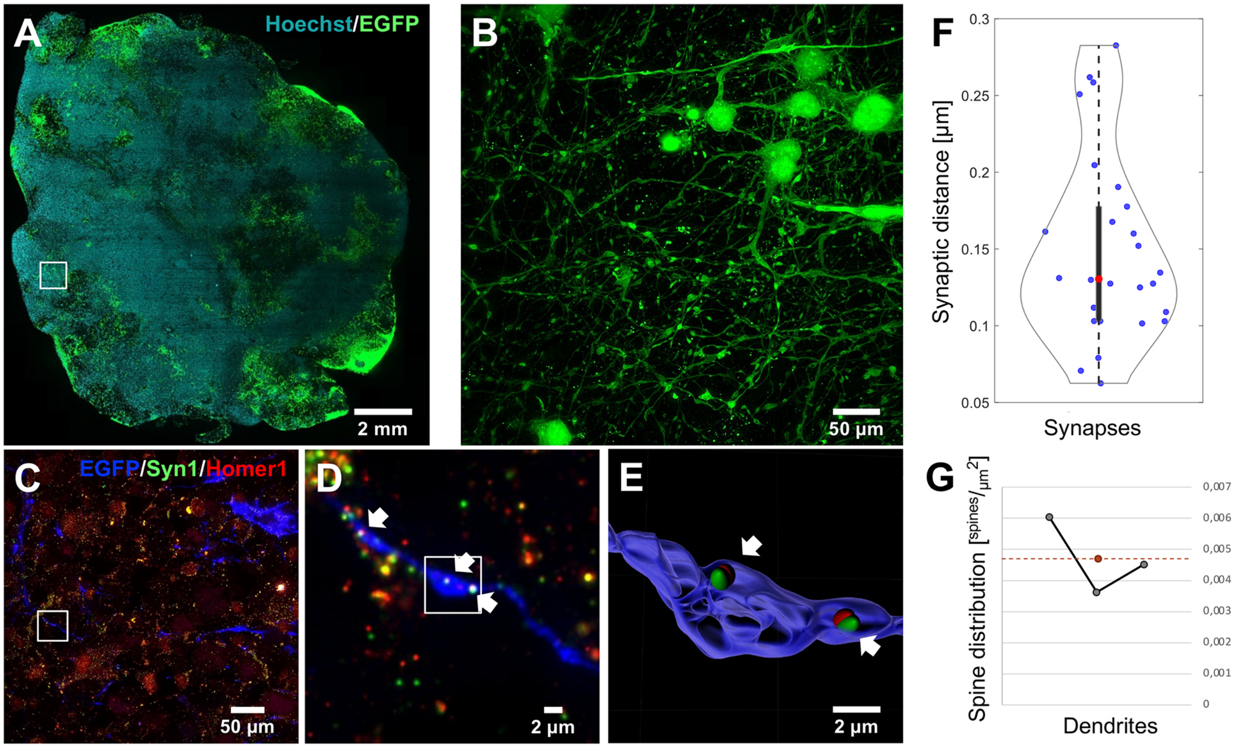

Fig. 8. Pre- and postsynaptic structures in a 14-month-old brain organoid prepared according to protocol I. (A-G) The organoid contained 10% EGFP-expressing cells and was labeled by Hoechst and stained with antibodies to the pre- and postsynaptic proteins synapsin 1 (SYN1, green) and HOMER1 (red). For details, see Movie 3. (A) Optical slice at a depth of 1.5 mm. This image was constructed using 285 single image tiles, which were acquired using a 10× NA 0.3 water immersion objective, and was also used in Fig. 2D as part of the series showing organoid development over time. Size 16.6×17.3 mm^2. (B) Maximum intensity projection comprising 1000 images (about 300 µm in the axial direction) acquired with a 25× NA 1.1 objective, size 547×547 µm^2, after expanding the sample 4-fold and after deconvolution. (C) Maximum intensity projection comprising 20 images (about 300 µm in axial direction). Here, EGFP is shown in blue and the pre- and postsynaptic proteins SYN1 and HOMER1 are shown in green and red, respectively. (D) Magnification of the boxed region in C, revealing the colocalization of pre- and postsynaptic proteins SYN1 and HOMER1 along axonal boutons. Arrows indicate the synapses along neurites. (E) 3D reconstruction of the multi-synaptic bouton shown in boxed area in D. (F) Violin plot of the determined distances between pre- and postsynaptic markers (blue dots) analyzed in 3D. The red dot shows the median, the black lines the quartiles and the dashed line the upper and lower whiskers. (G) Spine densities for three different dendrites. Mean density is marked in red and corresponds to an average value of one spine every 212 µm^2 (0.0047 spines/µm^2).

dendrite segments. For that purpose, the expanded organoid was labeled by antibodies against MAP2. We determined spine densities of 0.06, 0.036 and 0.045 spines per µm^2 on dendritic segments with lengths of 269, 187 and 175 µm lengths, respectively. This means that we could find one dendritic spine for every 212 µm^2 on average. Considering the above demonstration of the existence of pre- and postsynaptic structures, these values show that the 14-month-old organoid exhibited well-developed and abundant neuronal connections. Thus, using LSFEM spine structures (Fig. 3D-F) and synaptic structures (Fig. 8D,E) can be detected in complete 3D organoids without the need for physical cutting of the sample.

DISCUSSION

Cerebral organoids are opaque 3D structures with a size in the range of a few millimeters. Opacity and volume make light microscopic analysis difficult because the opacity impedes classical imaging with sufficient contrast and the organoid size prohibits the use of high-resolution optical microscopy. The latter requires objectives with a high NA, which generally have very short working distances. Classical imaging approaches using organoid slices miss the natural 3D features of such complex samples.

Here, we demonstrate the potential of LSFM combined with a clearing and expansion of organoids by a factor of 1.5- to 4-fold, which has also recently been used for the examination of mouse brain sections (LSFEM; Bürgers et al., 2019; Gao et al., 2019; Stockhausen et al., 2020). We demonstrate that this approach allows detailed analysis of organoids up to 15 mm diameter.

The preservation of the fluorescence of autofluorescent proteins during the expansion procedure enabled us to follow the location and fate of selected cell types during the course of development over a time period of up to 14 months. The use of a fraction of cells expressing fluorescent proteins when generating the organoids, in addition to nuclear staining, allowed a deeper analysis of the location and distribution of cells groups within the volume. Thereby, we confirmed the well-known observation that the development of organoids varied largely due to the batch-to-batch variability (Quadrato et al., 2016, 2017; Qian et al., 2019; Velasco et al., 2019).

Imaging across scales

The crucial details of neuronal connectivity occur on length ranges of ∼100 nm. Such small structures can optically only be resolved using super-resolution light microscopy. We have already demonstrated that LSFEM can yield effective super-resolution laterally down to less than 100 nm and axially down to 300 nm. Thereby, individual synaptic connections can be identified (Bürgers et al., 2019). Achieving this requires clearing followed by an expansion of the sample by a factor of four and subsequent high-resolution imaging. Further improvement of image resolution may be achieved by deconvolution techniques. This approach allowed us to detect single spine-like structures in a 5-month-old brain organoid. Usually, imaging at such a high resolution is feasible but not applicable for large sections of organoids due to the immense amount of data produced. An organoid of 1 mm^3 original size would yield an object of 64 mm^3 size after expansion. Imaging that structure at a resolution of 100 nm laterally and 300 nm axially at 16 bit, considering the Nyquist theorem, would yield a dataset of 340 TB. Current data processing workstations are at or beyond their computational limit when handling such amounts of data. Therefore, imaging at a mesoscopic scale is used to locate specific regions, for which super-resolution data can be obtained. Notably, this allows examining a single specimen on length ranges from 1 cm to 100 nm, corresponding to five orders of magnitude.

Mesoscale

A hallmark of developing cerebral organoids is the generation of rosette-forming neuroepithelial structures with an apical-basal polarity. The space enclosed by these structures has been shown to form a ventricle-like system, which can span across large volumes of the organoid (Di Lullo and Kriegstein, 2017). As these areas correspond to a pendant of the neurogenic ventricular zone *in vivo*, their qualitative and quantitative assessment is of great importance. The study of these structures was straightforward using LSFEM because they are immediately visible in the 3D data we acquired. The lumina of VZs could well be visualized and analyzed using additional staining against ZO1 or N-cadherin.

Microscale

A further determinant of brain organoid structure are oRGs. These cells can be stained using antibodies against TBR2, SOX2 and HOPX (Pollen et al., 2019). The identification of oRGs is generally challenging because of the low abundance of this cell type in brain organoids. Therefore, it is even more problematic if only 2D sections are employed because the mapped volume is quite small. The use of the complete 3D image stack clearly improved the chance of detecting this important cell type. For the success of these experiments and to achieve labeling with high contrast it was especially important to employ a new permeabilization strategy before labeling, namely to use CHAPS instead of Triton X (Zhao et al., 2020). This approach yielded a much better penetration of antibodies to their target sites inside the mature, rather large, organoids.

The orientation of cleavage planes of dividing cells with regard to the VZ surface is important for the growth properties of a brain organoid. We noted that evaluating the 3D data revealed the correct orientation of cleavage planes with regard to the lumen surface – use of 3D data avoided possible misinterpretations compared with using only 2D optical sections. Furthermore, we noticed that the use of SOX2 is sufficient to visualize the orientation of cleavage planes with our method, without the need for specialized antibodies such as phospho-vimentin.

Nanoscale

Clearly, LSFEM cannot compete with electron microscopy in terms of resolution and detection of fine structural details of specimen. However, in contrast to electron microscopy, LSFEM is compatible with multicolor fluorescence imaging, thus enabling molecular contrast for diverse neuronal populations and nanoscale resolution within a single large-tissue preparation. We performed triple color staining of a brain organoid using EGFP and pre- and postsynaptic markers in order to identify synapses unambiguously. Using LSFEM, we succeeded for the first time to detect both presynaptic synapsin 1 and postsynaptic HOMER1 within distances of 150 nm of each other along with neural projections, clearly proving the existence of synapses in a 14-month-old organoid by light microscopic means. The capability of imaging across many length ranges allows, for example, to count and analyze the spatial distribution of synapses in certain brain areas. In principle, our technique provides a sufficient optical resolution to allow the identification of different kinds of spines, e.g. mushroom spines or stubby spines, in 3D. In the future, for such experiments, it would be helpful to label dendritic structures using MAP2.

Clearly, LSFEM has specific limitations. An obvious one is the anisotropic optical resolution. Generally, the axial resolution is about 3-fold lower than the lateral resolution. Approaches to reduce that difference exist, but they do not function at the ultimate resolution limit. Furthermore, it is not simple to examine a specimen of arbitrary size with very high resolution. One reason is that the penetration time of antibodies into a spatially extended specimen increases nonlinearly with sample thickness. Thus, it is not trivial to achieve homogeneous staining of large samples. Also, very thick specimens present a problem, because the working distance of high resolution imaging objective lenses is limited.

In summary, we demonstrated that the combination of LSFM and ExM – LFSEM – allows imaging of mature brain organoids *in toto* down to synaptic resolution in a single imaging session, when they are combined with careful specimen preparation that preserves autofluorescent proteins and optimization of imaging results using deconvolution. The situation may be further improved when exploiting the fact that antibodies penetrate expanded tissue particularly well (Edwards et al., 2020). Thus, LSFEM is optimally suited for the analysis of brain organoid development.

MATERIALS AND METHODS

Pluripotent stem cell culture

Human IPSCs used in these experiments are cell line iLB-C-133bm-s4 (hPSCreg name UKBi013-A) and cell line iLB-C-133bm-s4 AAVS1-GFP (hPSCreg name UKBi013-A-1). Cells were maintained in six-well tissue culture plates (Nunc) coated with 1% Geltrex membrane matrix (Thermo Fisher Scientific) in StemMACS iPS-Brew (Miltenyi Biotec) with regular passaging using EDTA/PBS. Cultures were tested for mycoplasma contamination and were maintained mycoplasma free.

Generation of iPSC-derived 3D organoids

Protocol I

Organoids were generated along previously established protocol with slight modifications (Iefremova et al., 2017). In brief: on day 0 of organoid culture, iPSCs were dissociated into single-cell suspension using TrypLE Express (Gibco), followed by plating 18,000 cells in each well of an ultra-low-attachment round-bottom 96-well plate in StemFlex medium (Gibco) with 50 µM of ROCK inhibitor Y-27632 (10 µM, Hiss Diagnostics). In order to visualize the EGFP-positive cells, iPSCs from the same genetic background with and without doxycycline-inducible EGFP construct were mixed in the ratio 10/90, respectively. Organoids were fed every other day for up to 5 days with StemFlex media and then transferred to low-adhesion 6 cm plates in the neural induction medium containing 50% Neurobasal, 50% DMEM/F12 supplemented with 1× N-2 supplement, B-27 supplement (all Gibco) and glucose (0.4 mg/ml, Carl Roth). Neural induction medium was supplemented with 1% Minimum Essential Medium, non-essential amino acids solution (MEM-NEAA, Gibco), 1% GlutaMax, LDN-193189 (180 nM, Axon Medchem), A8301 (500 nM, Miltenyi Biotec) and XAV939 (10 µg/ml, Enzo Life Sciences) before medium change. After 5-6 days, the medium was changed to the neural differentiation medium containing 50% Neurobasal, 50% DMEM/F12 supplemented with 1× N-2 supplement, B-27 supplement, glucose (0.4 mg/ml), cAMP (0.15 µg/ml, Sigma-Aldrich), 1% MEM-NEAA, 1% GlutaMax. Over the next 5 days, organoids were embedded in Matrigel (Corning Life Sciences) and further cultured on a cell culture shaker with a medium change every 2-4 days until the day the cultures were fixed for further analysis. From day 35 onwards the medium was changed to 50% Neurobasal, 50% DMEM/F12 supplemented with 1× N-2 supplement, 1× B-27 supplement, glucose (0.4 mg/ml), cAMP (0.15 µg/ml), insulin (Sigma-Aldrich), 1% Matrigel, 20 ng/ml brain-derived neurotrophic factor (BDNF; CellGS) and 10 ng/ml glial cell-derived neurotrophic factor (GDNF).

Protocol II

Here, we used a modified protocol from Paşca et al. (2015). In brief, iPSCs were dissociated into single cell suspension with StemPro Accutase (Gibco) and organoid formation was performed by transferring 1.5×10^6 iPSCs (5000 cells/microwell) into AggreWell 800 plates (Stemcell Technologies) in medium [50% DMEM-F12 GlutaMax, 50% Neurobasal, 1:100 B-27, 1:200 N-2, 1:200 MEM-NEAA, 1 mM L-Glutamine, 1:1000 β-mercaptoethanol (all Gibco), 10 µg/ml insulin (Sigma-Aldrich)] supplemented with the two SMAD pathway inhibitors dorsomorphin (1 µM, Sigma-Aldrich) and SB-431542 (10 µM, AxonMedChem), as well as with the ROCK inhibitor Y-27632 (10 µM, Hiss Diagnostics). As described above, iPSCs from the same genetic background with and without doxycycline-inducible eGFP construct were mixed in the ratio 10/90, respectively. For the first 5 days, the medium without ROCK inhibitor was changed daily. Afterwards, the organoids were transferred into a CERO tube (OLS OMNI Life Science) and cultivated in a rotating CERO table-top bioreactor (CERO 3D bioreactor, OLS OMNI Life Science). From day 5 to day 12, organoids were fed every other day. On day 12, medium containing bFGF (10 ng/ml, Biotechne) instead of SMAD inhibitors was used for 4 days. From day 16 on, organoids were maintained in unsupplemented medium with medium changes every other day.

Generation of the mixed 3D cultures containing doxycycline-inducible EGFP-labeled iPSCs

In order to generate mixed 3D cortical organoids containing EGFP cells according to protocol I or II, we used iPSCs carrying a doxycycline-inducible EGFP cassette, which was knocked into the AAVS1 locus as previously described (Qian et al., 2014; Peitz et al., 2020). IPSCs were dissociated to a single cell suspension with StemPro Accutase (Gibco). Then, 90% of unlabeled iPSCs were gently and thoroughly mixed with 10% EGFP-labeled iPSCs from the same genetic background and seeded into AggreWell plates as described above. Doxycycline (1 µg/ml, Sigma-Aldrich) was added continuously with every medium change from day 0 (day of mixing) onwards. Except for the doxycycline treatment, the 3D cultures were maintained under the same conditions as iPSC-derived cultures containing 100% of unlabeled cells.

Specimen preparation and microscopy

Here, we give an overview of the methods for specimen preparation, expansion and microscopy. Detailed experimental procedures for both short and extended protocols, and the solutions required, can be found in the supplementary Materials and Methods.

Immunochemistry

Immunohistochemistry was optimized from standard protocols. All used chemicals are summarized in Table S1. Details of the procedure are given in the supplementary Materials and Methods. In brief, the fixed 3D cultures were first permeabilized using CHAPS in the permeabilization buffer (1× PBS, 0.5% CHAPS) on a shaker at 37°C. The time varied depending on the size of the sample, e.g. 1 h for a 1-month-old sample. After permeabilization, samples were washed three times with 1× PBS at room temperature (RT). To prevent unspecific binding of the primary antibody, the samples were incubated with blocking buffer (1× PBS, 5% normal goat serum, 0.3% Triton X-100, 0.02% sodium azide) on a shaker overnight (ON) at RT. After blocking, the organoids were incubated ON in blocking buffer with the primary antibody (see Table S2) on a shaker at 4°C. The following day, slices were washed at RT in blocking buffer three times for 30 min and incubated ON in secondary antibody (see Table S3) on a shaker at 4°C. For nuclear staining, all samples were stained using Hoechst 33342 (H3570, Invitrogen).

Organoid expansion

The expansion microscopy protocol was adopted from Chozinski et al. (2016). Details of the procedure are given in the supplementary Materials and Methods. In short, the immunostained organoids were incubated with 2 mM methylacrylic acid-NHS linker for 24 h on a shaker at RT. After washing three times in PBS, the organoids were incubated for 16 h in the monomer solution (8.6% sodium acrylate, 2.5% acrylamide, 0.15% N,N′-methylenebisacrylamide and 11.7% NaCl in 1× PBS) on a shaker at 4°C.

The gelling solution was prepared by adding 4-hydroxy-TEMPO (0.01%), TEMED (0.2%) and ammonium persulfate (0.2%) to fresh monomer solution. During gelling, the organoids were placed in a 24-well plate on ice to avoid early polymerization. After applying the gelling solution, samples were put on a shaker at 4°C for 5 min and then transferred to the gelling chamber, followed by 3 h incubation at 37°C. After the gel formation, the samples were incubated at 37°C in the digestion buffer (50 mM Tris, 1 mM EDTA, 0.5% Triton X-100, 0.8 M guanidine HCl, and 16 U/ml of proteinase K; pH 8.0), exchanging the buffer every 24 h. In general, a 2-month-old organoid takes about two complete days to be completely digested. After digestion, the buffer was removed and the samples were washed three times with PBS.

Light-sheet microscopy

For light-sheet microscopy we used a custom-built setup. In short, for fluorescence excitation, four fiber-coupled lasers emitting at 405, 488, 561 and 638 nm (Hübner Photonics) were employed. The horizontally scanned light sheet was generated by a galvanometer system with silver-coated mirrors. The adjustment of the beam waist position within the sample chamber was realized by relay optics mounted on a linear precision stage. The beam waist in the object plane was adjusted to a $1/e^2$ diameter of 6.5±0.02 µm for the 405 nm, 7.3±0.02 µm for the 488 nm, 7.0±0.02 µm for the 561 nm and 8.3±0.02 µm for the 638 nm laser lines. For illumination we used a Mitutoyo 10× NA 0.28 air objective. Our custom-designed sample chamber featured an illumination window formed by a conventional 24×24 mm coverslip with a thickness of 0.17 mm. The sample was observed from the top using different objective lenses (Table 2). The sample was mounted on a coverslip, which could be moved in three spatial directions by motorized micro-translation stages. In some experiments an optional 1.5× magnification (Nikon) was used. We used a sCMOS camera (2048×2048 pixels, pixel size 6.5 µm, Orca Flash 4.0 V2, Hamamatsu Photonics K.K.) for data acquisition in global shutter mode. All electronic components were controlled by a custom-written LabView program.

Mesoscopic imaging

Mesoscopic imaging and analysis yield information on the topology of complete organoids, which is helpful, for example, to analyze batch-to-batch differences.

For imaging, the digested specimen was fixed on a coverslip with poly-L-lysine to avoid movements during the measurement. Then, the coverslip was inserted into the sample holder and placed into the sample chamber filled with PBS solution, which resulted in an expansion by a factor of 1.5.

Before image acquisition, a visual inspection of the sample was performed to verify a successful sample preparation. Then, the samples were analyzed using LSFM employing a 10× water immersion (WI) objective lens with an NA of 0.3 and an effective field of view of 998 μm^2. The achieved real and effective optical resolutions are given in Table 2. Owing to the large size of the sample, imaging in a mosaic fashion was needed in order to image the whole organoid.

Microscopic imaging

For imaging at the microscopic scale, the organoids were prepared as described above, yielding a transparent 1.5-fold expanded specimen. Now, however, they were examined with a high-resolution long-distance objective with an NA of 1.1 enabling an optical resolution of about 0.3 µm laterally and 1.1 µm axially. This resulted in effective resolutions of 0.2 and 0.7 µm, respectively, when considering the sample expansion (Table 2). Thus, the lateral resolution increased by a factor of ∼4 and the axial resolution by a factor of ∼15 compared with mesoscopic imaging. This made structural characterization possible at the cellular length range. Imaging of complete organoids at this resolution would produce about 500 GB data per 1 mm^3 and per channel, which would require high-end image processing workstations for analysis. Therefore, imaging of complete organoids at this resolution is often not advisable, although it is principally possible. Rather, certain regions of interest (ROIs) should be selected in the mesoscale data for subsequent analysis at the microscopic scale.

Nanoscopic imaging

For imaging at the nanoscopic scale, organoids were prepared as described above, yielding a transparent 1.5-fold expanded specimen. Then, the buffer solution into which the sample was placed was replaced by bi-distilled water. This led to an ∼4-fold expansion compared with the original sample size. Such samples were examined with a high-resolution long-distance objective (NA 1.1) enabling an optical resolution of about 0.3 µm laterally and 1.1 µm axially. This yielded effective super-resolution of 0.1 and 0.3 µm, respectively, when considering the sample expansion (Table 2), which made structural characterization possible at the subcellular length range. The resolution can further be improved by 3D image deconvolution. When imaging, the axial step size must be adjusted such that deconvolution can optimally be performed.

Data processing

We processed 3D stacks of raw 16-bit images using custom-written MATLAB scripts, which allowed parallel data processing (Gonzalez et al., 2009). In a first step, the intensity histograms were adjusted to normalize brightness and contrast throughout the complete dataset.

Complete 3D representations of the samples were possible after several 3D datasets were stitched together using Fiji (Schindelin et al., 2012) and the stitching plugin of Preibisch et al. (2009). In order to optimize the stitching process, especially when datasets exceeded the available RAM of the workstation, the process was performed in two steps. First, substacks of the 3D datasets were created using a Fiji script. Each substack contained about 15% of the information located in the center of the full stack. Secondly, each substack was stitched to its respective neighboring substack yielding the best overlap in terms of the cross-correlation measure. Based on the localization information of each substack after stitching, the full 3D stacks were stitched.

A final step to improve the contrast throughout the 3D data was performed after stitching, to compensate for possible intensity variations of the sample in the axial direction. To this end, a histogram equalization was performed in every image plane of the stitched dataset. For calculation of z-projections, the maximum intensity projection algorithm of Fiji was used.

Deconvolution

As outlined in the Results section, selected image stacks were spatially deconvolved using Huygens (Professional version 21.10, Scientific Volume Imaging). Deconvolution was performed using theoretical point spread functions (PSF), based on microscopic parameters, or a measured PSF determined by analysis of fluorescent microbeads embedded in 1% agarose gel. The classical maximum likelihood estimation algorithm was used, and a signal-to-noise ratio value between 12 and 20 for a maximum number of iterations between 60 and 100 were selected.

The 3D representation of the data was achieved using the Surpass view in Imaris (Version 9.7.2, Bitplane). Data processing was performed on a workstation equipped with two Intel Xeon Platinum 8160 CPU (2.1 GHz, 24 cores), 512 GB memory, and an Nvidia Quadro P5000 GPU (16 GB GDDR5X) running under Windows 10 Pro.

Table 2. True and effective optical resolutions of imaging at various scales

Scale	Objective lens	True optical resolution		Effective optical resolution		Data size per 1 mm^3 sample
		lateral	axial	lateral	axial	
Mesoscale	10×, NA 0.3, WI	1.2 µm	17.8 µm	0.8 µm	11.8 µm	5.5 GB
Microscale	25×, NA 1.1 WI	0.3 µm	1.1 µm	0.2 µm	0.8 µm	500 GB
Nanoscale	25×, NA 1.1 WI	0.3 µm	1.1 µm	0.1 µm	0.3 µm	8 TB

Acknowledgements

We gratefully acknowledge expert support by the micromechanical workshop of the Institute of Physical and Theoretical Chemistry of the University of Bonn under the guidance of Daniel Poetes.

Competing interests

The authors declare no competing or financial interests.

Author contributions

Conceptualization: O.B., M.K.S., U.K.; Methodology: J.E.R.-G., V.I., L.S., S.W.C.A.Y., Y.B., O.B., M.K.S.; Validation: J.E.R.-G., V.I., M.K.S., U.K.; Formal analysis: J.E.R.-G.; Investigation: J.E.R.-G., V.I.; Resources: L.S., S.W.C.A.Y., Y.B.; Data curation: J.E.R.-G.; Writing - original draft: J.E.R.-G., V.I., S.W.C.A.Y., Y.B., O.B.; Writing - review & editing: J.E.R.-G., V.I., Y.B., O.B., U.K.; Visualization: J.E.R.-G.; Supervision: O.B., M.K.S., U.K.; Project administration: O.B., U.K.; Funding acquisition: O.B., M.K.S., U.K.

Funding

This work was supported by the Deutsche Forschungsgemeinschaft (SFB 1089-TP P03 and SFB 1089-TP B06 to L.S. and M.K.S.; SPP 2041 'Computational Connectomics' to M.K.S. and U.K.). Furthermore, it was funded by the TRA Matter and TRA Life & Health (University of Bonn) as part of the Excellence Strategy of the federal and state governments. The Deutscher Akademischer Austauschdienst and the Agencia Nacional de Investigación y Desarrollo provided grants to J.E.R.-G. Further financial support was obtained from the European Commission to O.B. (NeuroStemcell-Reconstruct 874758).

Peer review history

The peer review history is available online at https://journals.biologists.com/dev/article-lookup/doi/10.1242/dev.200439.

References

Adhya, D., Chennell, G., Crowe, J. A., Valencia-Alarcón, E. P., Seyforth, J., Hosny, N. A., Yasvoina, M. V., Forster, R., Baron-Cohen, S., Vernon, A. C. et al. (2021). Application of Airy beam light sheet microscopy to examine early neurodevelopmental structures in 3D hiPSC-derived human cortical spheroids. *Mol. Autism* **12**, 4. doi:10.1186/s13229-021-00413-1

Albanese, A., Swaney, J. M., Yun, D. H., Evans, N. B., Antonucci, J. M., Velasco, S., Sohn, C. H., Arlotta, P., Gehrke, L. and Chung, K. (2020). Multiscale 3D phenotyping of human cerebral organoids. *Sci. Rep.* **10**, 21487. doi:10.1038/s41598-020-78130-7

Baumgart, E. and Kubitscheck, U. (2012). Scanned light sheet microscopy with confocal slit detection. *Opt. Express* **20**, 21805-21814. doi:10.1364/OE.20.021805

Benito-Kwiecinski, S., Giandomenico, S. L., Sutcliffe, M., Riis, E. S., Freire-Pritchett, P., Kelava, I., Wunderlich, S., Martin, U., Wray, G. A., McDole, K. et al. (2021). An early cell shape transition drives evolutionary expansion of the human forebrain. *Cell* **184**, 2084-2102.e19. doi:10.1016/j.cell.2021.02.050

Bershteyn, M., Nowakowski, T. J., Pollen, A. A., Di Lullo, E., Nene, A., Wynshaw-Boris, A. and Kriegstein, A. R. (2017). Human iPSC-derived cerebral organoids model cellular features of lissencephaly and reveal prolonged mitosis of outer radial glia. *Cell Stem Cell* **20**, 435-449.e4. doi:10.1016/j.stem.2016.12.007

Bhaduri, A., Andrews, M. G., Mancia Leon, W., Jung, D., Shin, D., Allen, D., Jung, D., Schmunk, G., Haeussler, M., Salma, J. et al. (2020). Cell stress in cortical organoids impairs molecular subtype specification. *Nature* **578**, 142-148. doi:10.1038/s41586-020-1962-0

Brémond Martin, C., Simon Chane, C., Clouchoux, C. and Histace, A. (2021). Recent trends and perspectives in cerebral organoids imaging and analysis. *Front. Neurosci.* **15**, 629067. doi:10.3389/fnins.2021.629067

Bürgers, J., Pavlova, I., Rodriguez-Gatica, J. E., Henneberger, C., Oeller, M., Ruland, J. A., Siebrasse, J. P., Kubitscheck, U. and Schwarz, M. K. (2019). Light-sheet fluorescence expansion microscopy: fast mapping of neural circuits at super resolution. *Neurophoton* **6**, 015005. doi:10.1117/1.NPh.6.1.015005

Chen, B.-C., Legant, W. R., Wang, K., Shao, L., Milkie, D. E., Davidson, M. W., Janetopoulos, C., Wu, X. S., Hammer, J. A., Liu, Z. et al. (2014). Lattice light-sheet microscopy: imaging molecules to embryos at high spatiotemporal resolution. *Science* **346**, 1257998. doi:10.1126/science.1257998

Chen, F., Tillberg, P. W. and Boyden, E. S. (2015). Expansion microscopy. *Science* **347**, 543-548. doi:10.1126/science.1260088

Chozinski, T. J., Halpern, A. R., Okawa, H., Kim, H.-J., Tremel, G. J., Wong, R. O. L. and Vaughan, J. C. (2016). Expansion microscopy with conventional antibodies and fluorescent proteins. *Nat. Methods* **13**, 485-488. doi:10.1038/nmeth.3833

Dean, K. M., Roudot, P., Welf, E. S., Danuser, G. and Fiolka, R. (2015). Deconvolution-free subcellular imaging with axially swept light sheet microscopy. *Biophys. J.* **108**, 2807-2815. doi:10.1016/j.bpj.2015.05.013

Dekkers, J. F., Alieva, M., Wellens, L. M., Ariese, H. C. R., Jamieson, P. R., Vonk, A. M., Amatngalim, G. D., Hu, H., Oost, K. C., Snippert, H. J. G. et al. (2019). High-resolution 3D imaging of fixed and cleared organoids. *Nat. Protoc.* **14**, 1756-1771. doi:10.1038/s41596-019-0160-8

Di Lullo, E. and Kriegstein, A. R. (2017). The use of brain organoids to investigate neural development and disease. *Nat. Rev. Neurosci.* **18**, 573-584. doi:10.1038/nrn.2017.107

Dodt, H.-U., Leischner, U., Schierloh, A., Jährling, N., Mauch, C. P., Deininger, K., Deussing, J. M., Eder, M., Zieglgänsberger, W. and Becker, K. (2007). Ultramicroscopy: three-dimensional visualization of neuronal networks in the whole mouse brain. *Nat. Methods* **4**, 331-336. doi:10.1038/nmeth1036

Edwards, S. J., Carannante, V., Kuhnigk, K., Ring, H., Tararuk, T., Hallböök, F., Blom, H., Önfelt, B. and Brismar, H. (2020). High-resolution imaging of tumor spheroids and organoids enabled by expansion microscopy. *Front. Mol. Biosci.* **7**, 208. doi:10.3389/fmolb.2020.00208

Ellefsen, K. L. and Parker, I. (2018). Dynamic Ca^{2+} imaging with a simplified lattice light-sheet microscope: a sideways view of subcellular Ca^{2+} puffs. *Cell Calcium* **71**, 34-44. doi:10.1016/j.ceca.2017.11.005

Fu, Q., Martin, B. L., Matus, D. Q. and Gao, L. (2016). Imaging multicellular specimens with real-time optimized tiling light-sheet selective plane illumination microscopy. *Nat. Commun.* **7**, 11088. doi:10.1038/ncomms11088

Gao, R., Asano, S. M., Upadhyayula, S., Pisarev, I., Milkie, D. E., Liu, T.-L., Singh, V., Graves, A., Huynh, G. H., Zhao, Y. et al. (2019). Cortical column and whole-brain imaging with molecular contrast and nanoscale resolution. *Science* **363**, eaau8302. doi:10.1126/science.aau8302

Giandomenico, S. L., Mierau, S. B., Gibbons, G. M., Wenger, L. M. D., Masullo, L., Sit, T., Sutcliffe, M., Boulanger, J., Tripodi, M., Derivery, E. et al. (2019). Cerebral organoids at the air-liquid interface generate diverse nerve tracts with functional output. *Nat. Neurosci.* **22**, 669-679. doi:10.1038/s41593-019-0350-2

Gonzalez, R. C., Woods, R. E. and Eddins, S. L. (2009). *Digital Image Processing Using MATLAB*. s.l: Gatesmark Publshing.

Huisken, J., Swoger, J., Del Bene, F., Wittbrodt, J. and Stelzer, E. H. (2004). Optical sectioning deep inside live embryos by selective plane illumination microscopy. *Science* **305**, 1007-1009. doi:10.1126/science.1100035

Iefremova, V., Manikakis, G., Krefft, O., Jabali, A., Weynans, K., Wilkens, R., Marsoner, F., Brändl, B., Müller, F.-J., Koch, P. et al. (2017). An organoid-based model of cortical development identifies non-cell-autonomous defects in Wnt signaling contributing to Miller-Dieker syndrome. *Cell Rep.* **19**, 50-59. doi:10.1016/j.celrep.2017.03.047

Ku, T., Swaney, J., Park, J.-Y., Albanese, A., Murray, E., Cho, J. H., Park, Y.-G., Mangena, V., Chen, J. and Chung, K. (2016). Multiplexed and scalable super-resolution imaging of three-dimensional protein localization in size-adjustable tissues. *Nat. Biotechnol.* **34**, 973-981. doi:10.1038/nbt.3641

LaMonica, B. E., Lui, J. H., Hansen, D. V. and Kriegstein, A. R. (2013). Mitotic spindle orientation predicts outer radial glial cell generation in human neocortex. *Nat. Commun.* **4**, 1665. doi:10.1038/ncomms2647

Lancaster, M. A., Renner, M., Martin, C.-A., Wenzel, D., Bicknell, L. S., Hurles, M. E., Homfray, T., Penninger, J. M., Jackson, A. P. and Knoblich, J. A. (2013). Cerebral organoids model human brain development and microcephaly. *Nature* **501**, 373-379. doi:10.1038/nature12517

Lancaster, M. A., Corsini, N. S., Wolfinger, S., Gustafson, E. H., Phillips, A. W., Burkard, T. R., Otani, T., Livesey, F. J. and Knoblich, J. A. (2017). Guided self-organization and cortical plate formation in human brain organoids. *Nat. Biotechnol.* **35**, 659-666. doi:10.1038/nbt.3906

Masselink, W., Reumann, D., Murawala, P., Pasierbek, P., Taniguchi, Y., Bonnay, F., Meixner, K., Knoblich, J. A. and Tanaka, E. M. (2019). Broad applicability of a streamlined ethyl cinnamate-based clearing procedure. *Development* **146**, dev166884. doi:10.1242/dev.166884

Neyra, E. G., Martínez-Matos, Ó. and Vaveliuk, P. (2020). Ultra-long light sheets via curved beam intercrossing. *OSA Continuum* **3**, 2062-2069. doi:10.1364/OSAC.393073

Paşca, A. M., Sloan, S. A., Clarke, L. E., Tian, Y., Makinson, C. D., Huber, N., Kim, C. H., Park, J.-Y., O'Rourke, N. A., Nguyen, K. D. et al. (2015). Functional cortical neurons and astrocytes from human pluripotent stem cells in 3D culture. *Nat. Methods* **12**, 671-678. doi:10.1038/nmeth.3415

Peitz, M., Krutenko, T. and Brüstle, O. (2020). Protocol for the standardized generation of forward programmed cryopreservable excitatory and inhibitory forebrain neurons. *STAR Protoc.* **1**, 100038. doi:10.1016/j.xpro.2020.100038

Pollen, A. A., Bhaduri, A., Andrews, M. G., Nowakowski, T. J., Meyerson, O. S., Mostajo-Radji, M. A., Di Lullo, E., Alvarado, B., Bedolli, M., Dougherty, M. L. et al. (2019). Establishing cerebral organoids as models of human-specific brain evolution. *Cell* **176**, 743-756.e17. doi:10.1016/j.cell.2019.01.017

Preibisch, S., Saalfeld, S. and Tomancak, P. (2009). Globally optimal stitching of tiled 3D microscopic image acquisitions. *Bioinformatics* **25**, 1463-1465. doi:10.1093/bioinformatics/btp184

Qian, K., Huang, C. T.-L., Huang, C.-L., Chen, H., Blackbourn, L. W., Chen, Y., Cao, J., Yao, L., Sauvey, C., Du, Z. et al. (2014). A simple and efficient system for regulating gene expression in human pluripotent stem cells and derivatives. *Stem Cells* **32**, 1230-1238. doi:10.1002/stem.1653

Qian, X., Song, H. and Ming, G. (2019). Brain organoids: advances, applications and challenges. *Development* **146**, dev166074. doi:10.1242/dev.166074

Quadrato, G., Brown, J. and Arlotta, P. (2016). The promises and challenges of human brain organoids as models of neuropsychiatric disease. *Nat. Med.* **22**, 1220-1228. doi:10.1038/nm.4214

Quadrato, G., Nguyen, T., Macosko, E. Z., Sherwood, J. L., Min Yang, S., Berger, D. R., Maria, N., Scholvin, J., Goldman, M., Kinney, J. P. et al. (2017). Cell diversity and network dynamics in photosensitive human brain organoids. *Nature* **545**, 48-53. doi:10.1038/nature22047

Schindelin, J., Arganda-Carreras, I., Frise, E., Kaynig, V., Longair, M., Pietzsch, T., Preibisch, S., Rueden, C., Saalfeld, S., Schmid, B. et al. (2012). Fiji: an open-source platform for biological-image analysis. *Nat. Methods* **9**, 676-682. doi:10.1038/nmeth.2019

Schwarz, M. K. and Kubitscheck, U. (2021). Expansion light sheet fluorescence microscopy of extended biological samples: applications and perspectives. *Prog. Biophys. Mol. Biol*. **168**, 33-36. doi:10.1016/j.pbiomolbio.2021.09.004

Silvestri, L., Bria, A., Sacconi, L., Iannello, G. and Pavone, F. S. (2012). Confocal light sheet microscopy: micron-scale neuroanatomy of the entire mouse brain. *Opt. Express* **20**, 20582-20598. doi:10.1364/OE.20.020582

Stockhausen, A., Bürgers, J., Rodriguez-Gatica, J. E., Schweihoff, J., Merkel, R., Prigge, J. M., Schwarz, M. K. and Kubitscheck, U. (2020). Hard-wired lattice light-sheet microscopy for imaging of expanded samples. *Opt. Express* **28**, 15587-15600. doi:10.1364/OE.393728

Tillberg, P. W., Chen, F., Piatkevich, K. D., Zhao, Y., Yu, C.-C., English, B. P., Gao, L., Martorell, A., Suk, H.-J., Yoshida, F. et al. (2016). Protein-retention expansion microscopy of cells and tissues labeled using standard fluorescent proteins and antibodies. *Nat. Biotechnol.* **34**, 987-992. doi:10.1038/nbt.3625

Ueda, H. R., Ertürk, A., Chung, K., Gradinaru, V., Chédotal, A., Tomancak, P. and Keller, P. J. (2020). Tissue clearing and its applications in neuroscience. *Nat. Rev. Neurosci.* **21**, 61-79. doi:10.1038/s41583-019-0250-1

Velasco, S., Kedaigle, A. J., Simmons, S. K., Nash, A., Rocha, M., Quadrato, G., Paulsen, B., Nguyen, L., Adiconis, X., Regev, A. et al. (2019). Individual brain organoids reproducibly form cell diversity of the human cerebral cortex. *Nature* **570**, 523-527. doi:10.1038/s41586-019-1289-x

Vettenburg, T., Dalgarno, H. I. C., Nylk, J., Coll-Lladó, C., Ferrier, D. E. K., Čižmár, T., Gunn-Moore, F. J. and Dholakia, K. (2014). Light-sheet microscopy using an Airy beam. *Nat. Methods* **11**, 541-544. doi:10.1038/nmeth.2922

Yingling, J., Youn, Y. H., Darling, D., Toyo-Oka, K., Pramparo, T., Hirotsune, S. and Wynshaw-Boris, A. (2008). Neuroepithelial stem cell proliferation requires LIS1 for precise spindle orientation and symmetric division. *Cell* **132**, 474-486. doi:10.1016/j.cell.2008.01.026

Zhao, S., Todorov, M. I., Cai, R., Maskari, R. A., Steinke, H., Kemter, E., Mai, H., Rong, Z., Warmer, M., Stanic, K. et al. (2020). Cellular and molecular probing of intact human organs. *Cell* **180**, 796-812.e19. doi:10.1016/j.cell.2020.01.030

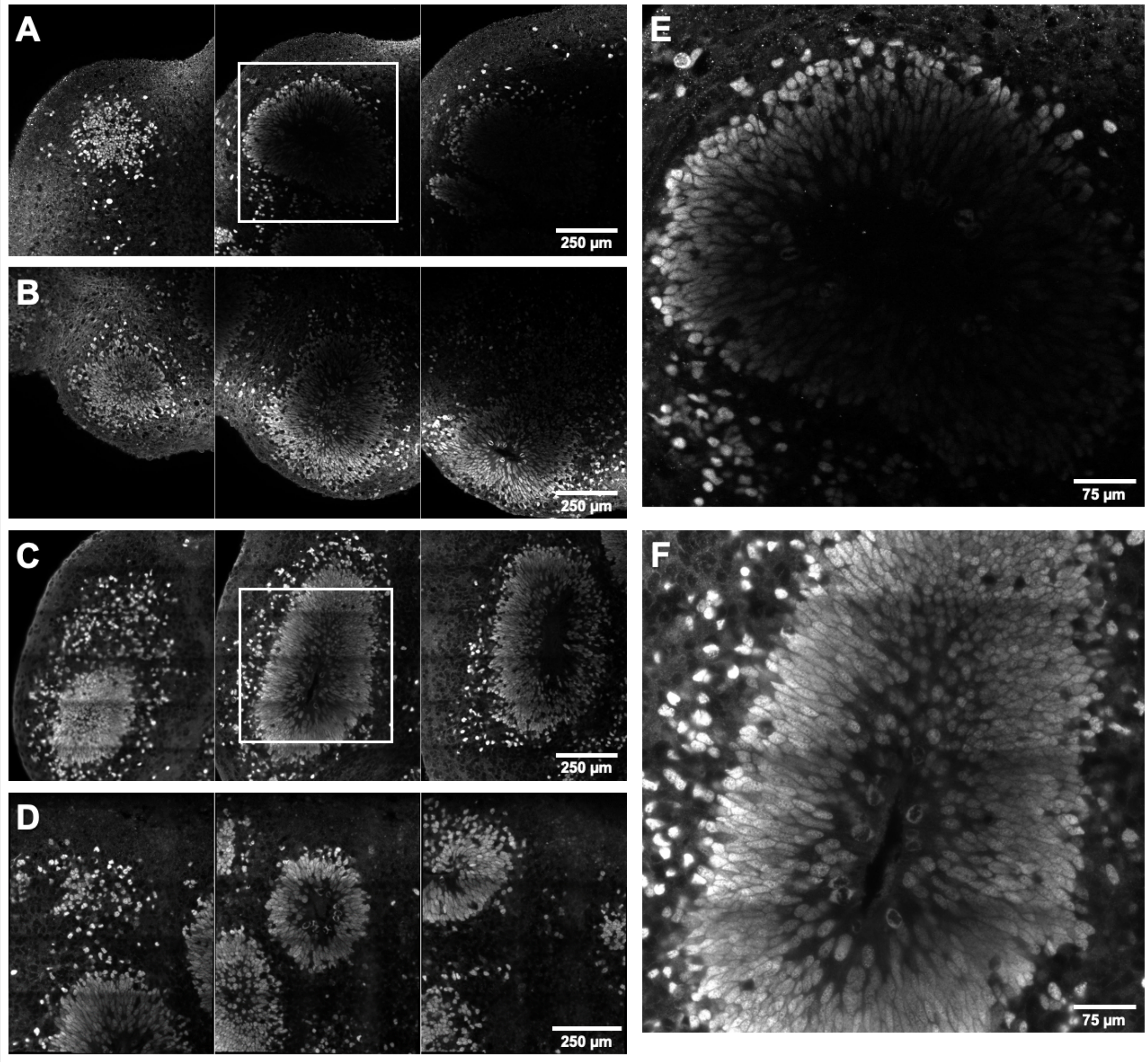

Fig. S1. Comparison of the permeabilization effect using TritonX-100 and CHAPS in four different brain organoids (protocol I) stained against the neural progenitor marker SOX2. Optical sections of (A) two months and (B) three months old brain organoids, respectively, permeabilized using 0.5% Triton X-100 in PBS. The sections were 200 µm apart from each other starting at the upper surface of the organoids. Obviously, the labeling is strong in the outer region and decreasing towards the interior of the organoid. Optical sections of (C, D) two months old brain organoids permeabilized using 0.5% CHAPS in PBS. The sections were taken 200 µm apart from each other. (E) and (F) Magnification of the regions marked in (A) and (D), respectively. The organoids are labeled throughout the complete volume. Samples were stained against SOX2 (1:100), after the permeabilization step, as described in Materials and Methods. The images were obtained using a custom built LSFM, after 1.5-fold expansion of the samples.

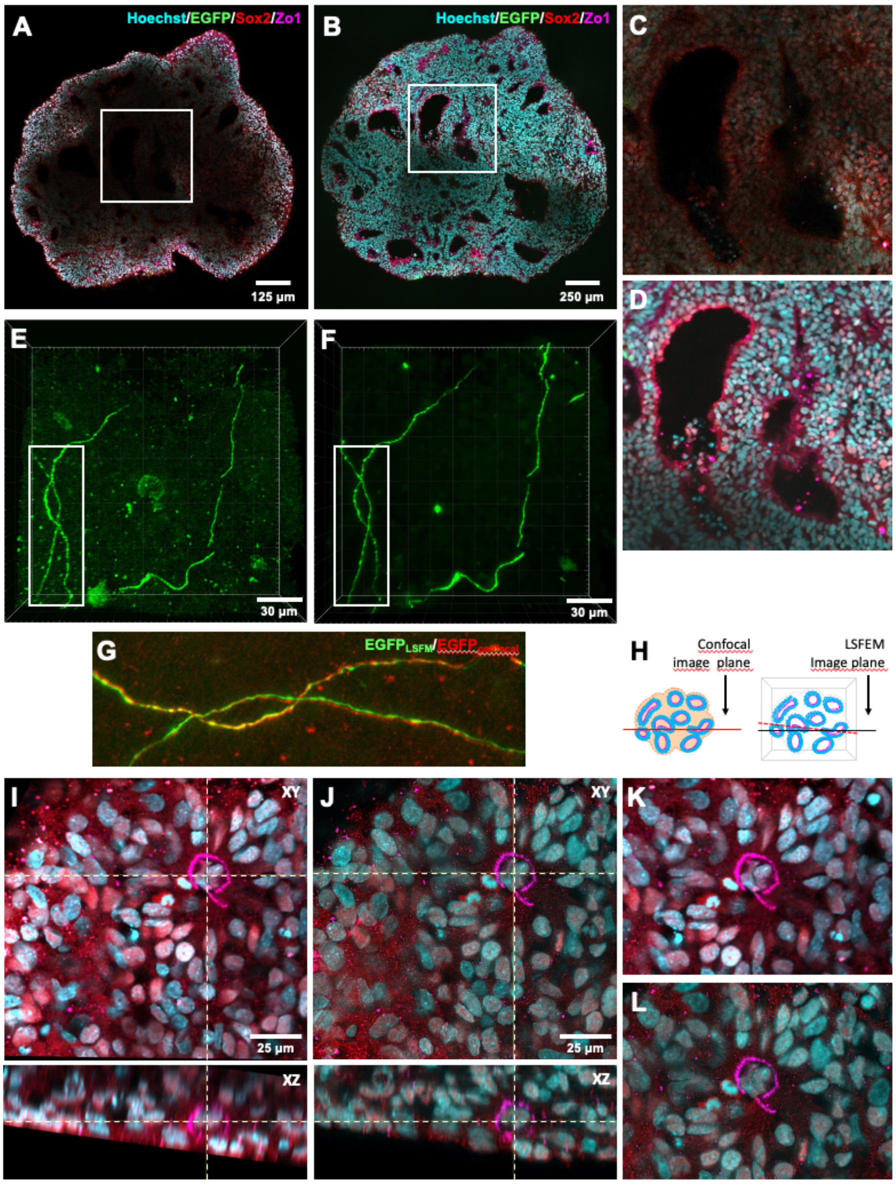

Fig. S2. Effect of clearing procedure on the staining and on the structure of a 40 days old brain organoid (protocol II) containing GFP-positive cells. The organoid was labeled by Hoechst (cyan) , progenitor cell marker Sox2 (red) and ZO1 (magenta). It was imaged before and after clearing and expansion (1.5X). (A) Optical section of the organoid acquired with a Zeiss LSM 880 (25x NA 0.8 W objective) in a depth of 1.2 mm. (B) Optical slice after digestion and 1.5-fold expansion acquired in the LSFM (10x NA 0.3 objective). (C and D) Magnification of the region marked in (A) and (B), respectively. The image shown in (C) was contrast-enhanced. (E) Rendering of the EGFP-channel from a 3D stack with a volume of 212 x 212 x 39 μm^3. The underlying image stack was obtained with the Zeiss LSM 880 (40x NA 1.1 W objective) from the same sample. (F) Rendering of a 3D stack of the same volume of this sample after digestion and 1.5-fold expansion. The corresponding image stack was obtained using the LSFM (25x NA 1.1 objective). This example demonstrates also the excellent conservation of the fluorescence of the autofluorescent protein EGFP. It is obvious that the overall data quality is superior after digestion and expansion. (G) Direct comparison between the marked image sections shown in (E) and (F). The overlay reveals the very close structural correspondence of the pre- and 1.5-fold expanded structures. (H) Image fields in (A) and (B) are not identical, but they share a common region (C, D). This is due to a small sample rotation, which often occurs during the sample manipulation and transfer into the LSFM chamber. The consequence is that the optical section imaged by the LSFM may slightly be tilted compared to an optical section obtained in the LSM880. However, the 3D data (E, F, G) reveal that the structures are preserved with only very subtle alterations. (I, J) Orthogonal projections of the volumes acquired for (E and F) showing the further channels. It can be seen that the shape of the apical surface of the rosette was maintained after the digestion-expansion procedure (K, confocal; L, LSFM). The loss of signal and resolution due to scattering in the confocal image (I) is evident, because the sample is not transparent.

Table S1. Chemicals

Name	Vendor	Catalog #
4-hydroxy-TEMPO	Sigma-Aldrich	176141
Acrylamide	Sigma-Aldrich	79-06-1
Agarose	Applichem	A8963
Ammonium persulfate	Sigma-Aldrich	A3678
CHAPS	Carl Roth GmbH	1479.1
EDTA	Carl Roth GmbH	8043.3
Guanidine HCl	Applichem	A1499
Hoechst 33342	Invitrogen	H3570
Methylacrylic acid-NHS	Sigma-Aldrich	730300
N,N’- methylenebisacrylamide	Sigma	M1533
Sodium Chloride	Carl Roth GmbH	HN00.2
Normal goat serum	Jackson ImmunoResearch	005-000-121
PBS (-/-)	Gibco	14190-094
Paraformaldehyde Solution, 4%	Alfa Aesar	J19943.K2
Poly-L-lysine	Sigma-Aldrich	P8920
Proteinase K	New England BioLabs	P8107S
Sodium acrylate	Sigma-Aldrich	408220
Sodium azide	Carl Roth GmbH	K305.1
TEMED	Sigma	T7024
Tris	Carl Roth GmbH	4855,2
Triton™ X-100	Sigma-Aldrich	X100-100ML

Table S2. Primary Antibodies

Name	Host	Dilution	Vendor	Catalog #
Homer 1	Guinea pig	1:1000	Synaptic Systems	160 004
HOPX	Mouse	1:250	Santa Cruz	sc398703
HOPX	Rabbit	1:200	Proteintech	11419-1-AP
N-cadherin	Mouse	1:250	BD Biosciences	610921
SOX2	Mouse	1:100	R&D Systems	MAB2018
Synapsin 1	Rabbit	1:1000	Synaptic Systems	106 103
TBR2	Rabbit	1:250	Abcam	ab23345
ZO-1	Rabbit	1:200	Invitrogen	40-2200
MAP2	Mouse	1:500	Sigma-Aldrich	M1406

Table S3. Secondary Antibodies

Name	Host	Species Reactivity	Dilution	Vendor	Catalog #
Alexa 405	Goat	Anti-Mouse IgG	1:500	Thermo Fisher Scientific	A3553
Alexa 555	Goat	Anti-Mouse IgG	1:400	Thermo Fisher Scientific	A21424
Alexa 555	Goat	Anti-Rabbit IgG	1:400	Thermo Fisher Scientific	A21429
Alexa 594	Goat	Anti-Guinea Pig IgG	1:500	Thermo Fisher Scientific	A11076
Atto 550	Goat	Anti-Mouse IgG	1:500	Sigma-Aldrich	43394
Atto 647N	Goat	Anti-Mouse IgG	1:400	Sigma-Aldrich	50185
Atto 647N	Goat	Anti-Rabbit IgG	1:500	Sigma-Aldrich	40839

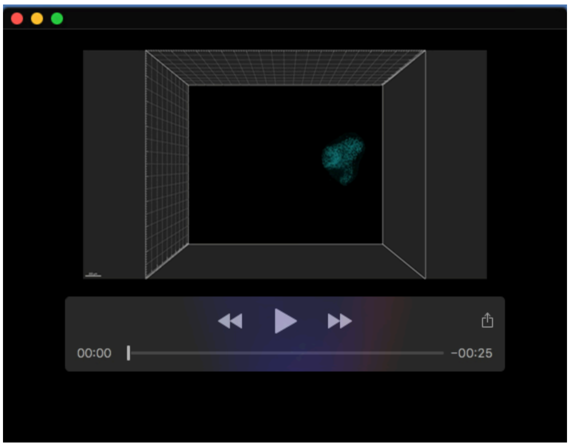

Movie 1. Apical surfaces of neuroepithelial structures in a 2-month-old brain organoid. The movie shows the 3D data of the organoid shown in Fig. 4. Staining was against cell nuclei (Hoechst, cyan) and ZO1 (magenta). The last phase of the movie shows the cropped apical surfaces of the neuroepithelium inside the organoid. The color labeling was randomly generated according to surface area.

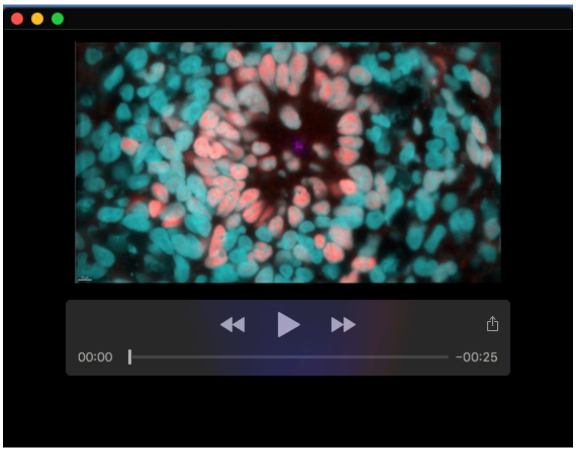

Movie 2. Analysis of cleavage planes. The movie shows the 3D data of the rosette and apical VZ lumen surface shown in Fig. 7.

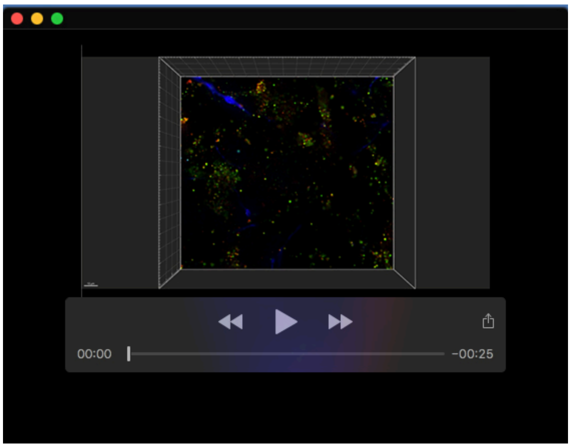

Movie 3. Pre- and postsynaptic structures in a 14-month-old brain organoid. The movie shows the 3D data and renderings of Fig. 8. The organoid contained 10% EGFP-expressing cells and was labeled by Hoechst and stained with antibodies to the pre- and post-synaptic proteins synapsin 1 (SYN1, green) and Homer1 (red). Please note that in this movie EGFP is shown in blue.

Supplementary Materials and Methods

Short Protocol: Organoid Expansion

Generally, incubation times depend on the size (age) of the organoid.

Immunochemistry

1. **Permeabilization:** Incubate organoid with permeabilization buffer at 37°C on a shaker. Duration depends on the size of the sample, e.g. 1h for an 1 month old (mo) organoid.
2. **Wash:** Three times with 1xPBS at room temperature (RT), e.g. 3 x 30 min for 1 mo organoid.
3. **Blocking:** Block samples with blocking buffer at room temperature (RT) on a shaker. 1 mo organoids are incubated for 8h.
4. **Primary antibody (Ab) incubation:** After removing the blocking solution, the samples are incubated in primary antibody in blocking buffer at 4°C, shaking. 1 mo organoids are incubated over night (ON).
5. **Wash:** Three times with blocking buffer at RT, e.g. 3 x 30 min for 1 mo organoid.
6. **Secondary AB incubation:** Incubation with secondary Ab in blocking buffer on a shaker at 4°C. 1 mo organoids are incubated ON.
7. **Wash:** Three times with 1xPBS at RT, e.g. 3 x 30 min for 1 mo organoid.

Pre-expansion imaging (optional)

8. **Nuclear staining:** Incubate samples with Hoechst (5µg/mL).
9. **Wash:** Three times with 1xPBS at RT, e.g. 3 x 30 min for 1 mo organoid.

Expansion

10. **Linking:** Incubation with 2 mM MA-NHS in PBS on shaker at RT. ON incubation for 1 mo organoid.
11. **Wash:** Three times with 1xPBS at RT, e.g. 3 x 30 min for 1 mo organoid.
12. **Monomer:** Incubate with monomer solution (page 13) on shaker at 4°C. ON incubation for 1 mo organoid.
13. **Gelling I:** Incubate with gelling solution on shaker at 4°C. 5 min incubation for 1 mo organoid.

    Gelling II: Transfer samples to prebuild gelling chamber. Incubate in gelling solution for 2h at 37°C. Check regularly if samples are not drying out.
14. **Remove excess gel:** Open the gelling chamber and remove the upper coverslip and excess of the gel around the tissue.

15. **Digestion:** Fill the chamber with digestion buffer and incubate, e.g. ON at 37°C for 1 mo organoids. Place samples into a wet chamber and secure the chamber with paraffin to make sure that the samples will not dry out.
16. **Expansion:** Carefully remove the digestion buffer. Wash the samples in the gelling chamber with distilled water around 3-4 x 20 min.

Transfer sample to the imaging chamber and start microscopy session.

Detailed Protocol: Expansion Procedure

We separate samples in individual wells, and use between 500 µL to 1000 µL of solution per sample in order to cover them completely. This is valid for every step.
Make sure that the plate is protected from light (e.g. aluminum foil) during all steps.
Before transferring the samples into PBS, the pipettes should to be coated using PBST (1xPBS + 0.3% Triton). For larger samples, e.g. 8 mo organoids, we recommend the use of a brush.

Washing buffer: 1xPBS

Permeabilization buffer: 1xPBS, 0.5% CHAPS

Blocking buffer: 1x PBS, 5% normal goat serum, 0.3% TritonX-100, 0.02% sodium azide

Digestion buffer: 50 mM Tris, 1 mM EDTA, 0.5% Triton-X100, 0.8M guanidine HCl, and 16 U/mL of proteinase K; pH 8.0

Immunochemistry

1. **Permeabilization:** Before immunostaining or the expansion protocol, the samples are permeabilized to improve penetration. Incubate the samples at 37°C on a shaker.

Sample age	1 mo	2 mo – 5 mo	>8 mo
Incubation time	1 h	3 h	ON

2. **Wash**: Three times with 1xPBS at room temperature (RT).

Sample age	1 mo	2mo – 5mo	>8mo
Incubation time (3x)	30 min	45 min	1h

3. **Blocking**: Block samples with blocking buffer on a shaker at room temperature (RT). Always use enough solution to cover the sample completely.

Sample age	1 mo	2mo – 5mo	>8mo
Incubation time (3x)	30 min	45 min	1h

For longer blocking sessions place the sample on shaker at 4°C.
For better results, use serum corresponding to the host species of the secondary Ab you will use.

4. **Primary Ab**: After removing blocking solution, it is not necessary to wash the samples. Then, the samples are incubated with primary Ab in blocking buffer on a shaker at 4°C.

Sample age	1 mo	2mo – 5mo	>8mo
Incubation time	1 day	3 days	4 – 5 days

5. **Washing**: Samples are washed three times on a shaker at RT with blocking buffer.

Sample age	1 mo	2mo – 5mo	>8mo
Incubation time (3x)	30 min	45 min	1h

6. **Secondary Ab incubation**: Incubated with secondary antibody in blocking buffer on shaker at 4°C.

Sample age	1 mo	2mo – 5mo	>8mo
Incubation time	1 day	3 days	4-5 days

For better results, e.g. to avoid cross reactivity between antibodies, we recommend immunolabeling in a serial manner instead of parallel combination of antibodies.

7. **Washing**: Wash the sample three times with 1xPBS on shaker at room temperature (RT)

Pre-expansion imaging (optional)

We usually perform a nuclear staining if we perform pre-expansion imaging. Alternatively, nuclear staining could be performed at the end of the expansion protocol (after digestion).

8. Cell nuclei were stained using Hoechst 33342 at a concentration of 5µg/mL.

Sample age	1 mo	2mo – 5mo	>8mo
Incubation time	ON	2 days	3 days

9. **Washing**: Wash the sample three times with 1xPBS on shaker at room temperature (RT).

Sample age	1 mo	2mo – 5mo	>8mo
Incubation time (3x)	30 min	45 min	1 h

For imaging the sample can be placed into a µ-Plate 24 Well Black (ibidi 82426) or a µ-Dish 35-mm glass-bottom dish (ibidi 81158) filled with 1xPBS depending on the size of the sample.

Expansion

10. **Linking**: Incubate with 2mM MA-NHS on a shaker at RT. Dilute MA-NHS 1:500 in PBS from 1M aliquots, which are stored at -20°C. Remove the PBS carefully from the well, or transfer the sample to another well with linking solution using a coated pipette. Each sample is incubated in a separate well.

Sample age	1 mo	2mo – 5mo	>8mo
Incubation time	ON	1 day	2 days

11. **Washing**: Wash the sample three times with 1xPBS on shaker at room temperature (RT).

Sample age	1 mo	2mo – 5mo	>8mo
Incubation time (3x)	30 min	45 min	1 hr

During the last washing step thaw the monomer solution aliquot (stored at -20°C) and put it on ice.

12. **Monomer**: Incubate with monomer solution on a shaker at 4°C. It is important to have the samples on a shaker to improve penetration and thus the linking of the polyacrylamide matrix into the sample.

Sample age	1 mo	2mo – 5mo	>8mo
Incubation time	ON	1 day	2 days

While sample is incubated with the monomer solution, a gelling chamber for the sample should be prepared.
To this end use a coverslip (22 x 22 mm) as a base and place spacers on two opposite corners (see sketch below). The spacers could be made with a double-sided tape, e.g. SPADA 4543VS, which have a thickness of about 100 µm and 9 mm width by folding it as many times as needed until the desired thickness is obtained and then cut it in a rectangular shape (~ 6 x 9 mm stripes).

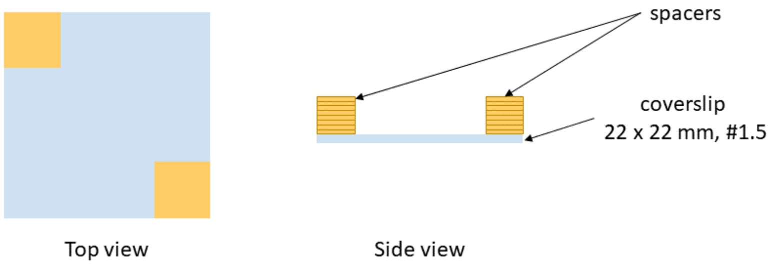

13. **Gelling I**: To prepare the gelling solution, mix monomer solution with TEMPO and TEMED, **adding** ammonium persulfate **at last**, and vortex briefly. For 100µL of gelling solution use 94µL monomer solution, 2µL TEMPO (0.5%), 2µL TEMED (10%) and 2µL APS (10%).

Remove the monomer solution and apply the gelling solution to the sample. Incubate the sample with the gelling solution for 5-10 minutes on a shaker at 4°C.
The gelling solution needs to be prepared just before being applied, and all the solutions have to be kept on ice. During the incubation, remove the cover tape from the spacers.

Gelling II: Transfer the sample to the prebuilt gelling chamber by placing a few drops of gelling solution in the middle of the coverslip with the spacers. Make sure the sample rests on the bottom, and add gelling solution around the sample.

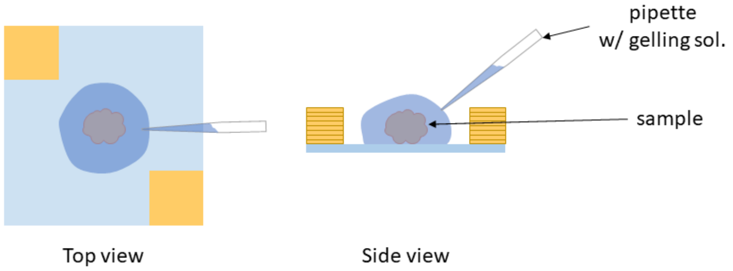

To avoid polymerization of the sample inside the well, place the well-plate with the samples on ice during the process. In addition, we recommend avoiding the simultaneous preparation of many samples. If the transfer to the gelling chamber is slow, there is a risk that the gel polymerizes in the well-plate.

Cover the sample with an 18 x 18 mm coverslip while avoiding the formation of bubbles around the sample or close to it. It should be enough gelling solution around the sample to be removed later and still have the sample surrounded by the gel.

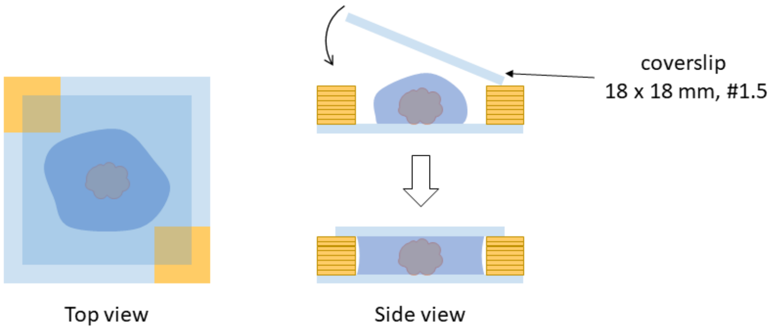

Put the gelling chamber on a small weighing boat (VWR 611-0093), and place it into a wet chamber to avoid dehydration of the gel.
To improve penetration of the gelling solution on big samples before polymerization, it is advisable to keep the samples at 4°C before incubation at 37°C.

Incubate in gelling solution for 2h at 37°C. Make sure that samples are not drying out.

14. **Remove excess gel:** Open the gelling chamber and remove the upper coverslip and the spacers. To remove the upper coverslip from the spacer, use a wet brush with PBST (0.1% or 0.3%) and apply on the spacers (see sketch below). After a couple of seconds, remove the coverslip and spacers with forceps. Remove the excess of the gel around the tissue with a scalpel or razor blade.
    Do not remove the sample from the bottom coverslip! This might damage the gel and sample.

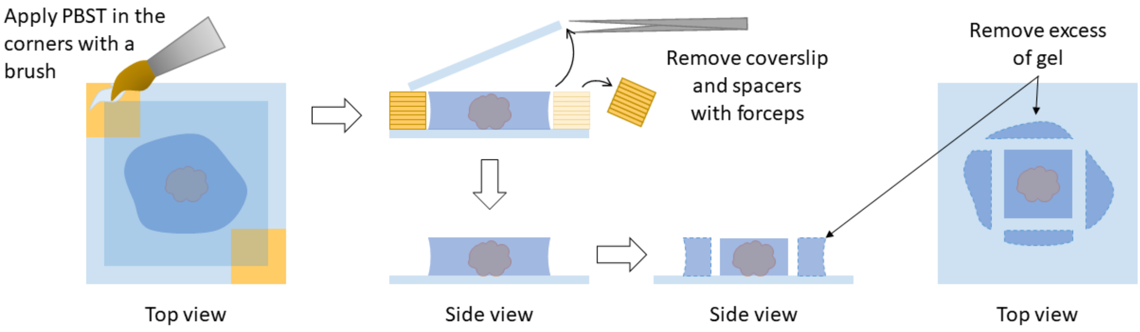

15. **Digestion:** Fill small plastic bowls, e.g. little weighing boats, with digestion buffer and incubate at 37°C. Use enough digestion buffer in order to cover the sample completely (~2,5mL for each weighing boat). Place in a wet chamber and close the box with paraffin. For thicker samples, the coverslip with the sample could be placed into a 6 well-plate.

    Keep the sample in digestion buffer until it is completely transparent. This takes about 24h for a 1 mo organoid. Change the digestion buffer every 24h if necessary.

16. **Expansion process**: Carefully remove the digestion buffer with a pipette. Use the bottom coverslip to transfer the sample into a 6 well-plate, and depending the desired expansion factor, wash the samples as follows:
    - **1,5x:** wash them with 1xPBS around 3-4 times.
    - **4x:** wash them with distilled water (MilliQ with 5mM Hepes, pH 7.4) around 3-4 times.

    For nuclear staining, all samples could be stained using Hoechst 33342 (H3570, Invitrogen) at a concentration of 5µg/mL.

Sample age	1 mo	2 mo - 5 mo	>8 mo
Incubation time	ON	2 days	3 days

After expansion, transfer the sample to the imaging chamber for microscopy.

Required solutions

Linking

1M MA-NHS in dimethyl sulfoxide. Stored as 10 µL aliquots in -20°C.

Monomer Solution

In order to yield 9.4 mL monomer solution use:

Chemical	**Stock Concentration**	**Volume [mL]**
Sodium acrylate	19 g/50 mL	2.25
Acrylamide 40%		0.625
N,N'-Methylenebisacrylamide	1 g/50 mL	0.75
Sodium Chloride	14.6 g/50 mL	4
PBS	10x	1
MilliQ Water		0.775

Stored as 600 µL aliquots in -20°C

Digestion Buffer

In order to yield 100 mL digestion buffer use:

Chemical	**Amount**
Tris	0.6057 g
EDTA	0.0372 g
Triton X-100 (100%)	500 µL
Guanidinium chloride	7.6424 g

Fill up to 96 mL with MilliQ Water.

Adjust the buffer to pH 8.0.

Stored as 4.8 mL aliquots in -20°C without Prot-K.

Just before use add 100 µL ddH$_2$O and 100 µL Prot-K. Final concentration of Prot-K, 16 $^{\text{units}}/_{\text{mL}}$